

MULTISENSOR TRANSLATION AND CONTINUITY OF VEGETATION INDICES
USING HYPERSPECTRAL DATA

By

Youngwook Kim

A Dissertation Submitted to the Faculty of the
DEPARTMENT OF SOIL, WATER, AND ENVIRONMENTAL SCIENCE

In Partial Fulfillment of the Requirements

For the Degree of

DOCTOR OF PHILOSOPHY

In the Graduate College

THE UNIVERSITY OF ARIZONA

2007

THE UNIVERSITY OF ARIZONA
GRADUATE COLLEGE

As members of the Dissertation Committee, we certify that we have read the dissertation prepared by Youngwook Kim

entitled MULTISENSOR TRANSLATION AND CONTINUITY OF VEGETATION INDICES USING HYPERSPECTRAL DATA

and recommend that it be accepted as fulfilling the dissertation requirement for the Degree of Doctor of Philosophy

Date: November 5th 2007
Dr. Alfredo Huete

Date: November 5th 2007
Dr. Edward Glenn

Date: November 5th 2007
Dr. Kurtis J. Thome

Date: November 5th 2007
Dr. Willem J. D. van Leeuwen

Final approval and acceptance of this dissertation is contingent upon the candidate's submission of the final copies of the dissertation to the Graduate College.

I hereby certify that I have read this dissertation prepared under my direction and recommend that it be accepted as fulfilling the dissertation requirement.

Date: November 5th 2007
Dissertation Director: Dr. Alfredo Huete

STATEMENT BY AUTHOR

This dissertation has been submitted in partial fulfillment of requirements for an advanced degree at The University of Arizona and is deposited in the University Library to be made available to borrowers under the rules of the library.

Brief quotations from this dissertation are allowable without special permission, provided that accurate acknowledgement of source is made. Requests for permission for extended quotation from or reproduction of this manuscript in whole or in part may be granted by the head of the major department or Dean of the Graduate College when in his or her judgment the proposed use of the material is in the interests of scholarship. In all other instances, however, permission must be obtained from the author.

SIGNED: Youngwook Kim

ACKNOWLEDGEMENTS

I would like to thank the dissertation director Dr. Alfredo Huete for his advising, assistance, guidance, and kindness. Special thanks go to Dr. Edward Glenn, Dr. Kurtis Thome, and Dr. Willem J. D. van Leeuwen for helping, educating, and giving me the confidence. My sincere gratitude goes to current and former TBRS members, especially Dr. Tomoaki Miura and Dr. Kamel Didan for teaching a lot of image processing techniques and skills on hyperspectral and multispectral imagery.

I wish to thank my wife (Namhee), two daughters (Ashley and Jenna), my parents, my parents-in-law, my grandparents, my sister, my sister-in-laws, my brother-in-laws, my nephew, my niece, and my friends in Korea for their patience, trust, love, and encouragement.

I sincerely thanks to the SWES administrative team under the leadership of Dr. Jeffrey Silvertooth, Judith Ellwanger, Veronica Hirsch, and Alicia Velasquez for their kindness to support me during my study.

This work was supported by a NPP VIIRS NASA grant #NNG04GJ22G for assessment of Vegetation Index EDR's. (J. Privette, P.I.), and NASA MODIS contract #NNG04HZ20C.

TABLE OF CONTENTS

LIST OF ILLUSTRATIONS	6
LIST OF TABLES	8
ABSTRACT	9
I. INTRODUCTION	11
Introduction and problem statement	11
Objectives	13
Overview of dissertation	13
II. EVALUATION OF INTER SENSOR TRANSLATIONS WITH HYPERSPECTRAL SIMULATION OF MULTIPLE SENSORS	15
1. Introduction	15
2. Study site and Methodology	18
3. Results	27
4. Discussion and conclusions	70
III. COMPATIBILITY OF ENHANCED VEGETATION INDEX ACROSS SENSORS: AN EVALUATION WITH CONVOLVED HYPERION DATA	73
1. Introduction	73
2. Study site and Methodology	77
3. Results	80
4. Discussion and conclusions	106
IV. MUTISENSOR REFLECTANCE AND VEGETATION INDEX COMPARISONS OF AMAZON TROPICAL FOREST PHENOLOGY WITH HYPERSPECTRAL HYPERION DATA	109
1. Introduction	109
2. Methodology	112
3. Results	113
4. Conclusions	138
REFERENCES.....	140

LIST OF ILLUSTRATIONS

<i>FIGURE 1-1:</i> Comparison of spectral responses over AVHRR, MODIS, VIIRS, SPOT-VGT, and SeaWiFS sensors in Visible/NIR	22
<i>FIGURE 1-2:</i> Image processing for spectral convolution of Hyperspectral data to multiple sensors	23
<i>FIGURE 1-3:</i> Inter sensor translations for ASD-MQUALs data in ANP and BNP, Brazil, Jul, 2002	28
<i>FIGURE 1-4:</i> Sensor deviation from MODIS value concerning ASD-MQUALs data in ANP and BNP, Brazil	32
<i>FIGURE 1-5:</i> Inter sensor translations for Hyperion at TOC level in ANP, BNP, and Tapajos, Brazil, Jul, 2002	36
<i>FIGURE 1-6:</i> Sensor deviation from MODIS value concerning Hyperion in ANP, BNP, and Tapajos, Brazil	40
<i>FIGURE 1-7:</i> Inter sensor translations for AVIRIS at TOC level in Flagstaff, AZ, Jul, 2003	45
<i>FIGURE 1-8:</i> Sensor deviation from MODIS value concerning AVIRIS in Flagstaff, AZ	46
<i>FIGURE 1-9:</i> Inter sensor relationships for reflectances and VIs from the combined hyperspectral data	54
<i>FIGURE 1-10:</i> Inter sensor translations for the combined hyperspectral data	60
<i>FIGURE 1-11:</i> The difference between trans/calc and convolved VIs	62
<i>FIGURE 1-12:</i> The difference between the transformed VIs and the computed VIs versus MODIS VIs	63
<i>FIGURE 1-13:</i> Deviation from MODIS value using the combined sensor analyses	67
<i>FIGURE 2-1:</i> Sensor deviation from MODIS reflectance (TOC) using Hyperion sensor analyses	85
<i>FIGURE 2-2:</i> VIs deviation from MODIS (TOC) for 5 sensors	89
<i>FIGURE 2-3:</i> EVI&EVI2 deviation vs. blue, red, and NIR reflectance deviation from MODIS (TOC) per each sensor	93
<i>FIGURE 2-4:</i> Spectral coherency on blue and red reflectance using EO-1 Hyperion	96
<i>FIGURE 2-5:</i> Crossplot of EVI and MODIS EVI (TOC) over sensors	97
<i>FIGURE 2-6:</i> Crossplot of EVI2 and MODIS EVI (TOC) over sensors	98
<i>FIGURE 2-7:</i> Crossplot of EVI2 and MODIS EVI2 (TOC) over sensors	98
<i>FIGURE 2-8:</i> The comparison of the ratio of red to blue regarding MODIS values over different land covers for multiple sensors ((a) Primary Forest, (b) Cerrado (Savanna) Grassland, (c) Cerrado (Savanna) Woodland, (d) Cultivated Pasture, (e) Sel Logged Forest, and (f) Converted Pasture)	101
<i>FIGURE 2-9:</i> MAD values over different land covers for multiple sensors (a, b) VIIRS-MODIS, (c, d) SPOT-VGT-MODIS, (e, f) SeaWiFS-MODIS	103

LIST OF ILLUSTRATIONS - *Continued*

<i>FIGURE 3-1:</i> Location of 6 EO-1 Hyperion scene acquisitions within Tapajos National Forest and surrounding areas, south Santarem, Para, Brazil; each Hyperion is 11 km wide	114
<i>FIGURE 3-2:</i> VIs variations for 5 phenological stages ((a) Agricultural site, (b) Primary Forest, and (c) Secondary Forest)	116
<i>FIGURE 3-3:</i> Crossplot of sensor and MODIS blue reflectance with all three land covers ((a) VIIRS, (b) SPOT-VGT, and (c) SeaWiFS)	120
<i>FIGURE 3-4:</i> Crossplot of sensor and MODIS red reflectance with all three land covers ((a) VIIRS, (b) SPOT-VGT, and (c) SeaWiFS)	121
<i>FIGURE 3-5:</i> Crossplot of sensor and MODIS NIR reflectance with all three land covers ((a) VIIRS, (b) SPOT-VGT, and (c) SeaWiFS)	122
<i>FIGURE 3-6:</i> VIIRS VI's deviations from MODIS values ((a) Agricultural site, (b) Primary Forest, and (c) Secondary Forest).....	125
<i>FIGURE 3-7:</i> AVHRR VI's deviations from MODIS values ((a) Agricultural site, (b) Primary Forest, and (c) Secondary Forest).....	126
<i>FIGURE 3-8:</i> SPOT-VGT VI's deviations from MODIS values ((a) Agricultural site, (b) Primary Forest, and (c) Secondary Forest).....	127
<i>FIGURE 3-9:</i> SeaWiFS VI's deviations from MODIS values ((a) Agricultural site, (b) Primary Forest, and (c) Secondary Forest).....	128
<i>FIGURE 3-10:</i> Slope variations of cross sensor translation equations of reflectance and VIs between sensor and MODIS regarding three periods (early-, mid-, and late- dry seasons) and land covers ((a) VIIRS, (b) AVHRR, (c) SPOT-VGT, and (d) SeaWiFS)	133
<i>FIGURE 3-11:</i> MAD variations of VIs between sensor and MODIS regarding three periods (early-, mid-, and late- dry seasons) and land covers ((a) VIIRS, (b) AVHRR, (c) SPOT-VGT, and (d) SeaWiFS)	135

LIST OF TABLES

<i>TABLE 1-1:</i> Description of the study areas	21
<i>TABLE 1-2:</i> Full width of the spectral bands at half of the maximum spectral transmissivity for the VNIR and SWIR bands of the AVHRR, MODIS, SPOT-VGT, and VIIRS sensors	21
<i>TABLE 1-3:</i> Description of parameters used in the Hyperion atmospheric corrections	25
<i>TABLE 1-4:</i> Comparison of linear regression equation regarding MODIS	50
<i>TABLE 1-5:</i> Comparison of linear regression equation within one dataset	52
<i>TABLE 1-6:</i> Slope, Intercept, and R-square in three levels reflectance at the TOC level	57
<i>TABLE 1-7:</i> Inter sensor translation equations for reflectances and VIs with the combined sensors	58
 <i>TABLE 2-1:</i> Description of the study areas	 78
<i>TABLE 2-2:</i> Cross sensor translation equations with MODIS using linear regression lines	81
 <i>TABLE 3-1:</i> Inter sensor translation equations with MODIS using linear regression lines across early-, mid-, and late-dry season at the combined three land covers	 130
<i>TABLE 3-2:</i> Comparison of linear regression equation regarding MODIS at the combined three land covers	137

ABSTRACT

The earth surface is monitored periodically by numerous satellite sensors which have different spectral response functions, image acquisition heights, atmosphere correction schemes, overpass times, and sun/view angle geometries. Temporal and spatial variations of land surface properties, such as vegetation index, Leaf Area Index (LAI), land surface temperature, and soil moisture, have been provided by long-term time series of various remote sensing datasets. Inter-sensor translation equations are required to build long-term time series by the combination of multiple sensors from historical to advanced and new satellite datasets. In the first chapter, inter-sensor translation equations of band reflectances and two vegetation indices (e.g. Normalized Difference Vegetation Index (NDVI) and Enhanced Vegetation Index (EVI)) were derived using linear regression equations relative to Moderate Resolution Imaging Spectroradiometer (MODIS) values. The consistency and validation of inter-sensor transforms were investigated through statistical student's t-test and the root mean square error (RMSE).

In the second chapter, cross-sensor extension of EVI and a 2-band EVI (without the blue band; EVI2) were investigated based on the continuity of both EVI's. Sensor specific red-blue coherencies were examined for the possibility of the EVI and EVI2 extension from MODIS sensor. The EVI continuity to MODIS was particularly problematic for the Visible Infrared Imager / Radiometer Suite (VIIRS) and the Sea-viewing Wide Field-of-view Sensor (SeaWiFS) that have dissimilar blue bands from that of MODIS. The cross-sensor extension and compatibility of EVI2 were improved and

provided the possibility to be lengthened to the Advanced Very High Resolution Radiometer (AVHRR) using its translation equation.

Finally, we evaluated the use of sensor-specific EVI and NDVI data sets, using a time sequence of Hyperion images over Amazon rainforest in Tapajos National Forest, Brazil for the 2001 and 2002 dry seasons. We computed NDVI, EVI, and EVI2 with the convolution data of different global monitoring and high temporal resolution sensor systems (AVHRR, MODIS, VIIRS, SPOT-VGT, and SeaWiFS) from Hyperion, and evaluated their spectral deviations and continuity in the characterization of tropical forest phenology. Our analyses show that EVI2 maintains the desirable properties of increased sensitivity in high biomass forests across all sensor systems evaluated.

I. INTRODUCTION

Introduction and problem statement

Numerous satellite sensor systems are used to observe the Earth's surface to assess land cover change and agricultural production, to manage natural resources, and to monitor vegetation – climate interactions. These sensor platforms have different optical characteristics, such as spectral response functions, image acquisition heights, atmospheric status, atmosphere correction schemes, overpass times and sun/view angle geometries. A long-term time series of satellite measurements have provided many important environmental variables, which are related to temporal and spatial variations of land surface properties. This information can provide an important step in examining the causes of global changes on climate and ecosystem. These long-term observations require much effort to ensure continuity and compatibility due to drifts in calibration, filter degradation, and variations in band locations and/or bandwidths. In order to build a long-term time series by the combination of multiple sensors, inter-sensor relationships should be specified and evaluated under several conditions. Spectral convolution of multiple sensors (e.g. National Oceanic and Atmospheric Administration (NOAA) 14 AVHRR, MODIS, the VEGETATION instrument of the System Pour l'Observation de la Terre (SPOT-VGT), and National Polar-Orbiting Operational Environmental Satellite System (NPOESS) VIIRS) from different hyperspectral sensor platforms (a full-range Analytical Spectral Devices sensor-Modland Quick Airborne Looks (ASD-MQUALs), Airborne Visible Infra Red Imaging Spectrometer (AVIRIS), and spaceborne Hyperion), all at nearly nadir view angle, were simulated at different platform levels of image acquisition

height and land cover types. A couple of inter-sensor translations will be obtained from each sensor pairs stated above (sensor versus MODIS). Inter-sensor relationships of band reflectances and two vegetation indices (e.g. NDVI and EVI) should be evaluated carefully through the deviation from MODIS values. The consistency of inter-sensor translation equations derived from three hyperspectral platforms have to be proved through statistical student's t-test for each platform pairs.

There are many studies that show the compatibility of merging coarse resolution NDVI values from new and advanced sensor systems for the purpose of the extending the existing long-term NDVI time series data. In contrast, the continuity and compatibility of the EVI across different sensor systems has received much less attention, compared with the NDVI, for continuity studies, despite the potential complementary benefits of the EVI to the existing NDVI time series, such as in more densely vegetated forest canopies.

In addition to NDVI, we should intensively evaluate the cross sensor extension of EVI, a 2-band EVI, without the blue band, and NDVI as a comparison purpose, using a set of convolved Hyperion satellite images over grassland, savanna, wetland, and forest land cover types in Brazil.

Now, we have inter-sensor translation equations from various datasets, but an analysis of inter-sensor translations with respect to phenological stages has not been made. The deviation analyses of vegetation indices derived from this study would be useful to understand tropical forest phenology, to generate consistent and objective estimates of phenology, and to evaluate phenological influences on inter-sensor transforms. NDVI, EVI, and a 2-band version of EVI (EVI2) computed from different

global monitoring systems need to be analyzed for their spectral differences and continuity in the characterization of tropical forest phenology.

Objectives

The major objective of this research is to investigate how to build a long-term time series from multiple instruments consistently with inter-sensor translations of spectral bands (blue, red, and NIR bands), EVI and EVI2, coherency analyses for multiple sensors, and sensitivity analysis on inter-sensor transforms.

We investigate the effect of land cover type on EVI, EVI2 translation, red-blue coherency, and the variation of inter-sensor translation equations of blue, red, NIR reflectances and VI's (NDVI, EVI, and EVI2) between the sensors and MODIS during periods of maximum phenologic activity.

Finally, we evaluate cross-sensor compatibilities of MODIS and VIIRS EVI and EVI2, as well as MODIS and AVHRR EVI2 and the interactions and influences of phenology (stage of greenness) on inter-sensor translation and continuity relationships.

Overview of dissertation

The major goal of this dissertation is to derive inter-sensor translation equations using the convolved multi-spectral sensor bandpass data from three hyperspectral platforms and the continuity of vegetation indices on multiple image acquisition heights, land cover type, and phenology.

This dissertation consists of three chapters. Generally, the first chapter deals with inter-sensor translation equations of multi-spectral reflectances and vegetation indices (NDVI and EVI) over three hyperspectral platform levels: canopy, airborne, and spaceborne platform levels. Spectral deviations from MODIS values are analyzed across multiple sensors (VIIRS, AVHRR, and SPOT-VGT) in Flagstaff, Arizona and Brazil, in order to see the differences per each platform level, sensor type and land cover. Finally, inter-sensor transforms are derived using the combined hyperspectral sensor.

The second chapter focuses on the continuity of the enhanced vegetation index (EVI) across multiple sensors (MODIS, AVHRR, VIIRS, SPOT-VGT, and SeaWiFS) from Hyperion data in Brazil. In particular, the new EVI (without blue band; EVI2) is introduced. Coherency analyses are performed between both red and blue reflectances. The sensitivity of EVI and EVI2 on reflectance translation and the effect of land cover type on EVI and EVI2 translation are examined. Lastly, cross-sensor compatibilities of MODIS and VIIRS EVI and EVI2 as well as MODIS and AVHRR EVI2 are evaluated.

The final chapter concentrates on the phenological influences on multi-spectral reflectance and vegetation indices using Hyperion data in the Amazon rainforest areas (Tapajos National Forest). The variation of inter-sensor translation equations of reflectances and vegetation indices is analyzed during the dry seasons in the Tapajos area. The influences of stage of greenness (phenology) on inter-sensor transform and continuity are evaluated.

II. EVALUATION OF INTER-SENSOR TRANSLATIONS WITH HYPERSPETRAL SIMULATION OF MULTIPLE SENSORS

1. Introduction

Long-term monitoring of the Earth's environment by satellite sensors requires consistent and comparable measurements. Starting with the Advanced Very High Resolution Radiometer (AVHRR) onboard the National Oceanic and Atmospheric Administration's (NOAA) polar orbiting satellite in 1981, multiple sensors have provided a long-term time series of satellite data, which contains rich information pertaining to the state and changes of many important biophysical variables, in particular the spectral vegetation index. Spectral vegetation indices (Tucker et al. 1979 and Huete et al. 1997) are one of the most important satellite products in monitoring temporal and spatial variations of vegetation photosynthetic activities and biophysical properties, including its relationship to biomass, leaf area index, agriculture and rangeland, primary productivity, photosynthetic radiation, carbon dioxide, meteorological and ecological parameters. However, use of such diverse satellite datasets requires a careful evaluation of their compatibility and consistency to avoid any artifacts due to differences in spectral response function, various atmospheric status, sensor/view angle geometry, different spatial resolution and overpass time. To build long-term observations from these satellite datasets, much efforts are required to ensure continuity and compatibility due to drifts in calibration, filter degradation, and variations in band locations and/or bandwidths (Miura et al. 2006 and Bryant et al. 2003). Also, the NDVI saturation of most of the densely forest areas is still problematic in sensor continuity analyses and inter-sensor translations.

Most sensor to sensor continuity studies have focused on the calibration and validation (the accuracy of data products) of each sensor through ground truth data such as field measurements and airborne sensor data. MODIS sensor calibration and validation were especially big issues before the Earth Observing System (EOS) Terra platform was launched. Most studies tried to calibrate and validate the new moderate resolution sensors with airborne sensors and/or the finer resolution sensors (Gao et al. 2003 and Huete et al. 2002). Sensor calibration uncertainties on MODIS vegetation indices by atmospheric radiative transfer code were evaluated (Miura et al. 2000). Price (1987) pointed out the major importance of solar input and radiometric calibration when comparing indices from different sensors.

Prelaunch MODIS VI prototype studies were compared with AVHRR data to evaluate the MODIS vegetation index compositing algorithm and ascertain the possibility of the continuity from AVHRR sensor. The BRDF composite approach may be more representative of vegetation changes over a 16-day period (van Leeuwen et al. 1999).

Trishchenko et al. (2002) studied the continuity on the AVHRR sensor series. Many AVHRR sensors have been launched over a 20+ year period and their sensors have been gradually improved. Although they were manufactured in the same way, their spectral characteristics were slightly different due to spectral response function (SRF) and overpass times. For multi-sensor comparisons, the effects of SRF were described by analyses of two pairs of actual satellite imagery data for AVHRR from NOAA-14 and -15 and from MODIS (Trishchenko et al. 2002). MODIS and AVHRR 16-day normalized difference vegetation index composite data at nearly the same overpass time were

compared, therefore, comparisons of Terra-MODIS and NOAA-17 AVHRR NDVI data (both AM platforms) and Aqua-MODIS and NOAA-16 AVHRR NDVI data (both PM platforms) are recommended (Gallo et al. 2005 and 2004). The new Global Inventory Monitoring and Modeling Study (GIMMS) product was provided from the AVHRR series using enhanced calibration and correction that considered the sensor differences, and included solar zenith angle correction (Tucker et al. 2005). A series of Landsat-4, 5, 7, and EO-1 ALI were investigated on the data continuity through ground-data verification and coincident image analysis (Bryant et al. 2003). Recently, cross-sensor relationships of reflectance and NDVI without the sun/view angle biases were studied using spectral convolution of hyperspectral sensors to multi-sensors (Miura et al. 2006). As a cross-calibration technique, an approach to calibrate reflectance bands of NOAA16 AVHRR over a desert area with a short-term time series of MODIS and a BRDF model were provided (Vermote et al. 2006).

Many cross-sensor translation equations were developed and compared from these theoretical bases (van Leeuwen et al. 2006, Miura et al. 2006, Steven et al. 2003, and Gitelson et al. 1998). Those translation equations are still dependent on the type of land cover, sensor spectral characteristics, and atmospheric condition.

Sensor continuity tests were conducted from inter-comparison of various multi-sensor datasets with the relationship between NDVI and biophysical variables (Goetz 1997). Compositing NDVI images were fairly robust and the NDVI anomalies exhibited similar variances between sensors on the historic AVHRR NDVI record for vegetation phenological studies (Brown et al. 2006).

The primary objective of this research is to investigate how to build a consistent long-term time series from multiple instruments. This study on sensor continuity work is to simulate and evaluate vegetation indices through spatial and spectral convolutions of hyperspectral data to other multi-spectral sensors (e.g. MODIS, AVHRR, SPOT_VGT, ETM+, and VIIRS; Huete et al. 2004). Lastly, the comparison and evaluation between each translation equation were performed to determine the changes of inter-sensor translation equation over diverse conditions. The essential elements and effects of inter sensor translation were investigated closely and determined.

For global applications focusing on vegetation responses to climate change, continuity and consistency of VI observations are essential in order to detect subtle trends in the long-term time series data. This data can enhance ground-based monitoring efforts, identify anomalous trends, and compare current climate conditions with analogous conditions from past years for insights into potential future vegetation dynamics (van Leeuwen et al. 2006). Although the differences are relatively small when vegetation indices are calculated from surface reflectance data, the inconsistencies in the data may be problematic when different monitoring systems were used in combination, or when one system takes over from another in a long-term time series (Steven et al. 2003).

2. Study Site and Methodology

The hyperspectral imager, Hyperion, is part of the Earth Orbiter 1 (EO-1), launched in November 2000 as part of NASA's New Millennium program that focused on new, more cost effective technologies for the Earth observation. The Hyperion hyperspectral

imager is a pushbroom sensor providing 220, 10 nm bands covering the spectrum from 400 to 2500 nm. Hyperion data was acquired for a wide variety of biomes in Brazil, including the Tapajos broadleaf evergreen rainforest (Tp, July 30, 2001); the cerrado/savannah biome in Brasilia National Park (BNP, July 20, 2001); and the Araguaia National Park (ANP, July 18, 2001), transition biome with rainforest, wetlands, and cerrado vegetation. All three sites are primary core validation sites for the Large Scale Biosphere and Atmosphere in the Amazon Experiment (LBA) experiment. For temporal analyses, four more Hyperion images in Tapajos area were processed. In addition, light-aircraft (ultra light; MQUALs) measurements with the ASD spectroradiometer were collected at the ANP (S 10°5', W 50°3') in Brazil, July 25, 2001 and BNP (S 15°4', W 47°59') in Brazil, July 21, 2001. The ASD_MQUALs acquired data every 1 nm at effective nominal bandwidths of 10nm from 380nm to 2500 nm with 15 degree Field of View (FOV) (http://eospsso.gsfc.nasa.gov/eos_observ/1_2_99/p22.html). The ultra light flew "below the atmosphere" at 150 m above ground level (AGL) at a speed of 30 m per second collecting a single spectrum every ~1 second over a ground spatial resolution of 13m by 30m. The data was acquired between 13:00 – 13:30 UTC (ANP; 44.8° Solar Zenith Angle (SZA) and 2.1° View Zenith Angle (VZA)), between 13:00 – 13:30 UTC (BNP; 49.2° SZA and 0.7° VZA), and between 13:30 – 14:00 UTC (Tapajos; 38.1° SZA and 4.6° VZA) and calibrated to ground reflectances by taking a ratio of the readings made over a Spectralon white reference panel before and after the flight. This data was convolved to the various sensor bandpasses at the top of canopy without atmospheric correction (Huete et al. 2006).

An airborne hyperspectral AVIRIS data was used in this analysis. A unique optical sensor delivers calibrated images of spectral radiance in 224 contiguous spectral channels (also called bands) with wavelengths from 400 to 2500 nanometers (nm). This low altitude AVIRIS imagery was obtained by a National Aeronautics and Space Administration (NASA) Twin Otter aircraft flying at an altitude of 1.7km above ground level with 33 degree FOV (Vane et al., 1993). At this altitude, AVIRIS pixels have a spatial resolution of about 4m and its swath was around 1.9km. AVIRIS had been flown over C. Hart Merriam Transect, Flagstaff, AZ on July 2003, and October 2003 when it collected 11 transect lines for July 2003 and 3 transect lines for October 2003 (Kim et al. 2005). C. Hart Merriam's investigations into distinct Life Zones following the slope of the San Francisco Peaks in Northern Arizona has helped shape present research into six dominant vegetation types on a 3000 m elevational gradient from the top of Mt. Humphreys to the Great Basin Desert floor of the Colorado Plateau (Kim et al. 2004). Land cover types were provided in Table 1-1 and classified across three Hyperspectral platforms using field survey with GPS measurements.

Multispectral sensors derived from the convolution of hyperspectral datasets will be analyzed over three different platforms levels; canopy-, airborne-, and satellite-level. A wide set of Hyperion images (as well as AVIRIS and ASD_MQUALs) will be utilized to compare reflectance and vegetation indices at canopy scale to Hyperion to MODIS scales.

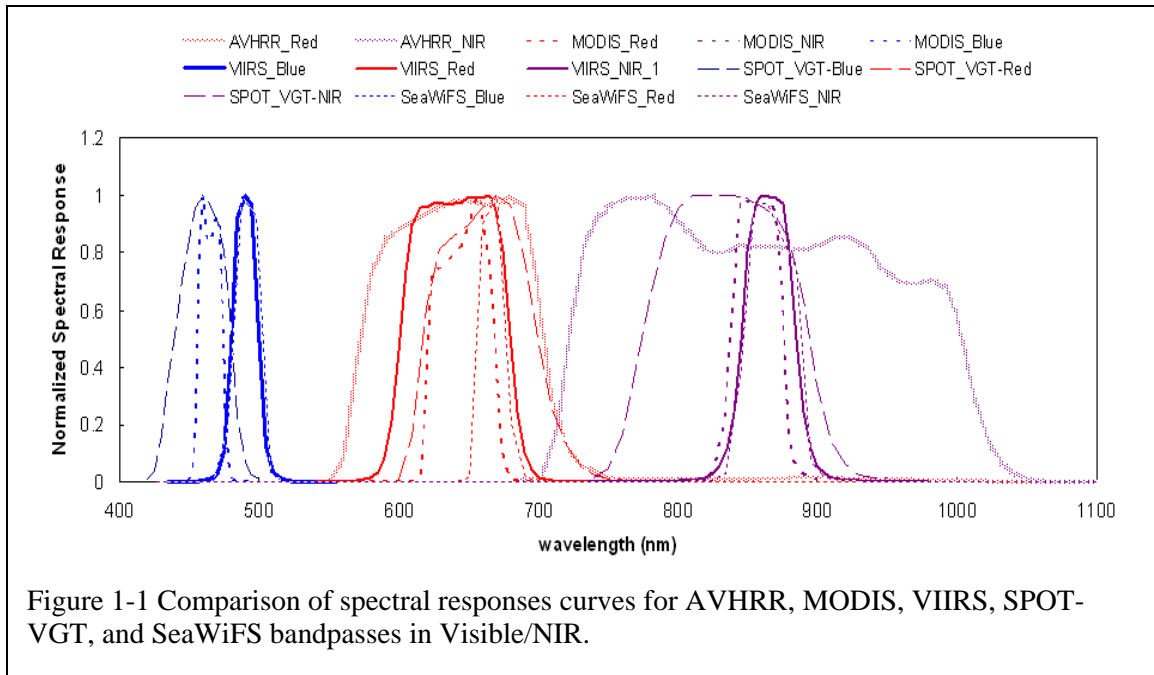
Fig. 1-1 and Table 1-2 display the sensor spectral response functions and image processing for spectral convolution and atmospheric correction by 6S (Vermote et al.

Table 1-1. Description of the study areas

Site location	Mean Annual Precip.	Mean Annual Temp.	Major Land cover type	Mean Elevation
Tapajos National Forest, Brazil	2060 mm	26 °C	Primary Forest Cultivated Pasture	100 m
Araguaia National Park, Brazil	1670 mm	26 °C	Riparian Forest Primary Forest Savanna Woodland Savanna Grassland Cultivated Pastures Burned Cerrado Sand Beach Water	210 m
Brasilia National Park, Brazil	1260 mm	21 °C	Riparian Forest Cerrado Woodland Cerrado Grassland	900 m
Great Basin Desert, Flagstaff, AZ	178 mm	11.1 °C	Desert shrubs Cacti	<1500 m
Desert Grassland, Flagstaff, AZ	229 mm	13.5 °C	Desert Grass Shrubs	1250 m
Pinyon-Juniper Woodlands, Flagstaff, AZ	381 mm	11.5 °C	Pinyon Pine Juniper	1750 m
Ponderosa Pine Forest, Flagstaff, AZ	660 mm	10.9 °C	Ponderosa Pine	2250 m
Mixed Conifer Forest, Flagstaff, AZ	787 mm	6.6 °C	Douglas-fir White fir Limber Pine Quaking Aspen	2750 m

Table 1-2. Full width of the spectral bands at half of the maximum spectral transmissivity for the VNIR and SWIR bands of the AVHRR, MODIS, SPOT-VGT, and VIIRS sensors

Sensor	FWHM bandwidth (nm)						
	Blue	Green	Red	NIR	SWIR1	SWIR2	SWIR3
AVHRR	N/A	N/A	580-680	725-1100	N/A	N/A	N/A
MODIS	459-479	545-565	620-670	841-876	1230-1250	1628-1652	2105-2155
SPOT_VGT	430-470	N/A	610-680	790-890	N/A	1580-1750	N/A
VIIRS	478-498	545-565	600-680	845.5-884.5	1230-1250	1580-1640	2225-2275



1997), respectively. Spectral response curve in AVHRR is the widest among sensors. MODIS and VIIRS spectral response function are very similar except for blue. The spectral response curve of SPOT-VGT is as good as that of MODIS, excluding Near Infrared (NIR) band. NIR in SPOT-VGT is wider than that in MODIS, including NIR in MODIS as well.

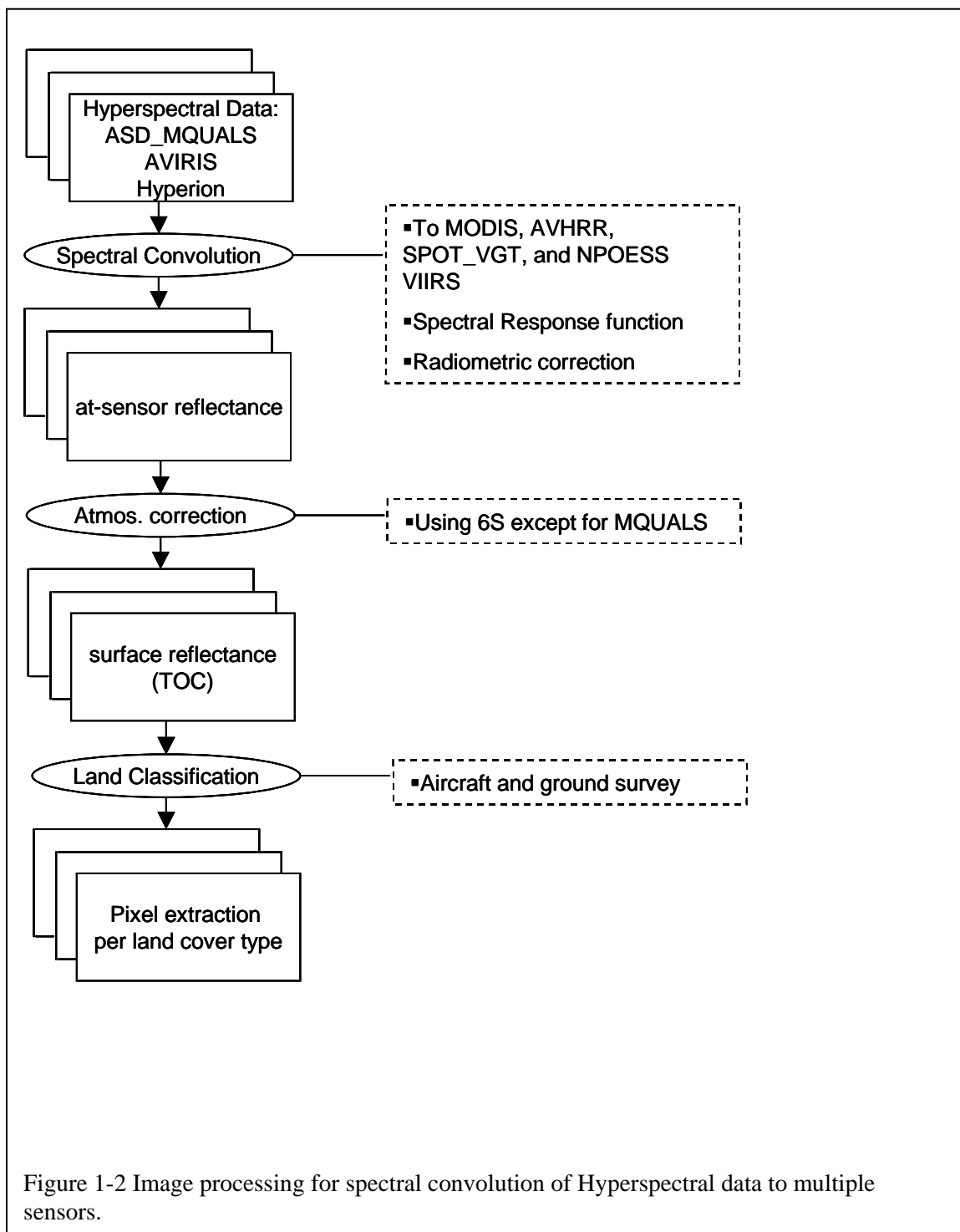
In Fig. 1-2, hyperspectral data is convolved spectrally to obtain multi spectral data at the top of atmosphere. All initial digital numbers (DN) in hyperspectral pixels are radiometrically calibrated to convert digital numbers to apparent band-averaged spectral radiance at the top of atmosphere (TOA) using radiometric calibration coefficients (gain and offset):

$$L_{i,j,k} = DN_{i,j,k} \times [CalCoef_k]^{-1} \quad [1]$$

where $i, j, k =$ image pixel i, j in spectral band k

$$L_{i,j,k} = \text{in-band radiance at sensor aperture } (\mu W / cm^2 nm sr)$$

$CalCoef_k = in - Band \text{ radiance calibration coefficient } (\mu W / cm^2 nm sr / DN)$
 $DN_{i,j,k} = image \text{ product digital value } (DN)$



This is atmospherically corrected to retrieve spectral reflectance at the top of canopy (TOC) by 6S based on MODTRAN 4 radiative transfer code. The 6S model was constrained with site specific atmospheric parameter values retrieved from available data sources (Table 1-3). The atmospheric model used for the scene was chosen based on the latitude and season. Pressure was adjusted for local ground elevation retrieved from GTOPO30 (Gesch, 1994). We used the continental aerosol model with a 100 km visibility (0.1 optical thickness; Miura et al. 2006). These assumptions were considered reasonable (Miura et al. 2006), because Hyperion images were acquired under a condition of clear skies at the beginning of the dry season (before the start of a biomass burning season) and AVIRIS has been flown under a clear sky before monsoon.

In the case of ASD_MQUALs, it is not applicable for atmospheric effects, since ASD_MQUALs data is not affected by the atmosphere due to the lowest acquisition height ("below the atmosphere"). Land cover types are classified by field survey and pixels are extracted according to the type of surface.

Two kinds of vegetation indices are used in this study. The EVI was developed to optimize the vegetation signal with improved sensitivity in high biomass regions and improved vegetation monitoring through a de-coupling of the canopy background signal and a reduction in atmosphere influences. Two equations take the form,

$$NDVI = \frac{\rho_{NIR} - \rho_{Red}}{\rho_{NIR} + \rho_{Red}} \quad [2]$$

$$EVI = G \times \frac{\rho_{NIR} - \rho_{Red}}{L + \rho_{NIR} + C_1 \times \rho_{Red} - C_2 \times \rho_{Blue}} \quad [3]$$

Table 1-3 Description of Parameters Used in the Hyperion Atmospheric Corrections.

	Hyperion			AVIRIS				
	ANP	BNP	Tapajos	Desert	Grassland	PJ	PP	MC
Image acquisition date	18-July- 2001	20-July- 2001	30-July- 2001	01-July- 2003	07-July- 2003	07-July- 2003	07-July- 2003	07-July- 2003
Ground elevation asl[*]	210	900 m	100 m	1.6 km	1.8 km	2 km	2.3 km	2.6 km
Solar zenith/azimuth angles	44° /134°	48° /137°	38° /125°	23° /117°	23° /117°	23° /117°	23° /117°	23° /117°
Atmospheric model	Tropical	Midlatitude winter	Tropical	Midlatitude summer				
water vapor content^{**}	4.3 cm	2.5 cm	4.3 cm	Lowtran				
Ozone content^{**}	.265 cm- atm.	.280 cm- atm.	.266 cm- atm.	Lowtran				
Aerosol model	Continental			Continental				
Visibility	100 km			100 km				

* ASL-Above Sea Level: Taken from GTOPO 30.

** Taken from Level-3 MODIS Atmospheric Daily Global Products.

Where ρ is atmospherically corrected surface reflectances, L is the canopy background adjustment that addresses nonlinear, differential NIR and red radiant transfer through a canopy, and $C1$, $C2$ are the coefficients of the aerosol resistance term, which used the blue band to correct for aerosol influences in the red bands. The coefficients adopted in the EVI algorithm are, $L=1$, $C1=6$, $C2 = 7.5$, and G (gain factor) = 2.5 (Huete, 1997).

3. Results

The ASD-MQUALs dataset has the least atmospheric contamination compared to the two other hyperspectral sensor platforms (AVIRIS and Hyperion), since the ultra light with ASD flew at 150 m AGL during the data acquisition time. In the analyses from ASD-MQUALs, it is assumed that atmospheric effects are minimal without atmospheric corrections. In addition, view angle effect does not need to be considered, because this dataset comes from identical hyperspectral simulations with near nadir view angle (view zenith angle (VZA): 0-5°). There are not the differences from view angle effects among the convolved multispectral sensors from Hyperion. Therefore, the biases from these simulations among the convolved multispectral sensors mainly result from the different spectral band responses over different land cover types, their temporal stage of growth (phenology), and, in the case of AVIRIS and Hyperion, the atmospheric correction schemes.

3.1. Spectral deviation analyses of ASD-MQUALs data across multiple sensors:

Canopy level

In this analysis, only three bands (Blue, Red, and NIR) were analyzed at the top-of-canopy level (TOC), i.e., the three bands used to compute vegetation indices. In Fig. 1-3, there was inter-sensor translation equations derived from ASD-MQUALs dataset. All cases were linear regressions with a strong R^2 values between sensor reflectances/VIs and MODIS reflectances/VIs.

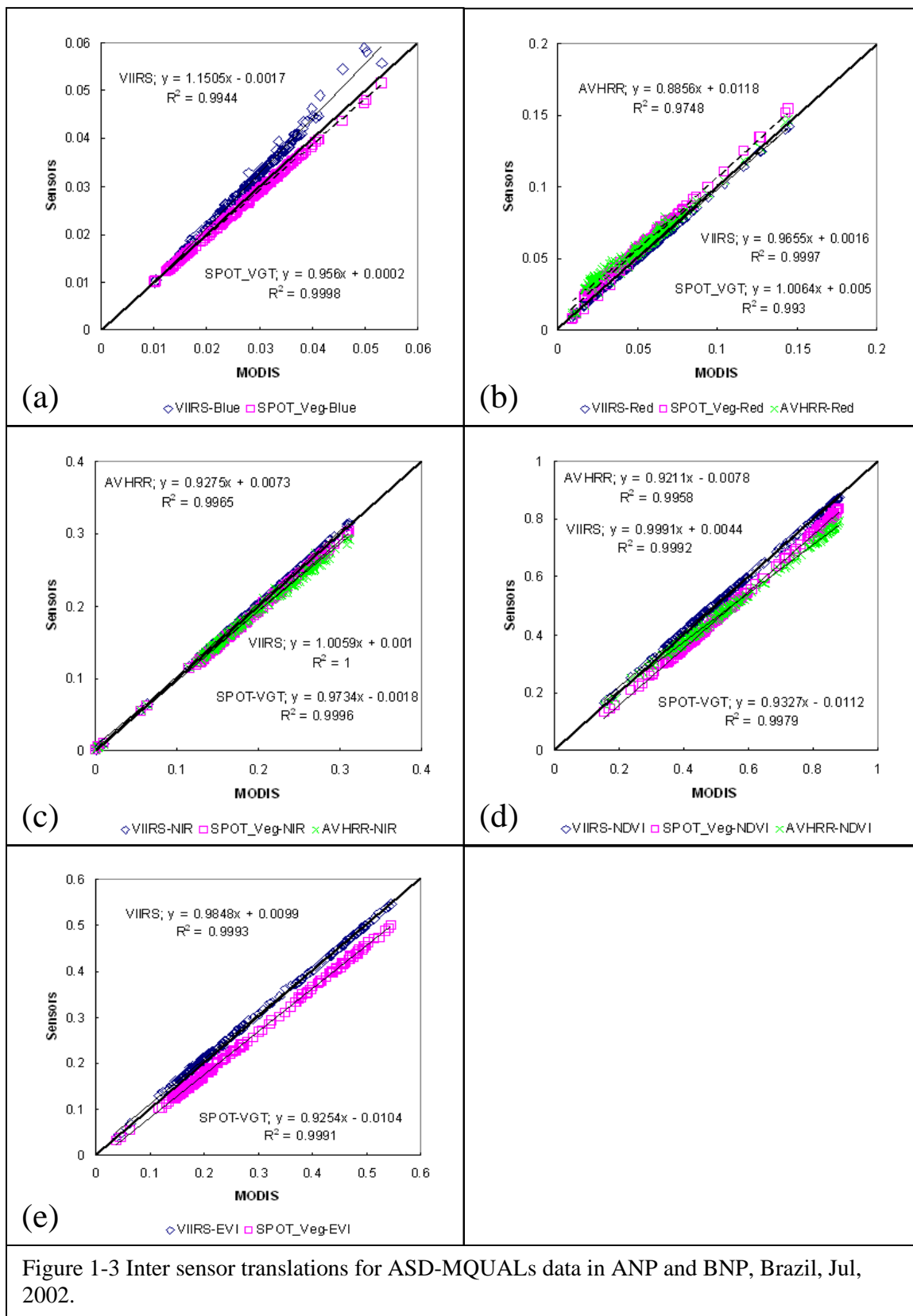


Figure 1-3 Inter sensor translations for ASD-MQUALs data in ANP and BNP, Brazil, Jul, 2002.

In order to see the detailed variations from MODIS values, sensor deviation from MODIS values were also computed as below:

$$\text{Sensor deviation} = \{\text{sensor reflectance (or VIs)} - \text{MODIS reflectance (or VIs)}\}$$

[4]

In Fig. 1-4a, the deviation of the VIIRS blue reflectance from the MODIS blue reflectance linearly increased in the positive direction with increasing MODIS blue reflectance, while the deviation of the SPOT-VGT blue reflectance also increased linearly, but in the negative direction. The biases between the VIIRS and MODIS blue reflectance were much larger up to ~ 0.01 than those between the SPOT-VGT and MODIS blue reflectance (up to -0.002) due to the different VIIRS blue band position from MODIS blue band. The spectral response function showed VIIRS blue band had shifted to the longer wavelength from MODIS blue band (Fig. 1-1). As expected, VIIRS red reflectance was very similar to MODIS red reflectance (a flat line), while SPOT-VGT and AVHRR red reflectance were a little different from the MODIS red reflectance (a curvilinear line) (Fig. 1-4b). In particular, it was the lower red reflectances (higher chlorophyll absorption) that resulted in the largest AVHRR deviation from MODIS red reflectances. The spectral band of the AVHRR red band was very wide and included portions of the green and NIR spectra, explaining huge differences between the AVHRR and MODIS red reflectance. In contrast to AVHRR and SPOT-VGT, the VIIRS red reflectance had negligible differences from the MODIS red reflectance.

For the NIR reflectance, the VIIRS NIR reflectance deviation was nearly constant, with an offset of $\sim +0.002$ reflectance units (Fig. 1-4c). The SPOT-VGT NIR reflectance

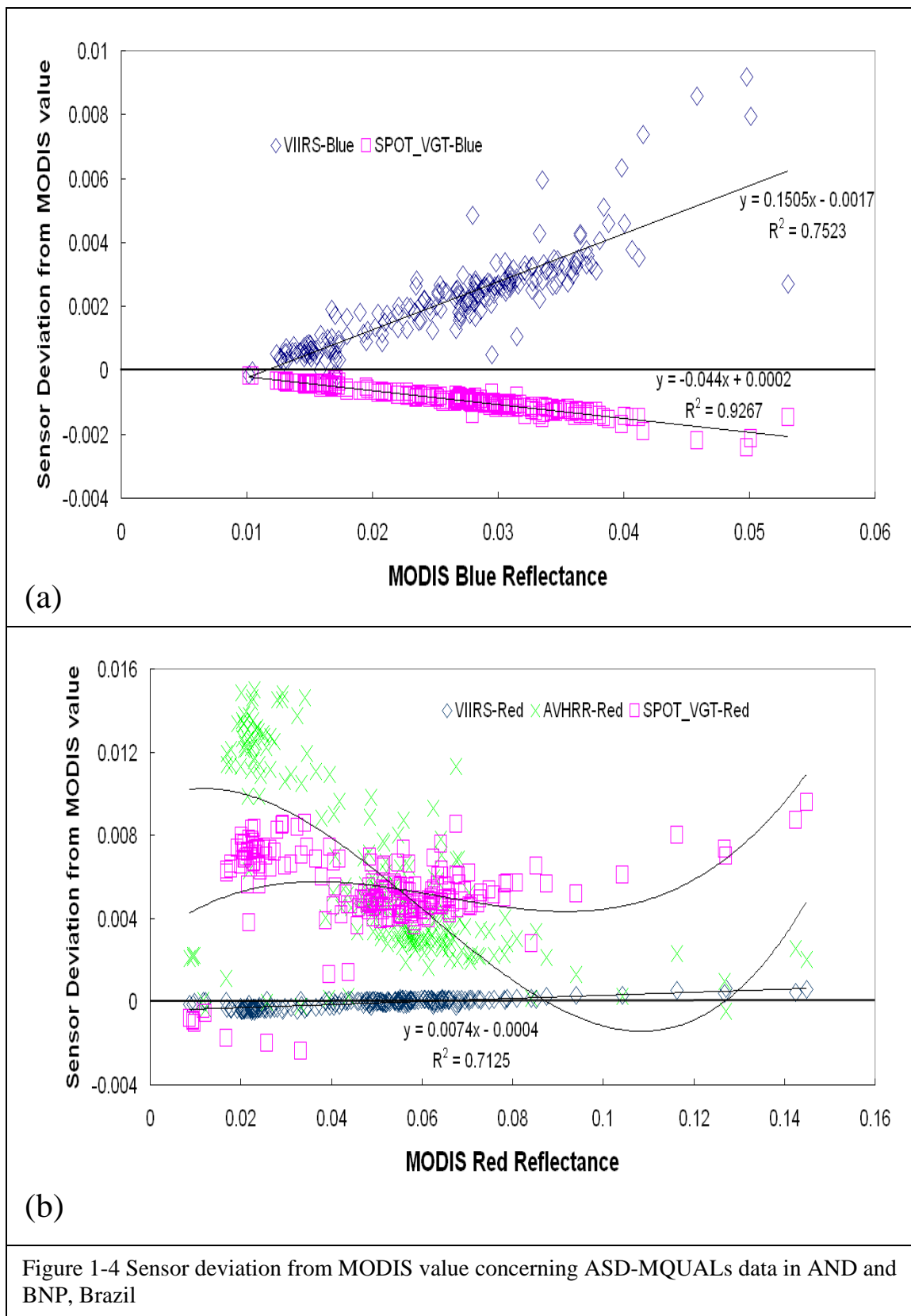
deviation was slightly curvilinear line up to around -0.008 , and became negative with increasing MODIS NIR reflectances (Fig. 1-4c). In contrast to VIIRS and SPOT-VGT, AVHRR NIR reflectance deviation was multiplicative and rapidly became greater in the negative direction until -0.025 with increasing MODIS NIR reflectance. Larger NIR reflectance deviation resulted in bigger errors under the relationship between the MODIS and AVHRR NIR reflectance (Fig. 1-4c). The differences in sensor red and NIR reflectances from MODIS could lead the variations of NDVI, and EVI between sensor and MODIS, in spite of the lower ASD-MQUALS acquisition height with the minimal atmosphere influences.

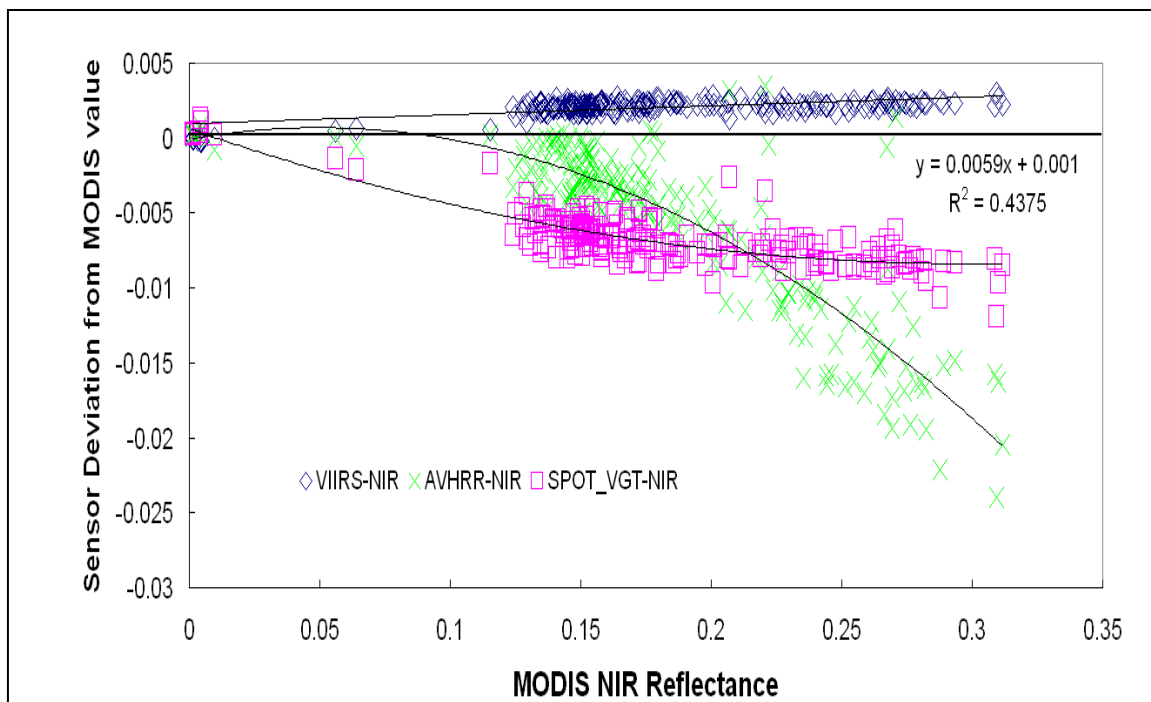
ASD-MQUALS NDVI values exhibited a wide range from 0.1 to 0.9 (Fig. 1-3d). There were linear regression relationships between sensors and MODIS NDVI, because their dissimilarity and curvilinear characteristics in red and NIR reflectance value from sensors was eliminated to some degree by the calculation of vegetation indices. We figured out that AVHRR NDVI deviated from MODIS NDVI by 10 % at MODIS NDVI of 0.85, because red and NIR reflectance between AVHRR and MODIS were notably varied in the smaller red and larger NIR reflectance values. SPOT-VGT NDVI showed 5 % differences from MODIS NDVI, while VIIRS NDVI was nearly flat line relative to MODIS NDVI. AVHRR-NDVI showed increasingly negative departures from the MODIS NDVI with increasing NDVI values. This was due to the multiplicative higher AVHRR red and lower AVHRR NIR responses found with increasing amounts of vegetation. In contrast to AVHRR, SPOT-VGT and VIIRS NDVI exhibited unique and

constant variations, with an offset of -0.05 units in SPOT-VGT NDVI and ± 0.01 unit in VIIRS NDVI.

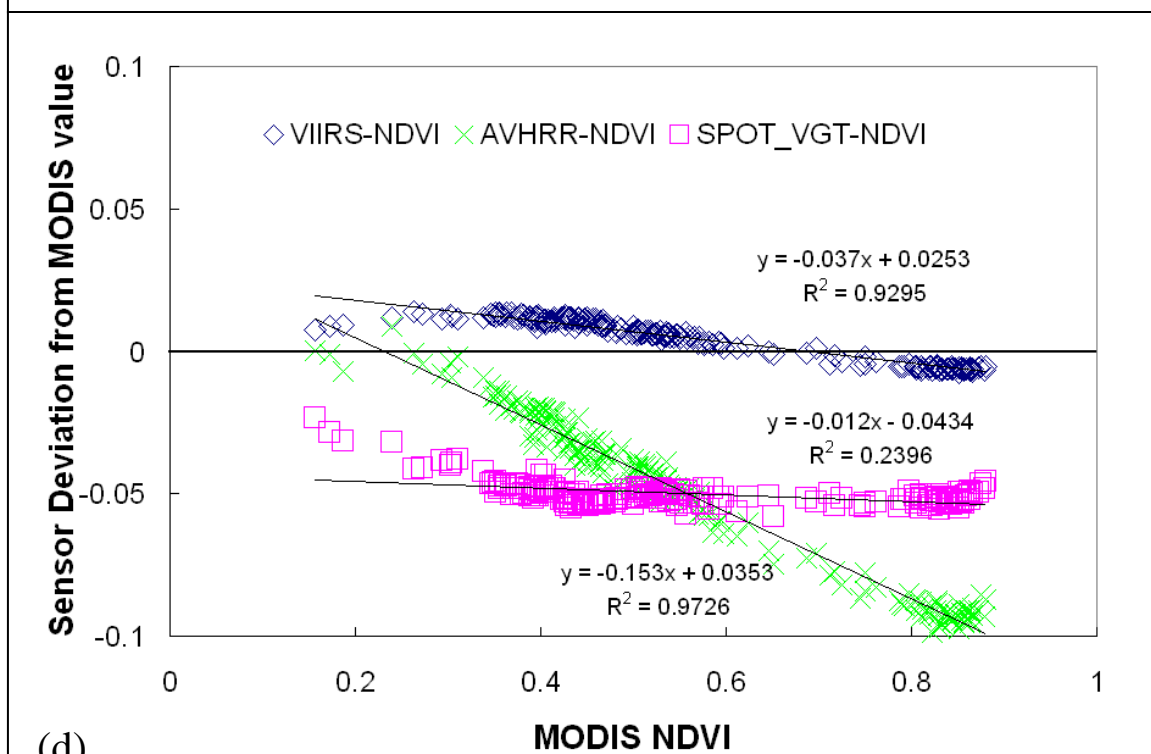
In the case of EVI (Fig. 1-4e), VIIRS EVI was very stable with an offset of +0.01 in spite of the larger deviations between MODIS and VIIRS blue reflectances (Fig. 1-4a).

The SPOT-VGT EVI showed a proportional decreasing trend with increasing MODIS EVI. This amounted to 5 % change at MODIS EVI value of 0.55. Based on this result, it appeared that the proportional decrease observed with SPOT-VGT EVI, was a result of the blue band. SPOT-VGT blue reflectance decreased proportionally relative to MODIS blue reflectance (see Fig. 1-4a), while the SPOT-VGT red and NIR deviations were not proportional but more constant offsets.



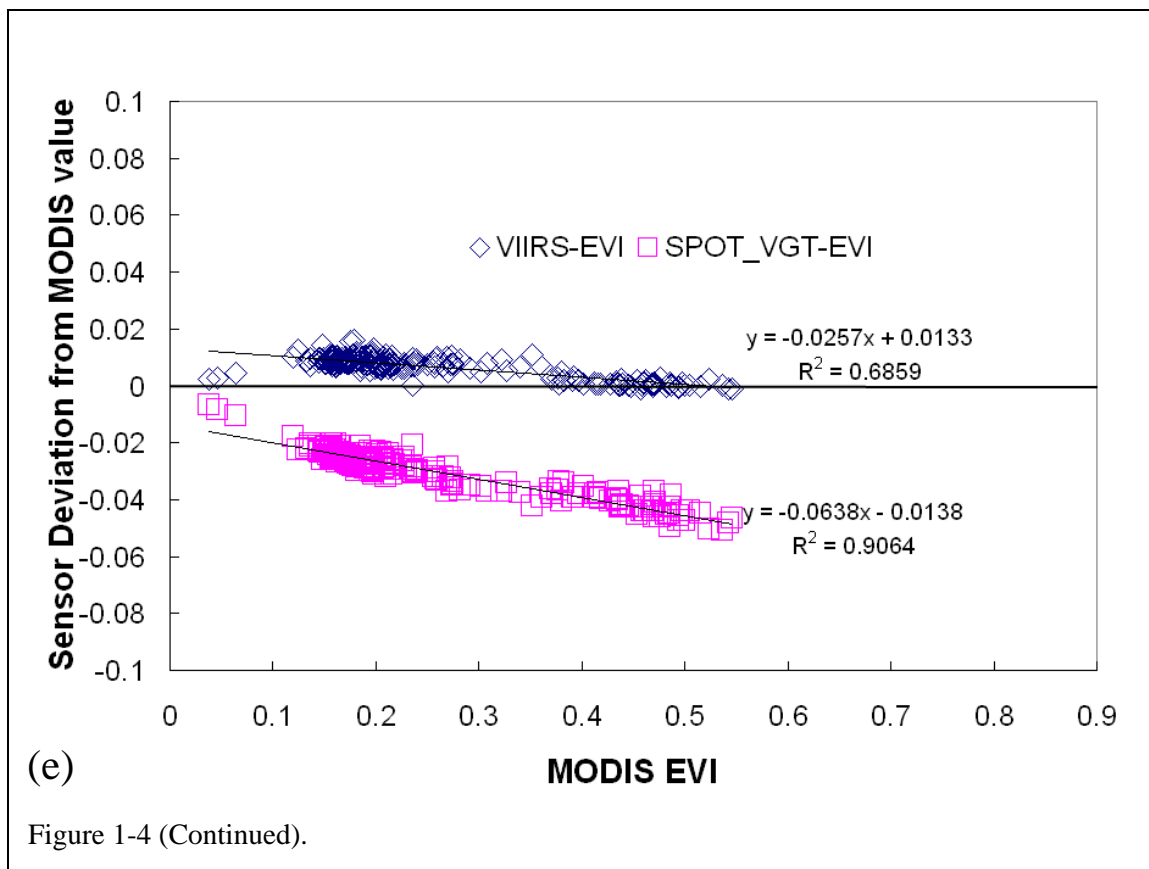


(c)



(d)

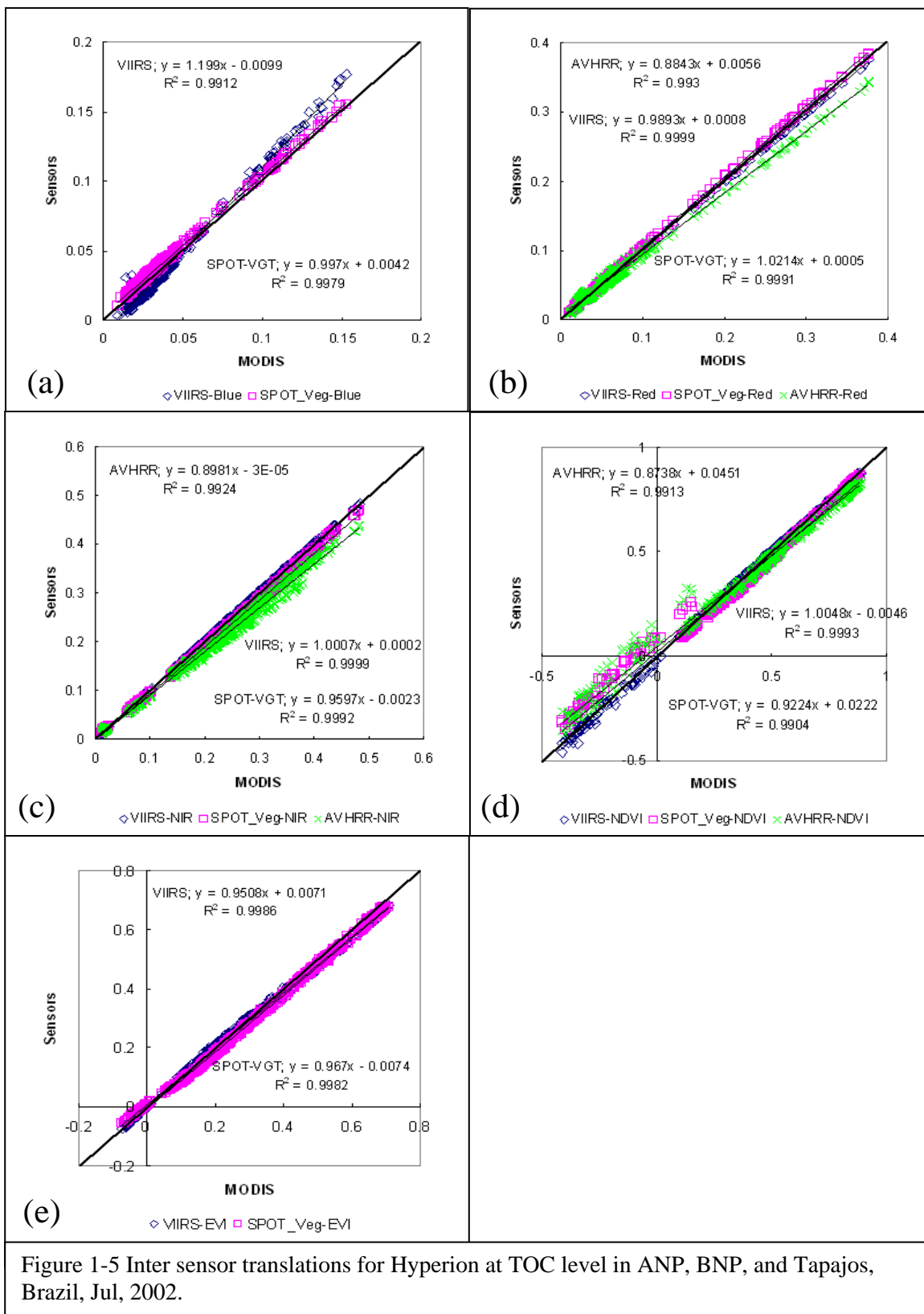
Figure 1-4 (Continued).



3.2. Spectral deviation analyses of Hyperion data across multiple sensors: Space level

In Fig. 1-5, Hyperion dataset at the TOC level was used for inter-sensor translation equations and the analyses of multiple sensor comparisons. Image acquisition height was at nearly top-of-atmosphere and it was the highest altitude compared to other hyperspectral datasets (ASD-MQUALs and AVIRIS). VIIRS blue reflectance was increased greatly with increasing MODIS blue reflectance (Fig. 1-5a) due to the large slope (1.199) as like as ASD-MQUALs dataset (1.1505) (Fig. 1-3a). In Fig. 1-6a, SPOT-VGT blue reflectance deviation was almost a constant offset with a slightly positive value. VIIRS blue reflectance deviation showed two different parts; negative and positive deviations from MODIS blue reflectance. VIIRS blue reflectance deviation became rapidly greater in the positive direction with increasing MODIS blue reflectance. VIIRS deviation in Hyperion dataset showed similar deviation to ASD-MQUALs dataset, but VIIRS deviation was mostly positive in ASD-MQUALs and positive and negative in Hyperion dataset. This seemed to result from the different sensitivity of spectral response function and atmospheric influence in blue band on the land covers between MODIS and SPOT-VGT, even though the slope change across these sites for the sensors versus MODIS blue reflectance did not show much variation (Fig. 1-6a).

In the case of the red reflectance (Fig. 1-6b), AVHRR red reflectance deviation became negative with increasing MODIS red reflectance (in ANP), in contrast with ASD-MQUALs dataset (mostly positive). The relationship between VIIRS and MODIS red

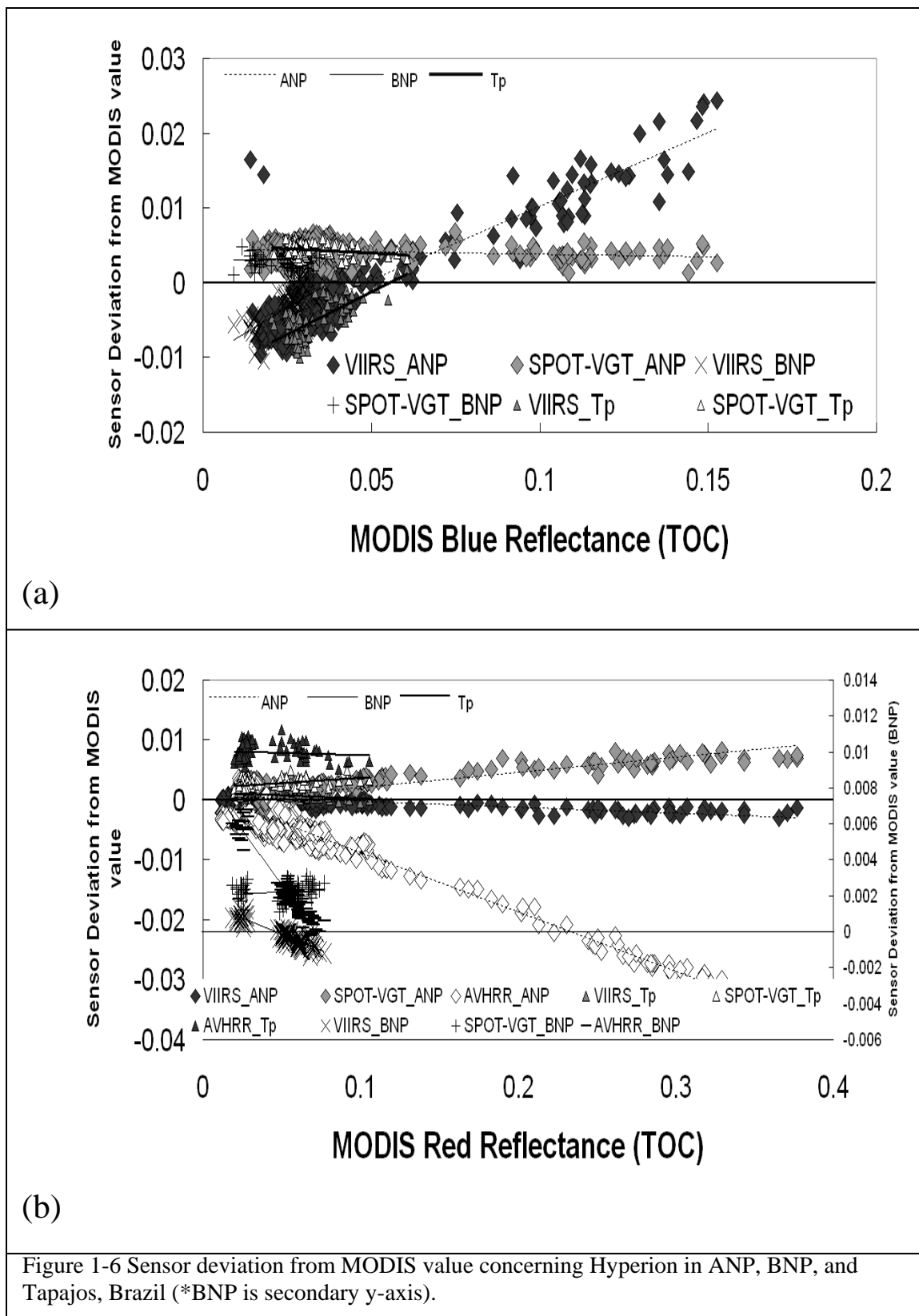


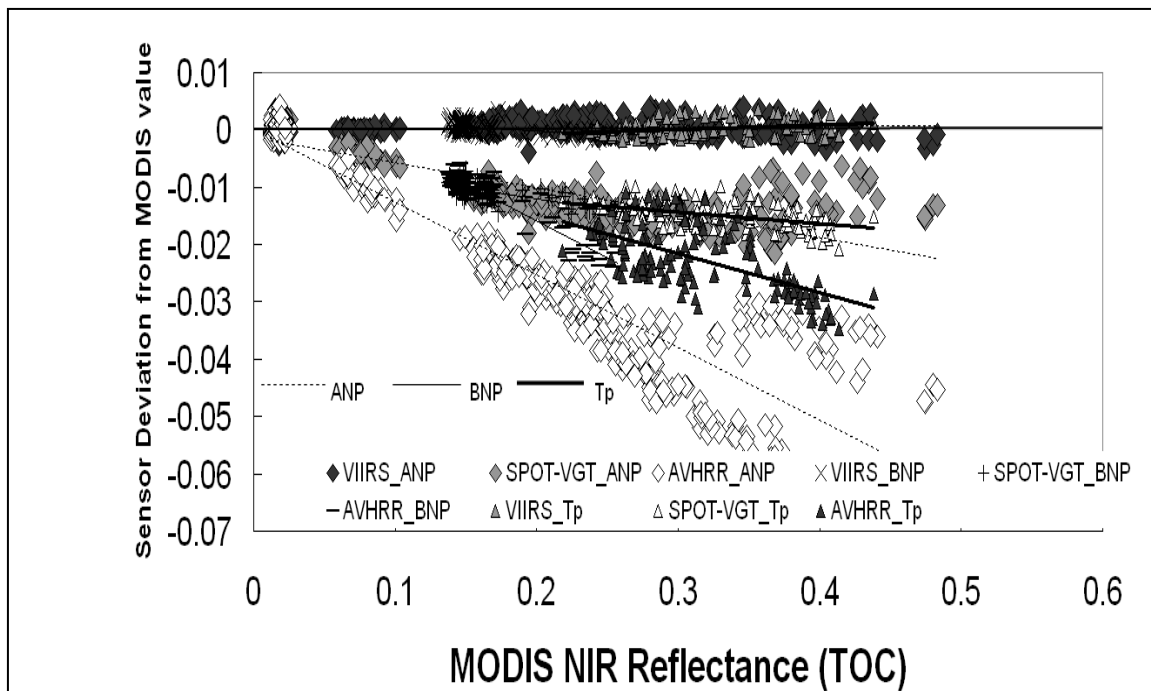
reflectance had the best linear regression (Fig. 1-5b) with a constant deviation (Fig. 1-6b). On the other hand, SPOT-VGT red reflectance deviation increased with increasing MODIS red reflectance (Fig. 1-6b). In the red reflectance (Fig. 1-6b), the slope change over different land covers was minimal except for the AVHRR sensor. In Tapajos study site, AVHRR red deviation was almost a flat line or decreased slightly with increasing MODIS red reflectance. VIIRS red deviation in Hyperion was very similar with that in ASD-MQUALs dataset (i.e. a constant offset). SPOT-VGT red deviation in Hyperion and ASD-MQUALs were both positive, while AVHRR red deviation in both datasets was not significantly related.

The relationship of the NIR reflectance between AVHRR and MODIS showed more dispersion, likely due to the included water absorption band in NIR (Fig. 1-6c). Because water absorption bands were not included in the NIR reflectance of VIIRS, MODIS, and SPOT-VGT, their relations were closely associated with its own spectral differences. VIIRS NIR reflectance deviation from the MODIS value across the three study sites was constantly zero for the whole range of MODIS NIR reflectance. The NIR deviation of AVHRR and SPOT-VGT decreased with increasing MODIS NIR reflectance. In the case of AVHRR NIR reflectance, it was divided into two directions from around MODIS NIR reflectance of 0.2. Upper area was mostly from Tapajos forest study site and the bottom area was from Araguaia and Brasilia National Park study sites. VIIRS NIR deviation in Hyperion was almost identical to that in ASD-MQUALs. SPOT-VGT and AVHRR NIR deviations decreased with increasing MODIS NIR reflectance, as like as in ASD-MQUALs.

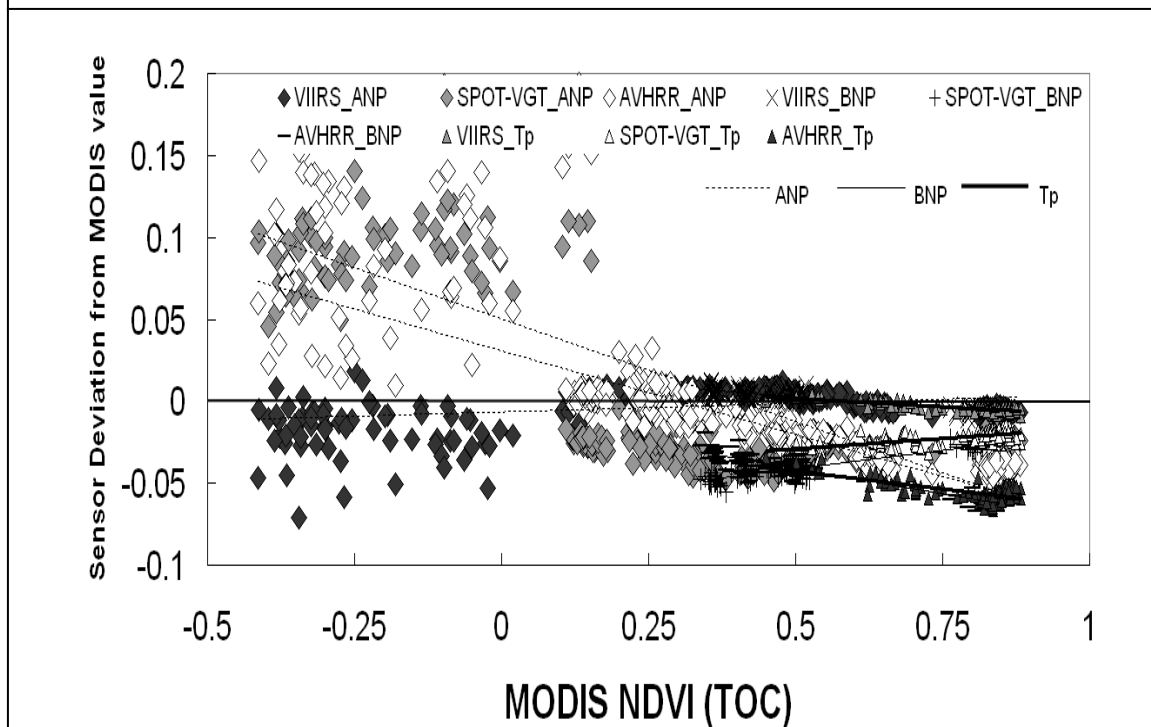
In addition to the reflectances, sensor NDVI values were compared with MODIS NDVI (Fig. 1-6d). There were some outliers from major linear trends in the negative NDVI area (mostly water region), interestingly. Sensor NDVI variations varied between -0.07 and 0.02 in MODIS NDVI values and increased with decreasing MODIS NDVI. AVHRR NDVI intersected SPOT-VGT NDVI at around MODIS NDVI of 0.6. SPOT-VGT NDVI in BNP and Tapajos study sites became greater with increasing MODIS NDVI, in contrast to ANP study site. MODIS NDVI of less than 0.1 was remarkably scattered in their deviations. AVHRR and SPOT-VGT NDVI deviations were mostly positive and VIIRS NDVI distributions were negatively less than MODIS NDVI of 0.1. Since the images obtained from Hyperion had been taken of various land cover types, the specific land covers (e.g. water in ANP study site) made NDVI negative. The relationship between VIIRS and MODIS was strongly linear in the even negative NDVI compared to other sensors (Fig. 1-5d), since the spectral response of the red and NIR band in VIIRS and MODIS was most similar, while that in AVHRR and SPOT-VGT was more discrete than MODIS and VIIRS relationships. The wide spectral range of the SPOT-VGT NIR as well as the AVHRR NIR bands could be affected by adjacent water absorption areas. Though significant differences were not detected in the NIR band of SPOT-VGT and MODIS, NDVI values of SPOT-VGT and MODIS sensors exhibited a large discrepancy in their negative values (Fig. 1-6d). The sensor NDVI deviations in Hyperion were very similar to those in ASD-MQUALs. Both datasets in SPOT-VGT increased slightly from MODIS NDVI of 0.4 in Hyperion (a flat line in ASD-MQUALs dataset) (Fig. 1-4d and Fig. 1-6d).

In the case of EVI (Fig. 1-6e), they had a smaller dynamic range than that of NDVI. There were fewer distributions in the negative MODIS EVI compared with negative NDVI. VIIRS EVI deviations from MODIS values in BNP and in some parts of ANP study sites were about zero until the MODIS EVI showed a value of 0.35 (Fig 1-6e). In Tapajos and some other areas of ANP study site, the VIIRS EVI deviation decreased with increasing MODIS EVI. Its deviation decreased slightly by -0.04 . The EVI deviations in SPOT-VGT and VIIRS crossed at MODIS EVI of 0.7. SPOT-VGT EVI deviation was mostly negative relative to MODIS EVI values. The slope of SPOT-VGT EVI deviation in BNP and Tapajos study sites remained almost zero. In contrast to ASD-MQUALs, SPOT-VGT red reflectance deviation was proportionally increased relative to MODIS Red reflectance (Fig 1-4b and Fig. 1-6b), while SPOT-VGT NIR reflectance deviation decreased proportionally relative to MODIS NIR reflectance (Fig. 1-4c and Fig. 1-6c). SPOT-VGT blue reflectance deviation was not proportional but produced more constant offsets. It showed less influence in the blue band on EVI, as far as the constant deviation from the MODIS EVI value (Fig. 1-6e), due to the similarity of spectral response function in the blue band between SPOT-VGT and MODIS. In ASD-MQUALs, SPOT-VGT blue deviations decreased proportionally, resulting in the SPOT-VGT EVI deviation decreased, too (Fig. 1-4a, d).



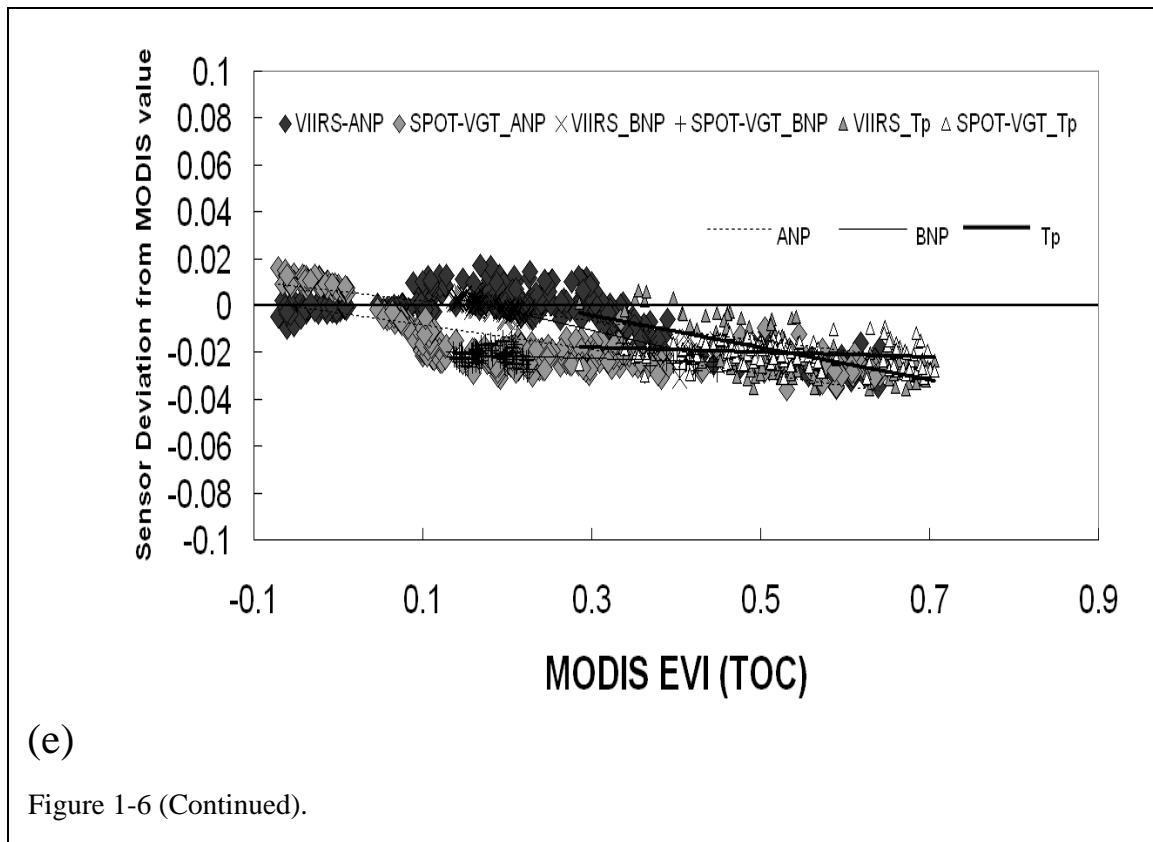


(c)



(d)

Figure 1-6 (Continued).



3.3. Spectral deviation analyses of AVIRIS data across multiple sensors:

Airplane level

Figs. 1-7 and 1-8 display AVIRIS data analyses as an intermediate image acquisition height between space-level and canopy-level. Surface reflectance from AVIRIS data needed to be corrected by 6S, because AVIRIS data had been taken at an altitude high enough to be influenced by the local atmospheric status. Most analyses were much closer to ASD-MQUALs results than Hyperion results. As the MODIS blue reflectance was increased, the VIIRS blue reflectance deviation was increased and SPOT-VGT reflectance deviation decreased slightly (Fig. 1-8a). The higher MODIS blue reflectance

described brighter objects (e.g. desert and grassland) and the lower MODIS blue reflectance showed darker objects (e.g. vegetated areas).

In contrast to Hyperion results (Fig. 1-6b, c), AVIRIS red and NIR reflectance deviations were less scattered in comparison with the MODIS red and NIR reflectance (Fig. 1-8b, c). The deviation of VIIRS red reflectance was nearly zero at the lower MODIS red reflectance in the vegetated region (e.g. Pinyon-Juniper, Ponderosa Pine, and Mixed Conifer forest), while the VIIRS red reflectance deviation became negative at the higher MODIS red reflectance in the desert and grassland area (Fig. 1-8b). The AVHRR red reflectance was a little higher (up to 0.01) than the MODIS red reflectance in the vegetated areas such as shown in the Hyperion dataset in Tapajos study site, while the AVHRR red reflectance was slightly less (up to ~ 0.008) than the MODIS red reflectance in the desert and grassland (Fig. 1-8b). In contrast to AVHRR and VIIRS sensors, SPOT-VGT red reflectance was somewhat larger than the MODIS red reflectance across the five ecosystems similar to ASD-MQUALs and Hyperion datasets (Fig. 1-8b).

The VIIRS NIR reflectance was nearly identical to the MODIS NIR reflectance as same as ASD-MQUALs and Hyperion datasets (Fig. 1-7c and Fig. 1-8c). SPOT-VGT NIR reflectance was slightly smaller than MODIS NIR reflectance (Fig. 1-7c and Fig. 1-8c). SPOT-VGT NIR reflectance deviation decreased with increasing MODIS NIR reflectance as same as ASD-MQUALs and Hyperion datasets (Fig. 1-8c). For AVHRR sensor, there were two directions of the distribution. The positive deviation represented the desert region, zero deviation was the grassland, and negative deviations showed the

vegetated areas (Pinyon-Juniper woodlands, Ponderosa Pine forest, and Mixed conifer forest) (Fig. 1-8c).

In terms of vegetation indices, the MODIS NDVI values were slightly lower than VIIRS and SPOT-VGT NDVI except for some parts of AVHRR NDVI (Fig. 1-7d). AVHRR NDVI deviation depended on vegetation density. That is to say, AVHRR NDVI was larger than the MODIS NDVI over desert and grassland areas (NDVI; 0.06 – 0.12), while AVHRR NDVI was smaller than MODIS NDVI over the vegetated areas (Pinyon-Juniper woodlands, Ponderosa Pine forest, and Mixed conifer forest) (Fig. 1-8d). A wider spectral response of red and NIR in AVHRR lead positive NDVI deviations at high biomass area, and negative NDVI and EVI2 deviation at the regions with no or sparse vegetation. The NDVI deviation trend showed the similarity to the NIR deviation in AVIRIS datasets. The SPOT-VGT NDVI deviation was different in that the deviation was slightly increased with increasing MODIS NDVI above MODIS NDVI of 0.3.

The VIIRS EVI deviation was almost constant with an offset of ~ 0.01 reflectance units. In contrast to SPOT-VGT NDVI deviation, SPOT-VGT EVI deviation decreased with increasing MODIS EVI values across all types of land cover due to the decreasing SPOT-VGT blue reflectance (Fig. 1-8e).

3.4. Comparing linear regression equation

There were three sets of data for different hyperspectral platforms and three regression equations derived from each platform. We might then ask whether the slopes and intercepts of these lines are significantly different or whether they might be only

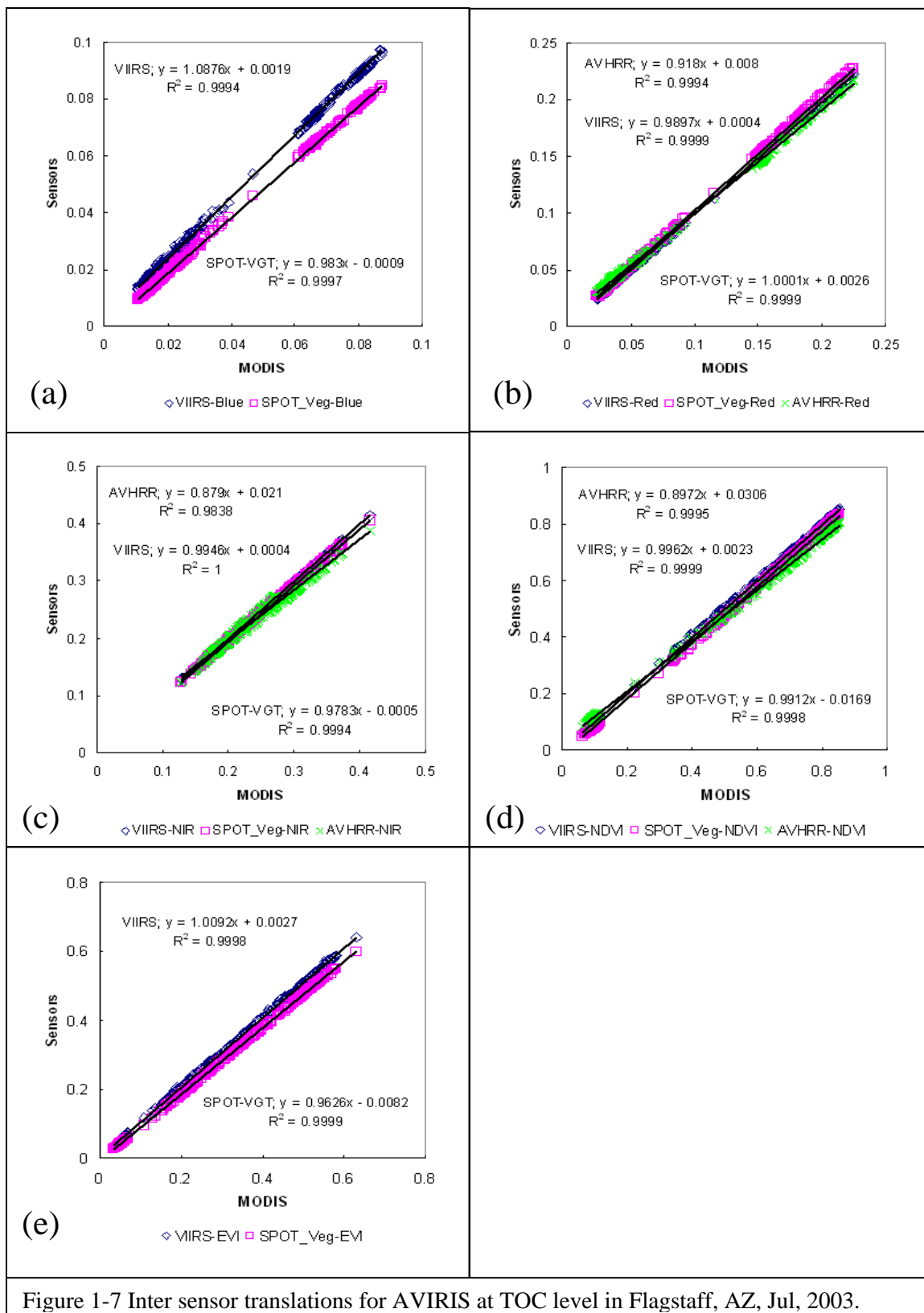
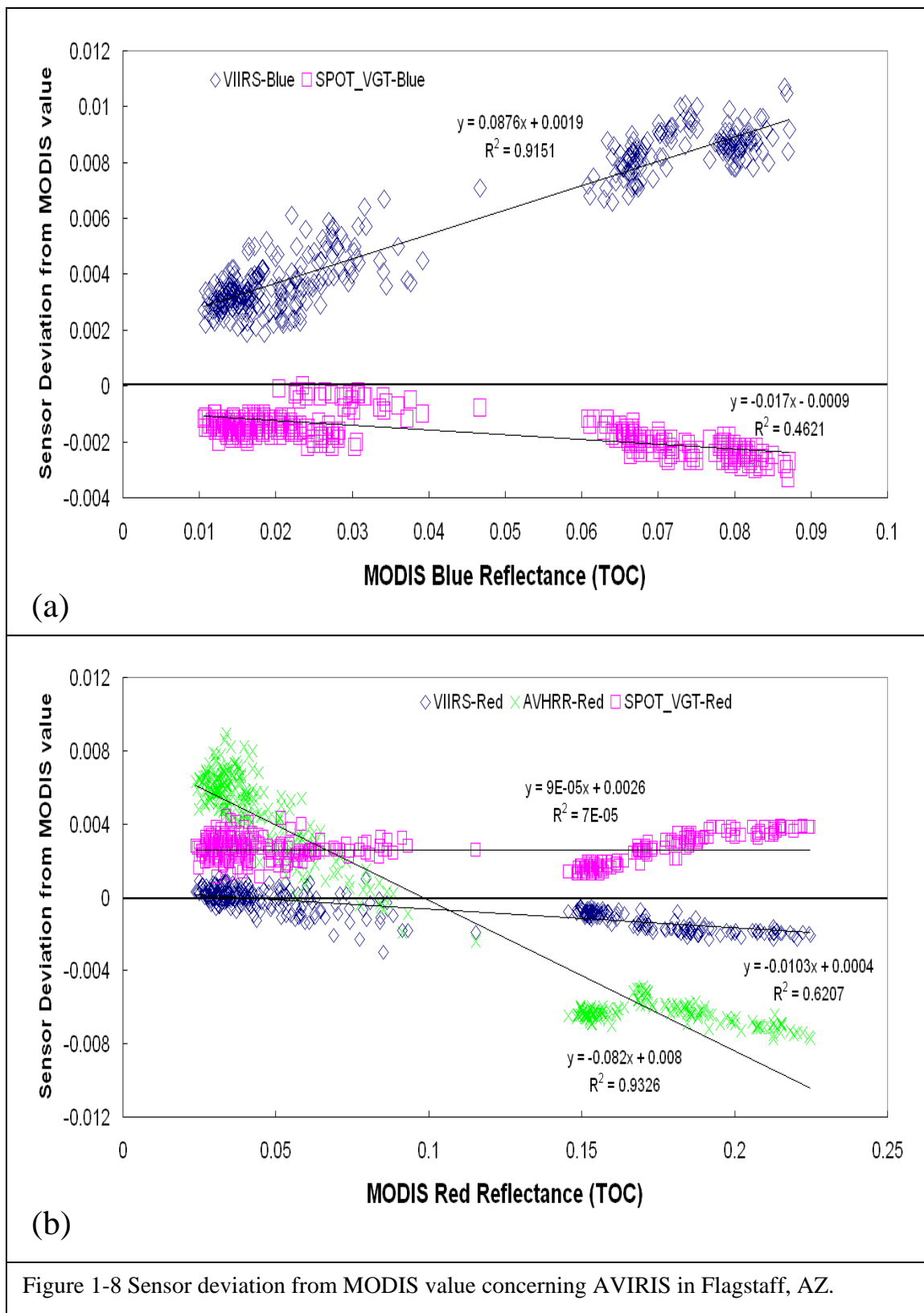
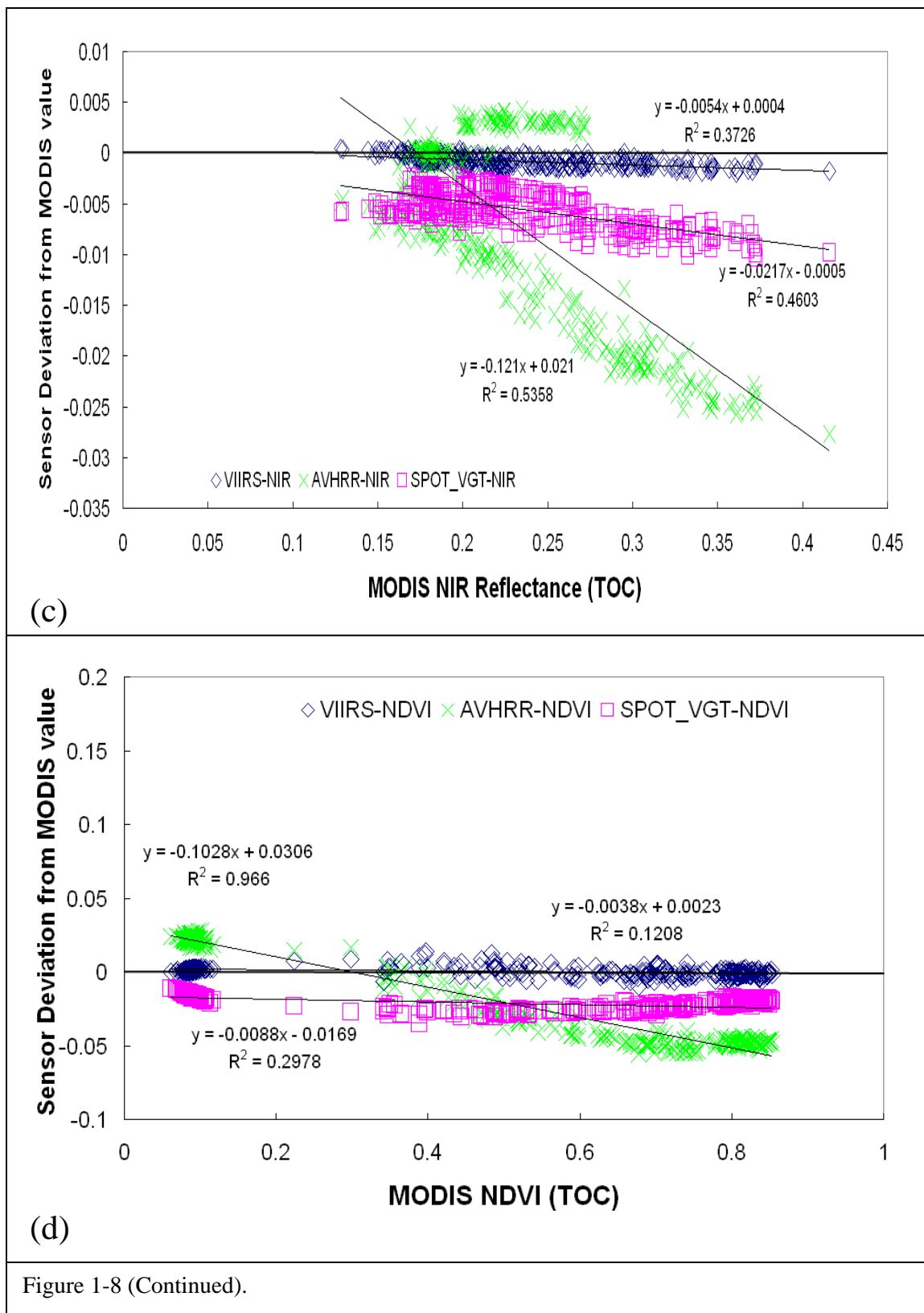
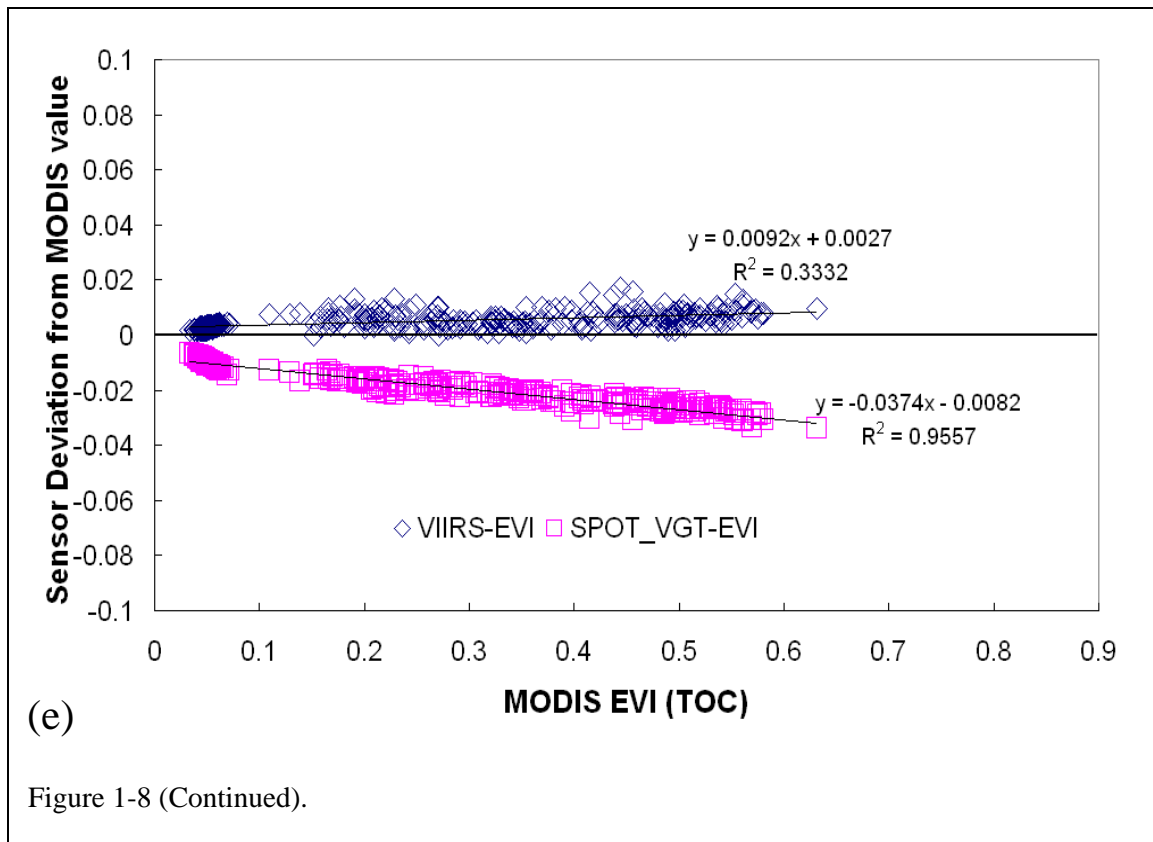


Figure 1-7 Inter sensor translations for AVIRIS at TOC level in Flagstaff, AZ, Jul, 2003.







estimating the same reflectance or VI value. A simple method for testing hypothesis about equality of two regression coefficients involved the use of Student's t test. In this section, statistical values for testing similarities among regression lines were presented as summarized in Table 1-6. A simple method for testing hypothesis about equality of two linear regression coefficients was chosen by the use of Student's t-test in a fashion analogous to that of testing for differences between two means. In biology, 95% confident level is recommended, but stricter criteria for agreement are needed. In this study, 99% confidence level was selected. The t-values were calculated as following (Zar 1999):

$$t = \frac{slope1 - slope2}{S_{b1} - S_{b2}} \quad [5]$$

$$, \text{ where } S_{b1} - S_{b2} = \sqrt{\frac{(S^2_{Y.X})_p}{\sum x_{sample1}^2} + \frac{(S^2_{Y.X})_p}{\sum x_{sample2}^2}} \quad [6]$$

$$\text{and } (S^2_{Y.X})_p = \frac{\text{residual } SS_{sample1} + \text{residual } SS_{sample2}}{\text{residual } DF_{sample1} + \text{residual } DF_{sample2}} \quad [7]$$

(residual SS: residual Sum of Square and residual DF: residual Degree of Freedom)

When we assume the slopes and intercepts of linear regression are same ($H_0: \beta_1 = \beta_2$), we cannot reject this hypothesis with 99% confidence level, because all $|t|$ were less than 2.58. It implied that the slopes and intercepts of linear regression equations derived from three hyperspectral datasets were not significantly different with respect to MODIS reflectances and VIs with 99% confidence level. The statistical results were provided in Table 1-4 and the three t-values were shown regarding reflectances and VI's.

In order to examine the significant difference of inter-sensor equations within one dataset, $|t|$ values for the slope and intercept were computed in Table 1-5. For the most part, they were not significant difference within one dataset, but there were some significant differences: in the blue reflectance between VIIRS from Hyperion and SPOT-VGT from Hyperion, in the red reflectance between AVHRR from Hyperion and SPOT-VGT from Hyperion, in the NDVI between VIIRS from Hyperion and AVHRR from Hyperion. It was hard to make universal translation equations for the reflectances and vegetation indices, irrespective of sensor types.

Table 1-4 Comparison of linear regression equation regarding MODIS

	Sensor	Sensor	vs.	SAMPLE 1			SAMPLE 2			$ t _{\text{slope}}$	$ t _{\text{intercept}}$	
				$\sum x^2$	$\sum xy$	$\sum y^2$	$\sum x^2$	$\sum xy$	$\sum y^2$			
Blue	ASD_MQUALs	AVIRIS	VIIRS	0.156581	0.000196	0.186225	1.253031	0.008159	1.57051	0.463394	0.026522	ND
	ASD_MQUALs	Hyperion	VIIRS	0.156581	0.000196	0.186225	1.179299	0.011607	1.220337	0.437779	0.074016	ND
	AVIRIS	Hyperion	VIIRS	1.253031	0.008159	1.57051	1.179299	0.011607	1.220337	1.725451	0.182768	ND
	ASD_MQUALs	AVIRIS	SPOT-VGT	0.156581	0.00015	0.145708	1.253031	0.006195	1.174913	0.229417	0.009347	ND
	ASD_MQUALs	Hyperion	SPOT-VGT	0.156581	0.00015	0.145708	1.179299	0.010182	1.374424	0.355984	0.034730	ND
	AVIRIS	Hyperion	SPOT-VGT	1.253031	0.006195	1.174913	1.179299	0.010182	1.374424	0.22688	0.082649	ND
Red	ASD_MQUALs	AVIRIS	VIIRS	0.621865	0.003542	0.612221	6.886413	0.001692	6.780934	0.175922	0.027841	ND
	ASD_MQUALs	Hyperion	VIIRS	0.621865	0.003542	0.612221	5.018387	0.31129	4.976147	0.215996	0.058980	ND
	AVIRIS	Hyperion	VIIRS	6.886413	0.001692	6.780934	5.018387	0.31129	4.976147	0.006604	0.006604	ND
	ASD_MQUALs	AVIRIS	AVHRR	0.621865	0.003949	0.735489	6.886413	0.016107	6.543062	0.23738	0.027841	ND
	ASD_MQUALs	Hyperion	AVHRR	0.621865	0.003949	0.735489	5.018387	0.259461	4.346519	0.012367	0.058980	ND
	AVIRIS	Hyperion	AVHRR	6.886413	0.016107	6.543062	5.018387	0.259461	4.346519	0.577964	0.041161	ND
	ASD_MQUALs	AVIRIS	SPOT-VGT	0.621865	0.00419	0.740758	6.886413	0.004617	7.137557	0.044365	0.016901	ND
	ASD_MQUALs	Hyperion	SPOT-VGT	0.621865	0.00419	0.740758	5.018387	0.329288	5.27485	0.131218	0.039365	ND
	AVIRIS	Hyperion	SPOT-VGT	6.886413	0.004617	7.137557	5.018387	0.329288	5.27485	0.342246	0.033743	ND
NIR	ASD_MQUALs	AVIRIS	VIIRS	7.506029	0.000938	7.669503	25.72381	0.000417	25.53681	0.123715	0.006569	ND
	ASD_MQUALs	Hyperion	VIIRS	7.506029	0.000938	7.669503	38.61088	0.001034	38.71319	0.05511	0.008479	ND
	AVIRIS	Hyperion	VIIRS	25.72381	0.000417	25.53681	38.61088	0.001034	38.71319	0.099262	0.003254	ND
	ASD_MQUALs	AVIRIS	AVHRR	7.506029	0.013478	6.975614	25.72381	0.057805	24.08898	0.548989	0.155075	ND
	ASD_MQUALs	Hyperion	AVHRR	7.506029	0.013478	6.975614	38.61088	0.449821	31.18318	0.343548	0.085653	ND
	AVIRIS	Hyperion	AVHRR	25.72381	0.057805	24.08898	38.61088	0.449821	31.18318	0.335114	0.368976	ND
	ASD_MQUALs	AVIRIS	SPOT-VGT	7.506029	0.009822	6.983549	25.72381	0.01523	24.52046	0.055077	0.049457	ND
	ASD_MQUALs	Hyperion	SPOT-VGT	7.506029	0.009822	6.983549	38.61088	0.097707	34.95387	0.152696	0.025635	ND
	AVIRIS	Hyperion	SPOT-VGT	25.72381	0.01523	24.52046	38.61088	0.097707	34.95387	0.314586	0.035518	ND

Table 1-4 (Cont.)

	Sensor	Sensor	vs.	SAMPLE 1			SAMPLE 2			$ t _{\text{slope}}$	$ t _{\text{intercept}}$	
				$\sum x^2$	$\sum xy$	$\sum y^2$	$\sum x^2$	$\sum xy$	$\sum y^2$			
NDVI	ASD_MQUALs	AVIRIS	VIIRS	71.36446	34.45207	72.17395	127.6582	68.28834	127.6055	0.043872	0.030710	ND
	ASD_MQUALs	Hyperion	VIIRS	71.36446	34.45207	72.17395	220.4934	119.8606	219.8536	0.081651	0.131225	ND
	AVIRIS	Hyperion	VIIRS	127.6582	68.28834	127.6055	220.4934	119.8606	219.8536	0.163742	0.131374	ND
	ASD_MQUALs	AVIRIS	AVHRR	71.36446	28.08408	59.12784	127.6582	60.44628	114.2022	0.366068	0.588160	ND
	ASD_MQUALs	Hyperion	AVHRR	71.36446	28.08408	59.12784	220.4984	106.7759	194.3476	0.724098	0.809827	ND
	AVIRIS	Hyperion	AVHRR	127.6582	60.44628	114.2022	220.4984	106.7759	194.3476	0.462346	0.286497	ND
	ASD_MQUALs	AVIRIS	SPOT-VGT	71.36446	29.63322	59.95933	127.6582	64.48977	118.8802	0.895023	0.087207	ND
	ASD_MQUALs	Hyperion	SPOT-VGT	71.36446	29.63322	59.95933	220.4984	113.2198	201.1018	0.157719	0.511437	ND
	AVIRIS	Hyperion	SPOT-VGT	127.6582	64.48977	118.8802	220.4984	113.2198	201.1018	1.356273	0.770789	ND
EVI	ASD_MQUALs	AVIRIS	VIIRS	16.80322	2.660032	17.33885	39.30136	8.215987	40.61632	0.293261	0.086536	ND
	ASD_MQUALs	Hyperion	VIIRS	16.80322	2.660032	17.33885	82.21084	20.59053	76.90505	0.388321	0.031979	ND
	AVIRIS	Hyperion	VIIRS	39.30136	8.215987	40.61632	82.21084	20.59053	76.90505	0.95037	0.071603	ND
	ASD_MQUALs	AVIRIS	SPOT-VGT	16.80322	2.14884	13.41526	39.30136	7.134171	34.75462	0.489323	0.028938	ND
	ASD_MQUALs	Hyperion	SPOT-VGT	16.80322	2.14884	13.41526	82.21084	20.54057	74.29958	0.493131	0.035562	ND
	AVIRIS	Hyperion	SPOT-VGT	39.30136	7.134171	34.75462	82.21084	20.54057	74.29958	0.074348	0.013518	ND

$X=MODIS$ value and $y=sensor$ value

$$t_{0.01(2),700} = 2.583, t_{0.01(2),800} = 2.582 \text{ and } t_{0.01(2),1000} = 2.581$$

$V = 685$ for ASD-MQUALs and AVIRIS, 829 for ASD_MQUALs and Hyperion, and 1102 for AVIRIS and Hyperion

ND=Not significantly different

Table 1-5 Comparison of linear regression equation within one dataset

	Sensor	Sample1	Sample2	SAMPLE 1			SAMPLE 2			$ t _{\text{slope}}$	$ t _{\text{intercept}}$	
				$\sum x^2$	$\sum xy$	$\sum y^2$	$\sum x^2$	$\sum xy$	$\sum y^2$			
Blue	ASD_MQUALs	VIIRS	SPOT-VGT	0.156581	0.000196	0.186225	0.156581	0.00015	0.145708	1.917336	0.018730	ND
	AVIRIS	VIIRS	SPOT-VGT	1.253031	0.008159	1.570510	1.253031	0.006195	1.174913	1.546615	0.010350	ND
	Hyperion	VIIRS	SPOT-VGT	1.179299	0.011607	1.220337	1.179299	0.010182	1.374424	3.399192	0.237270	SD
Red	ASD_MQUALs	VIIRS	AVHRR	0.621815	0.003542	0.612221	0.621815	0.003949	0.735489	0.779000	0.001950	ND
	ASD_MQUALs	VIIRS	SPOT-VGT	0.621815	0.003542	0.612221	0.621815	0.004190	0.740758	0.397986	0.064223	ND
	ASD_MQUALs	AVHRR	SPOT-VGT	0.621815	0.003949	0.735489	0.621815	0.004190	0.740758	1.125323	0.063346	ND
	AVIRIS	VIIRS	AVHRR	6.886413	0.001692	6.780934	6.886413	0.016107	6.543062	1.128150	0.119581	ND
	AVIRIS	VIIRS	SPOT-VGT	6.886413	0.001692	6.780934	6.886413	0.004617	7.137557	0.160104	0.033868	ND
	AVIRIS	AVHRR	SPOT-VGT	6.886413	0.016107	6.543062	6.886413	0.004617	7.137557	1.274839	0.083851	ND
	Hyperion	VIIRS	AVHRR	5.018387	0.311290	4.976147	5.018387	0.259461	4.346519	1.926233	0.088056	ND
	Hyperion	VIIRS	SPOT-VGT	5.018387	0.311290	4.976147	5.018387	0.329288	5.274850	0.561716	0.00525	ND
	Hyperion	AVHRR	SPOT-VGT	5.018387	0.259461	4.346519	5.018387	0.329288	5.274850	2.475922	0.092102	SD
NIR	ASD_MQUALs	VIIRS	AVHRR	7.506029	0.000938	7.669503	7.506029	0.013478	6.975614	0.805580	0.064734	ND
	ASD_MQUALs	VIIRS	SPOT-VGT	7.506029	0.000938	7.669503	7.506029	0.009822	6.983549	0.333855	0.028763	ND
	ASD_MQUALs	AVHRR	SPOT-VGT	7.506029	0.013478	6.975614	7.506029	0.009822	6.983549	0.483084	0.095775	ND
	AVIRIS	VIIRS	AVHRR	25.72381	0.000417	25.53681	25.72381	0.057805	24.08898	1.821546	0.324601	ND
	AVIRIS	VIIRS	SPOT-VGT	25.72381	0.000417	25.53681	25.72381	0.015230	24.52046	0.255735	0.034516	ND
	AVIRIS	AVHRR	SPOT-VGT	25.72381	0.057805	24.08898	25.72381	0.015230	24.52046	1.580975	0.292950	ND
	Hyperion	VIIRS	AVHRR	38.61088	0.001034	38.71319	38.61088	0.449821	31.18318	1.903423	0.385879	ND
	Hyperion	VIIRS	SPOT-VGT	38.61088	0.001034	38.71319	38.61088	0.097707	34.95387	0.740878	0.043368	ND
	Hyperion	AVHRR	SPOT-VGT	38.61088	0.449821	31.18318	38.61088	0.097707	34.95387	1.174830	0.350923	ND
NDVI	ASD_MQUALs	VIIRS	AVHRR	71.36446	34.45207	72.17395	71.36446	28.08408	59.12784	0.930269	0.145317	ND
	ASD_MQUALs	VIIRS	SPOT-VGT	71.36446	34.45207	72.17395	71.36446	29.63322	59.95933	0.793714	0.186195	ND
	ASD_MQUALs	AVHRR	SPOT-VGT	71.36446	28.08408	59.12784	71.36446	29.63322	59.95933	0.143750	0.042134	ND
	AVIRIS	VIIRS	AVHRR	127.6582	68.28834	127.6065	127.6582	60.44628	114.2022	1.841878	0.526517	ND
	AVIRIS	VIIRS	SPOT-VGT	127.6582	68.28834	127.6065	127.6582	64.48977	118.8802	0.092835	0.051988	ND
	AVIRIS	AVHRR	SPOT-VGT	127.6582	60.44628	114.2022	127.6582	64.48977	118.8802	1.772983	0.586593	ND
	Hyperion	VIIRS	AVHRR	220.4984	119.8606	219.8536	220.4984	106.7759	194.3476	2.815732	0.098228	SD
	Hyperion	VIIRS	SPOT-VGT	220.4984	119.8606	219.8536	220.4984	113.2198	201.1018	1.770149	0.049410	ND
	Hyperion	AVHRR	SPOT-VGT	220.4984	106.7759	194.3476	220.4984	113.2198	201.1018	1.065854	0.049784	ND
EVI	ASD_MQUALs	VIIRS	SPOT-VGT	16.80322	2.660032	17.33885	16.80322	2.148840	13.41526	0.637433	0.217843	ND
	AVIRIS	VIIRS	SPOT-VGT	39.30136	8.215987	40.61632	39.30136	7.134171	34.75462	0.751646	0.175814	ND
	Hyperion	VIIRS	SPOT-VGT	82.21084	20.59053	76.90505	82.21084	20.54057	74.29958	0.308848	0.276438	ND

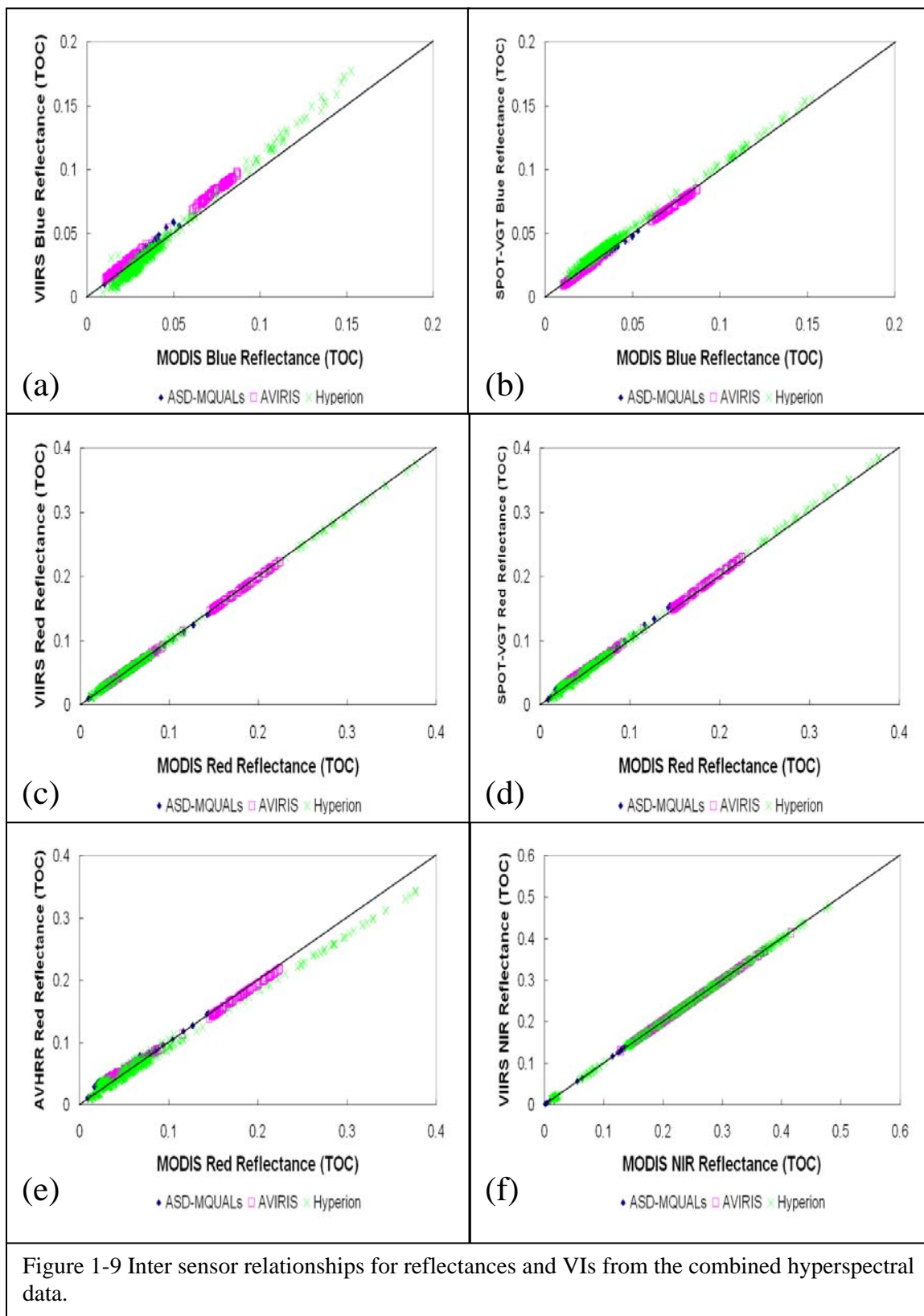
$X = \text{MODIS value and } y = \text{sensor value. } t_{0.01(2),700} = 2.583, t_{0.01(2),800} = 2.582 \text{ and } t_{0.01(2),1000} = 2.581$

$V = 685 \text{ for ASD-MQUALs and AVIRIS, } 829 \text{ for ASD_MQUALs and Hyperion, and } 1102 \text{ for AVIRIS and Hyperion, ND=Not significantly different and SD = significantly different}$

3.5. The combined cross sensor analyses

The combined inter-sensor relationships between sensor and MODIS reflectances and VIs were provided in Fig. 1-9. As for the blue reflectance, ASD-MQUALs and AVIRIS datasets showed close relationships with the MODIS blue reflectance for the VIIRS and SPOT-VGT sensors. In Hyperion data, the VIIRS blue reflectance became larger with the increasing MODIS blue reflectance (Fig. 1-9a), while the SPOT-VGT blue reflectance became larger with the decreasing MODIS blue reflectance (Fig. 1-9b). As for the red reflectances (Fig. 1-9c, d, e), the VIIRS and MODIS red reflectances consistently agreed with the MODIS red reflectances. The AVHRR red reflectances in Hyperion decreased slightly with increasing MODIS red reflectance. In the case of the NIR reflectances, linear relationship between VIIRS/SPOT-VGT and MODIS sensor was established with the least deviation (Fig. 1-9f, g)). In contrast, the AVHRR NIR reflectances were gradually departed with the increasing MODIS NIR reflectances, even for ASD-MQUALs and AVIRIS data (Fig. 1-9h).

As far as the vegetation indices, many contaminated pixels were shown in the negative NDVI area (most water regions) (Fig. 1-9i, j, and k). Visually it seemed to fit best between VIIRS and MODIS NDVI over three sensors. In the case of AVHRR and SPOT-VGT sensors, their NDVI value decreased with increasing MODIS NDVI value. As for the EVI (Fig. 1-9l, m), VIIRS EVI from ASD-MQUALs and AVIRIS was very close to the MODIS EVI, while VIIRS EVI from Hyperion was slightly smaller than MODIS EVI in the higher EVI values. In contrast to VIIRS sensor, most of the SPOT-VGT EVI values were smaller than MODIS EVI across all three datasets.



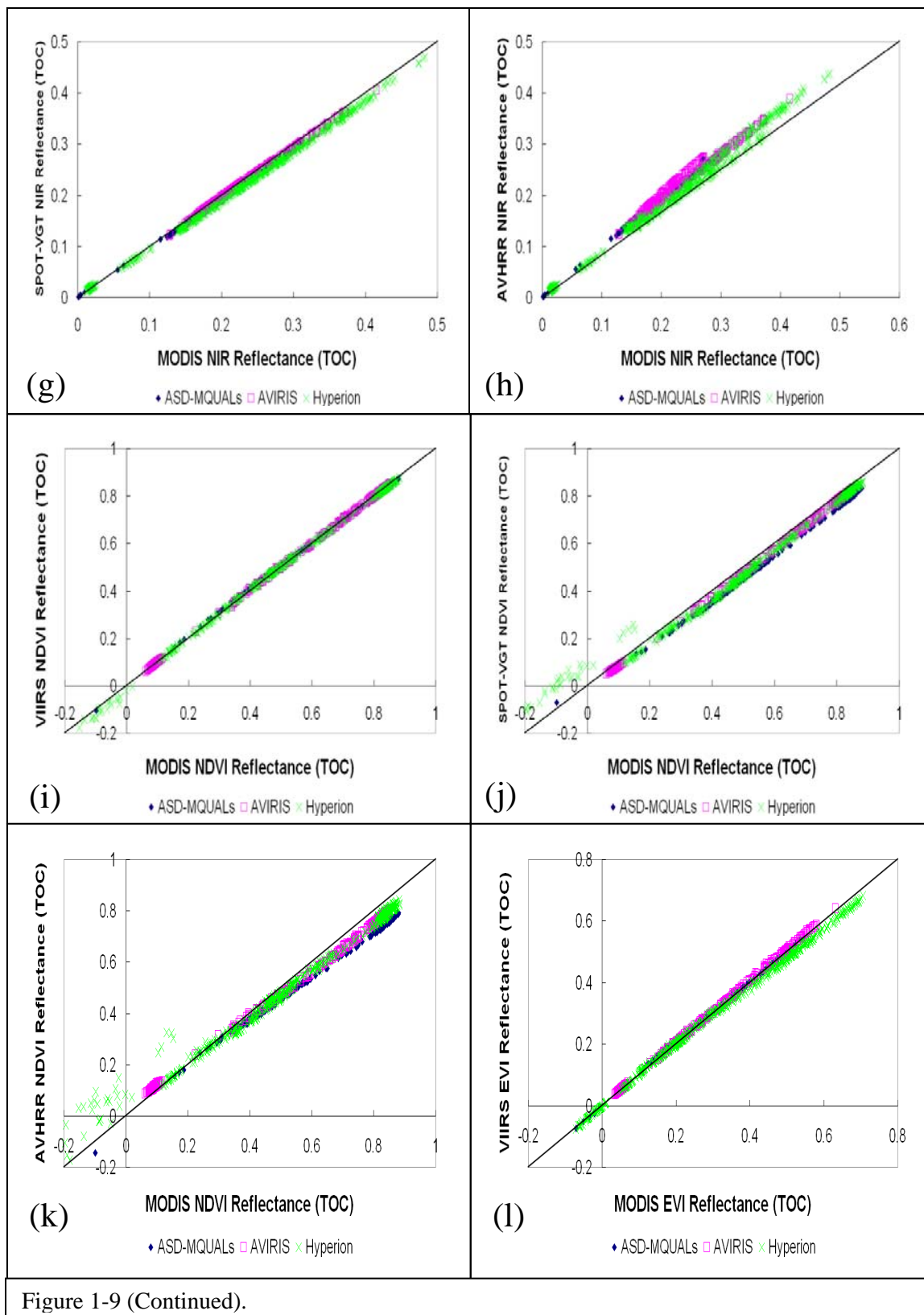
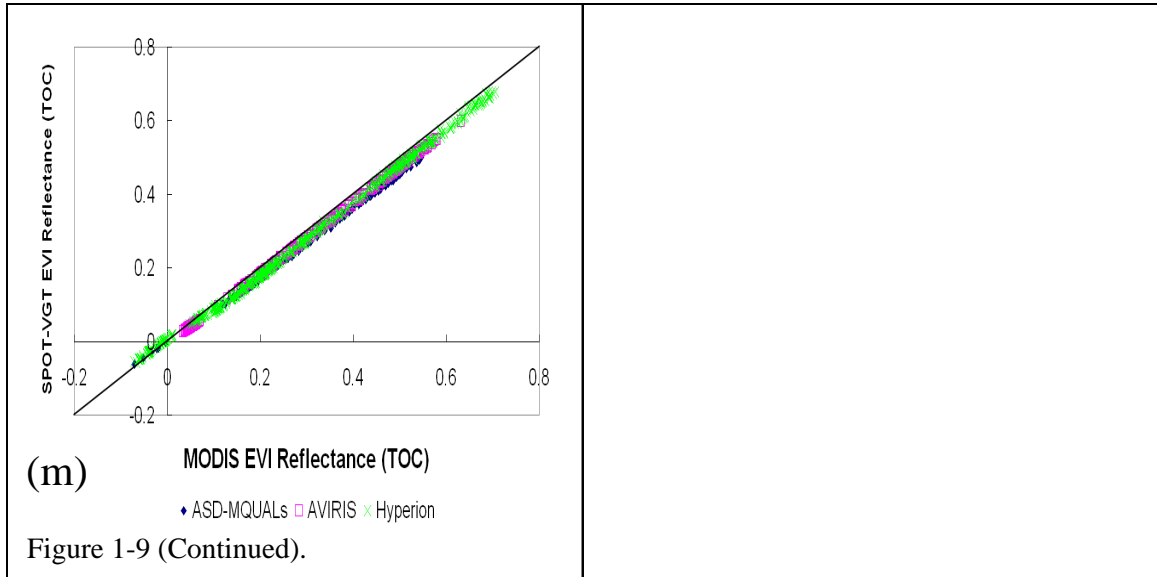


Figure 1-9 (Continued).



Inter-sensor transforms from three different datasets (ASD-MQUALs, Hyperion, and AVIRIS) are presented in Table 1-6. The Root Mean Square Error (RMSE) of the difference between the transformed and the convolved sensor value was computed to explain which inter-sensor translation equations derived from three hyperspectral platforms reproduce sensor reflectances and vegetation indices from MODIS values

accurately. RMSE is calculated as:
$$\sqrt{\frac{E((\hat{\theta} - \theta))^2}{N}} \quad [8]$$

where E: mean, $\hat{\theta}$: the predicted value by model (the transformed value), and θ : the actual observed value (the convolved value). The highest RMSE mostly occurred in the blue, red, NIR reflectances, NDVI, and EVI in Hyperion dataset (Table 1-6).

For the purpose of deriving the universal inter-sensor translation equations, the combined transforms were suggested to be used in this study (Table 1-7). RMSE between the transformed and the convolved sensor value was calculated to describe how well

Table 1-6 Inter-sensor translation equations for three hyperspectral platform levels at the TOC level

			MODIS				
			Blue	Red	NIR	NDVI	EVI
ASD-MQUALs	AVHRR	Slope		0.8856	0.9275	0.9211	
		Intercept		0.0118	0.0073	-0.0078	
		R-square		0.9748	0.9965	0.9958	
		RMSE**		0.0033	0.0034	0.0143	
	SPOT-VGT	Slope	0.956	1.0064	0.9734	0.9327	0.9254
		Intercept	0.0002	0.005	-0.0018	-0.0112	-0.0104
		R-square	0.9998	0.993	0.9996	0.9979	0.9991
		RMSE**	0.0050	0.0019	0.0012	0.0110	0.0036
	VIIRS	Slope	1.1505	0.9655	1.0056	0.9991	0.9848
		Intercept	-0.0017	0.0116	0.001	0.0044	0.0099
		R-square	0.9944	0.9997	1	0.9992	0.9993
		RMSE**	0.0082	0.0100	0.0004	0.0039	0.0033
Hyperion	AVHRR	Slope		0.8843	0.8981	0.8738	
		Intercept		0.0056	-0.00003	0.0451	
		R-square		0.993	0.9924	0.9913	
		RMSE**		0.0047	0.0088	0.0272	
	SPOT-VGT	Slope	0.997	1.0214	0.9597	0.9224	0.967
		Intercept	0.0042	0.0005	-0.0023	0.0222	-0.0074
		R-square	0.9979	0.9991	0.9992	0.9904	0.9982
		RMSE**	0.0011	0.0019	0.0030	0.0302	0.0086
	VIIRS	Slope	1.199	0.9893	1.0007	1.0048	0.9508
		Intercept	-0.0099	0.0008	0.0002	-0.0046	0.0071
		R-square	0.9912	0.9999	0.9999	0.9993	0.9986
		RMSE**	0.0027	0.0017	0.0012	0.0090	0.0074
AVIRIS	AVHRR	Slope		0.918	0.879	0.8972	
		Intercept		0.008	0.021	0.0306	
		R-square		0.9994	0.9838	0.9995	
		RMSE**		0.0015	0.0061	0.0059	
	SPOT-VGT	Slope	0.983	1.0001	0.9783	0.9912	0.9626
		Intercept	-0.0009	0.0026	-0.0005	-0.0169	-0.0082
		R-square	0.9997	0.9999	0.9994	0.9998	0.9999
		RMSE**	0.0005	0.0007	0.0013	0.0041	0.0014
	VIIRS	Slope	1.0876	0.9897	0.9946	0.9962	1.0092
		Intercept	0.0019	0.0004	0.0004	0.0023	0.0027
		R-square	0.9994	0.9999	1	0.9999	0.9998
		RMSE**	0.0007	0.0005	0.0004	0.0031	0.0023

**root mean square error (RMSE) between the transformed sensor value and the convolved sensor value

Table 1-7 Inter sensor translation equations for reflectances and VIs with the combined sensors

From (x)	To (y)		Blue	Red	NIR	NDVI	EVI
MODIS	AVHRR	Slope		0.9051	0.895	0.8874	
		Intercept		0.0072	0.0088	0.0324	
		R-square		0.9933	0.9822	0.9932	
		Stdev*		0.0047	0.0107	0.0235	
		RMSE**		0.0047	0.0107	0.0235	
MODIS	SPOT-VGT	Slope	0.9843	1.0088	0.9635	0.947	0.9638
		Intercept	0.0018	0.002	-0.0004	0.0024	-0.0093
		R-square	0.9858	0.9989	0.9982	0.9928	0.9981
		Stdev*	0.0029	0.0021	0.0036	0.0258	0.0081
		RMSE**	0.0029	0.0021	0.0036	0.0262	0.0080
MODIS	VIIRS	Slope	1.1494	0.9884	0.9985	1.0009	0.9683
		Intercept	-0.0044	0.0007	0.0005	-0.0006	0.0074
		R-square	0.9775	0.9999	0.9998	0.9994	0.9975
		Stdev*	0.0042	0.0006	0.0013	0.0077	0.0092
		RMSE**	0.0042	0.0015	0.0013	0.0077	0.0092
AVHRR	SPOT-VGT	Slope		1.1089	1.0618	1.0645	
		Intercept		-0.0056	-0.0069	-0.0309	
		R-square		0.9954	0.9887	0.9945	
AVHRR	VIIRS	Slope		1.0848	1.0955	1.1197	
		Intercept		-0.0066	-0.0052	-0.0335	
		R-square		0.9933	0.9813	0.9917	
VIIRS	SPOT-VGT	Slope	0.8254	1.0205	0.9645	0.9442	0.9916
		Intercept	0.0067	0.0013	-0.0009	0.0039	-0.0157
		R-square	0.937	0.9988	0.9976	0.9894	0.9932

*standard deviation (stdev) from the difference between the transformed sensor value and the convolved sensor value

**root mean square error (RMSE) from the transformed sensor value and the convolved sensor value

inter-sensor translation equations replicate sensor reflectances and vegetation indices from the convolved multiple sensor values. The largest RMSE values were 0.0042 for VIIRS blue reflectance, 0.0047 for AVHRR red reflectance, 0.0107 for AVHRR NIR reflectance, 0.0262 for SPOT-VGT NDVI, and 0.0092 for VIIRS EVI.

There were former studies on inter-sensor transforms for NDVI (van Leeuwen et al. 2006 and Steven et al. 2003) as follows:

$$NDVI_{AVHRR-14} = 0.904NDVI_{MODIS} + 0.003 \quad \text{and} \quad NDVI_{SPOT-VGT} = 0.981NDVI_{MODIS} - 0.006$$

for Steven's equation (2003) [9]

$$NDVI_{AVHRR-14} = 0.9318NDVI_{MODIS} - 0.0071 \quad \text{and} \quad NDVI_{VIIRS} = 0.975NDVI_{MODIS} + 0.0022$$

for van Leeuwen's equation (2006) [10]

Equation [9] had the larger slope than the slope from the combined Hyperspectral translation equations. Equation [10] by various land covers at the surface level (surface reflectance) had a larger slope derived from AVHRR and MODIS and a smaller slope derived from VIIRS and MODIS.

In Fig. 1-10, inter-sensor transforms are provided for the blue, red, NIR and VIs. Linear relationships between various sensors and MODIS sensor were established in the cross plots. These translation equations from the combined hyperspectral datasets removed the spatial and temporal variations in the transforms i.e. various land covers in Brazil and different ecosystems in Arizona.

There are two methods to derive vegetation index. For example, if we had 0.1 of red and 0.4 of NIR at MODIS, the computed MODIS NDVI should be 0.6. When we converted MODIS red and NIR reflectances to AVHRR values using the translation

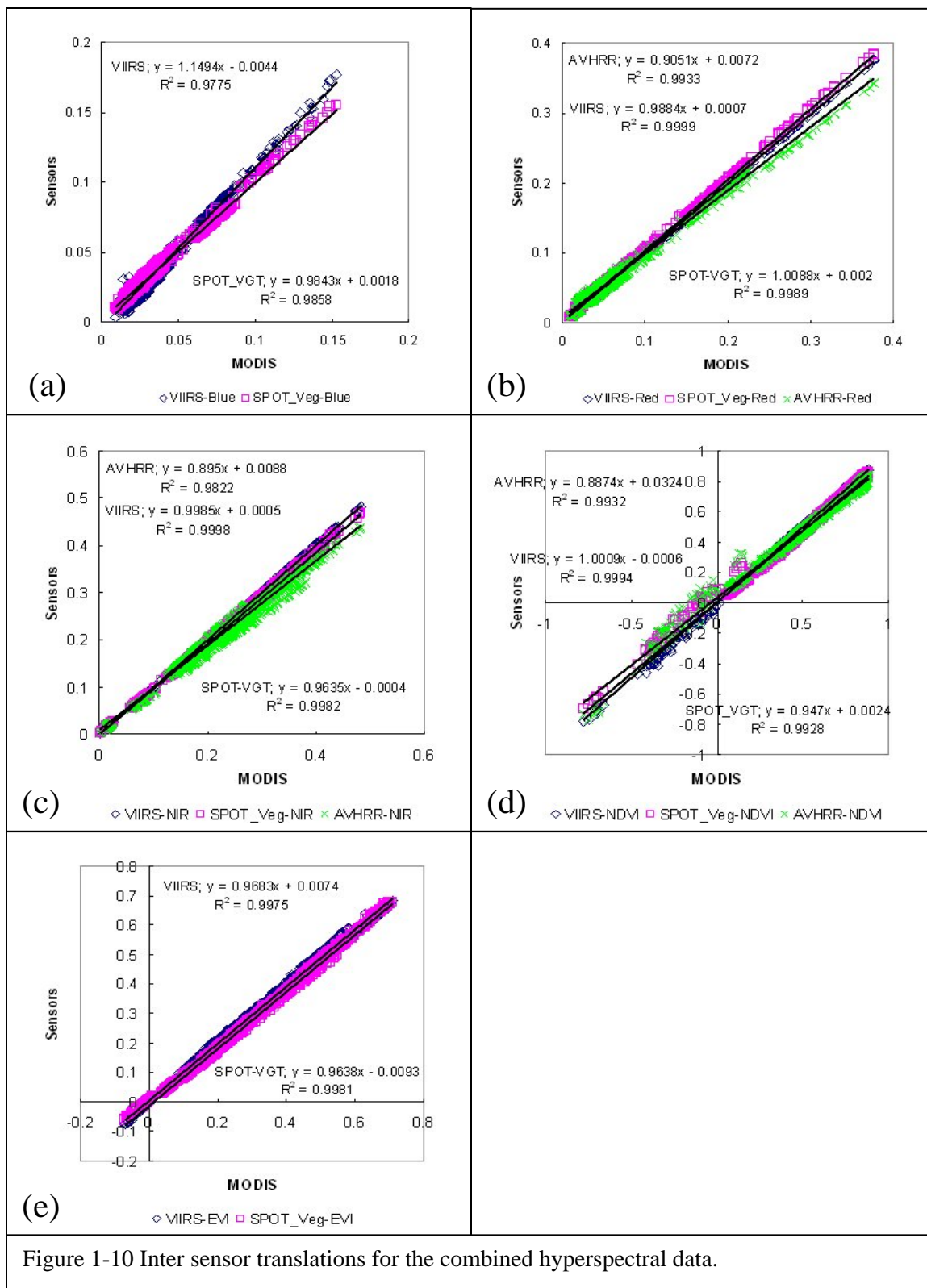
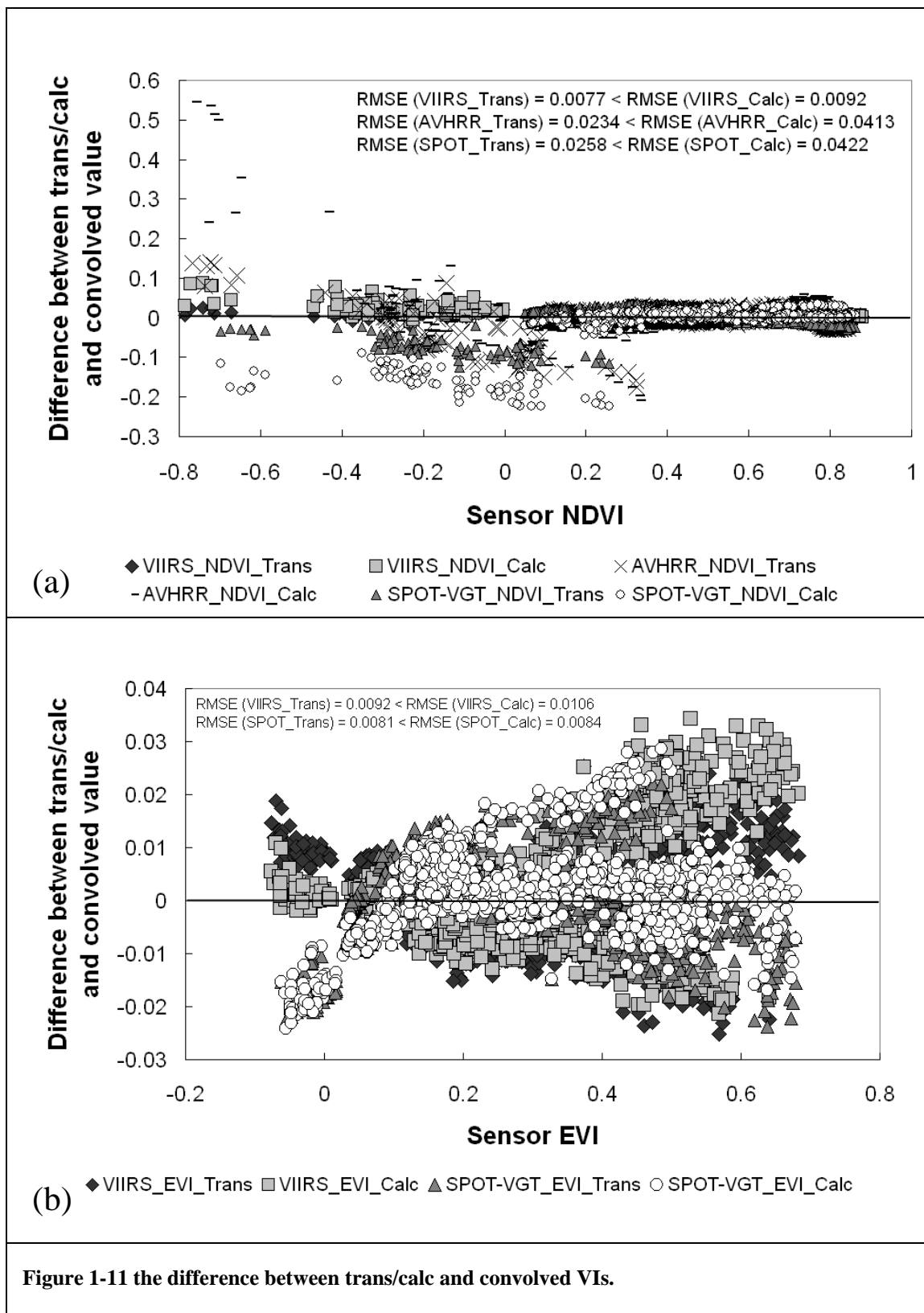


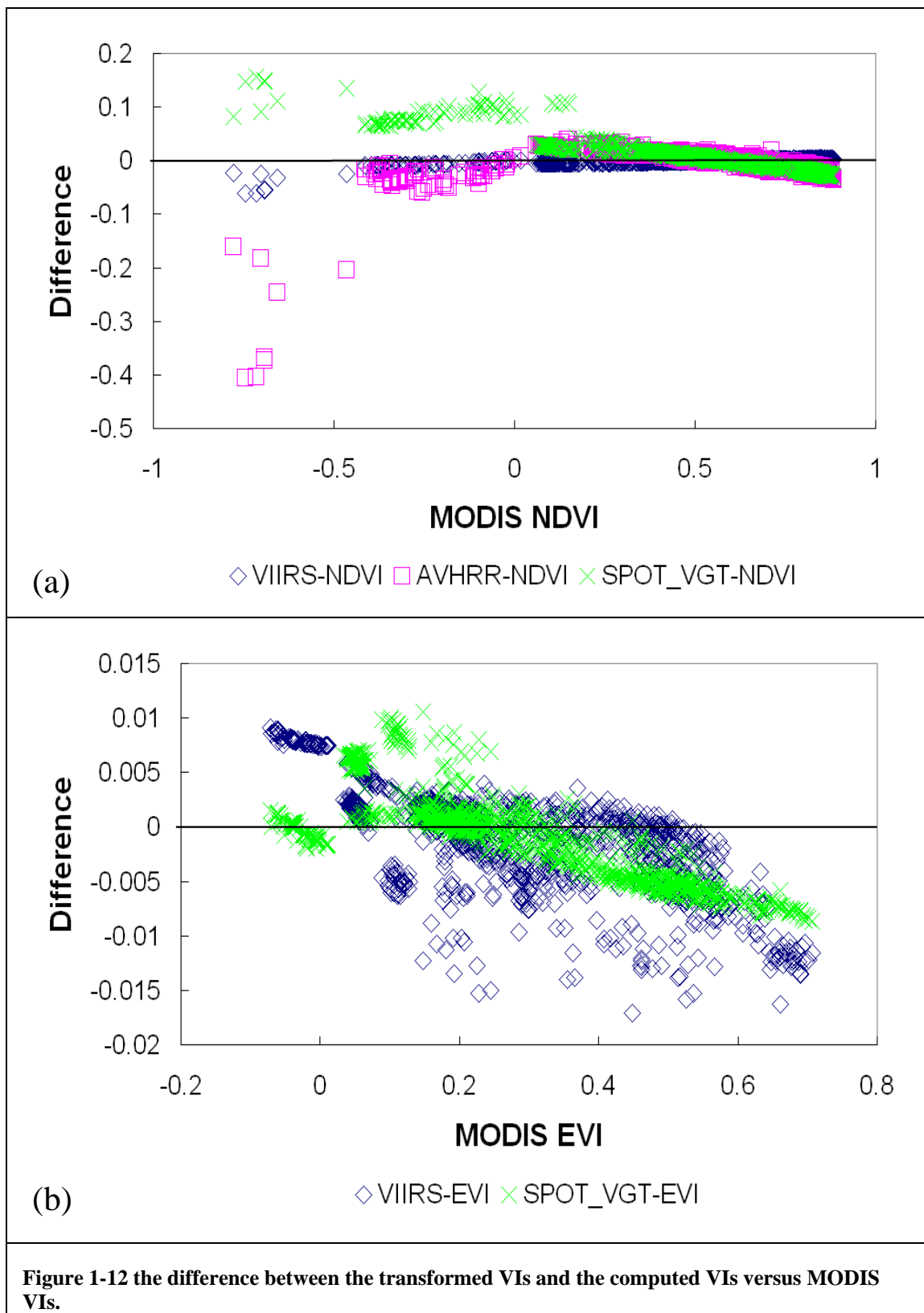
Figure 1-10 Inter sensor translations for the combined hyperspectral data.

equations between AVHRR and MODIS, the converted AVHRR red was 0.09771 and NIR was 0.3668. The calculated AVHRR NDVI from these converted reflectances was 0.5793, while the converted AVHRR NDVI through NDVI translation equation between AVHRR and MODIS was 0.56484. These did not match exactly and the difference was around 1%. The converted AVHRR NDVI was smaller than the computed AVHRR NDVI. This matter was applicable to EVI. We should not overlook this situation on the vegetation indices transforms and vegetation indices computed from the transformed reflectances.

In order to investigate which vegetation indices are closer to the convolved vegetation indices, the differences between the translated/calculated and convolved vegetation indices were compared and RMSE per each sensor was computed in Fig. 1-11. RMSE from the translated NDVI and EVI was smaller than that from the calculated NDVI and EVI (Fig. 1-11a, b). Thus, the transformed vegetation indices were closer to vegetation indices from the convolved values than the computed vegetation indices. Concerning the biases between both vegetation indices, the difference between the transformed vegetation indices and the computed vegetation indices were presented in Fig. 1-12. The difference from NDVI was constant, excluding the negative NDVI value (Fig. 1-12a). As for the EVI, the difference in the VIIRS sensor ranged from 0.01 to -0.015, while that from the SPOT-VGT sensor varied from 0.01 to -0.01 (Fig. 1-12b).

To fully understand the behavior of vegetation indices to some types of external factors, a detailed analysis of the individual bands needs to be performed. The vegetation





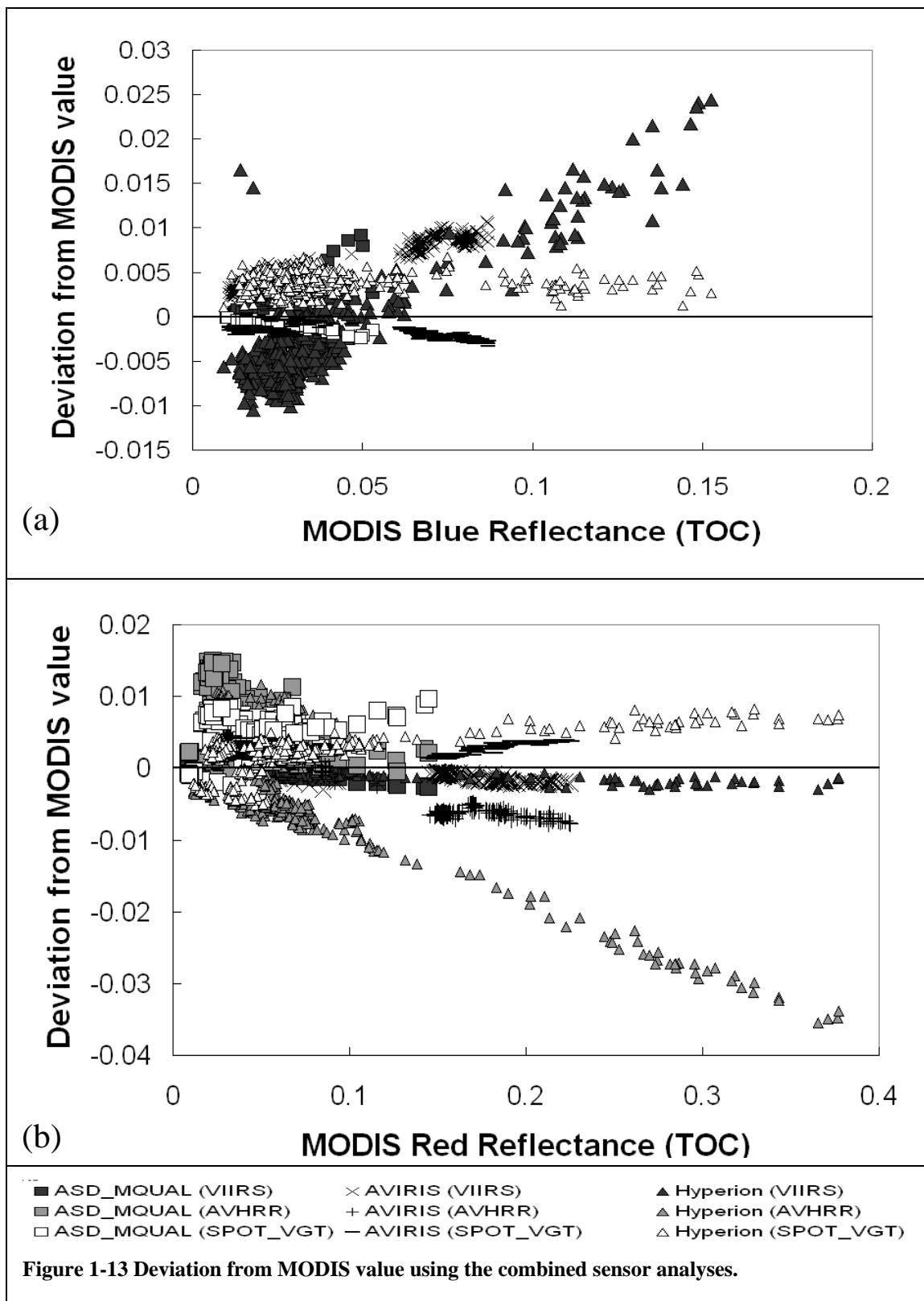
index value will need to be the weighted in the result of the sensitivity experienced by each band to the external influence, although the strength of NDVI reduces many forms of multiplicative noise (illumination differences, cloud shadows, atmospheric attenuation, and certain topographic variations) present in multiple bands. In this study, when one sensor vegetation index is transformed to another sensor vegetation index, the transformed vegetation index would be suggested rather than vegetation indices calculated from the transformed reflectances.

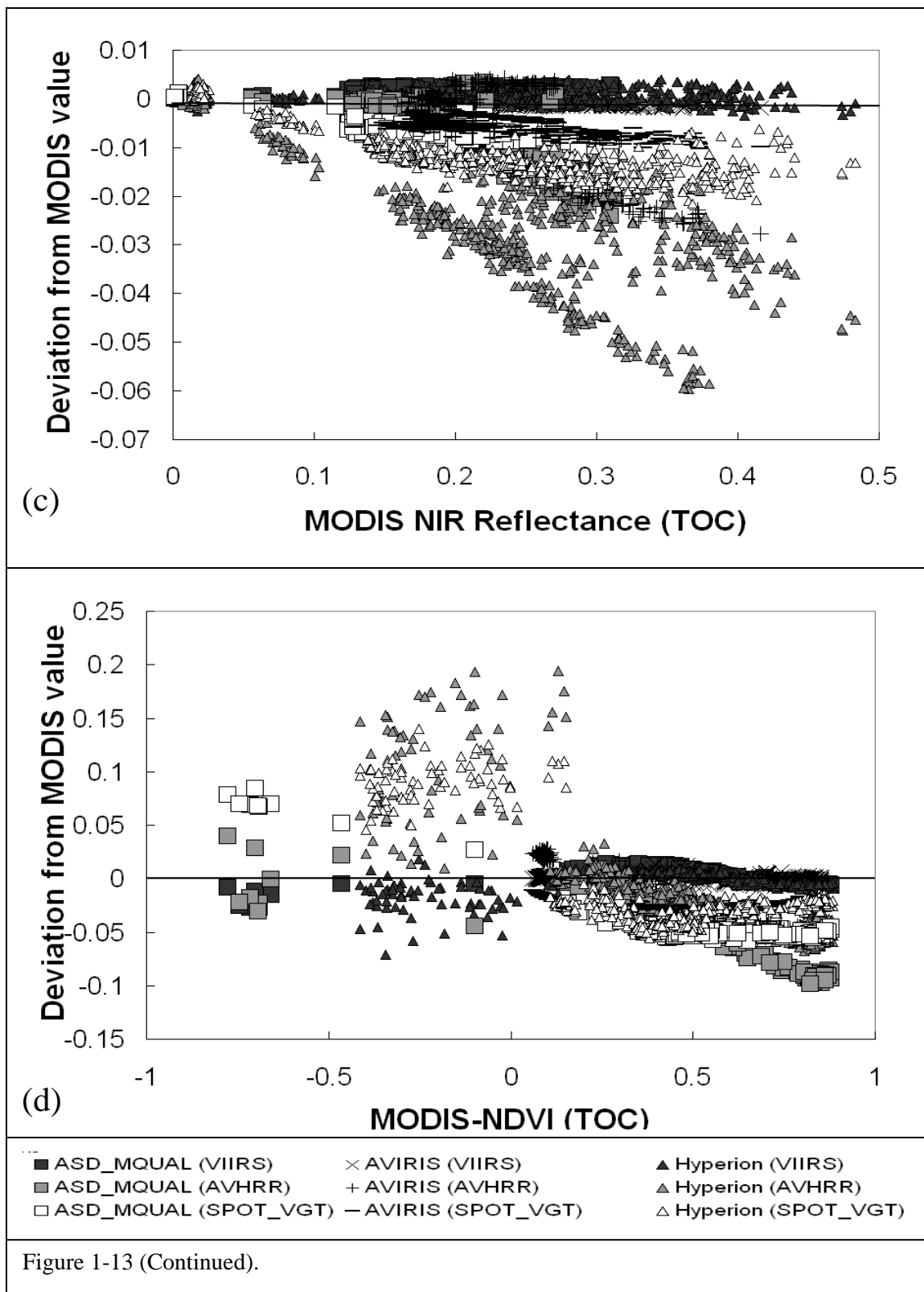
3.6 Sensor deviation analyses using the combined hyperspectral sensor.

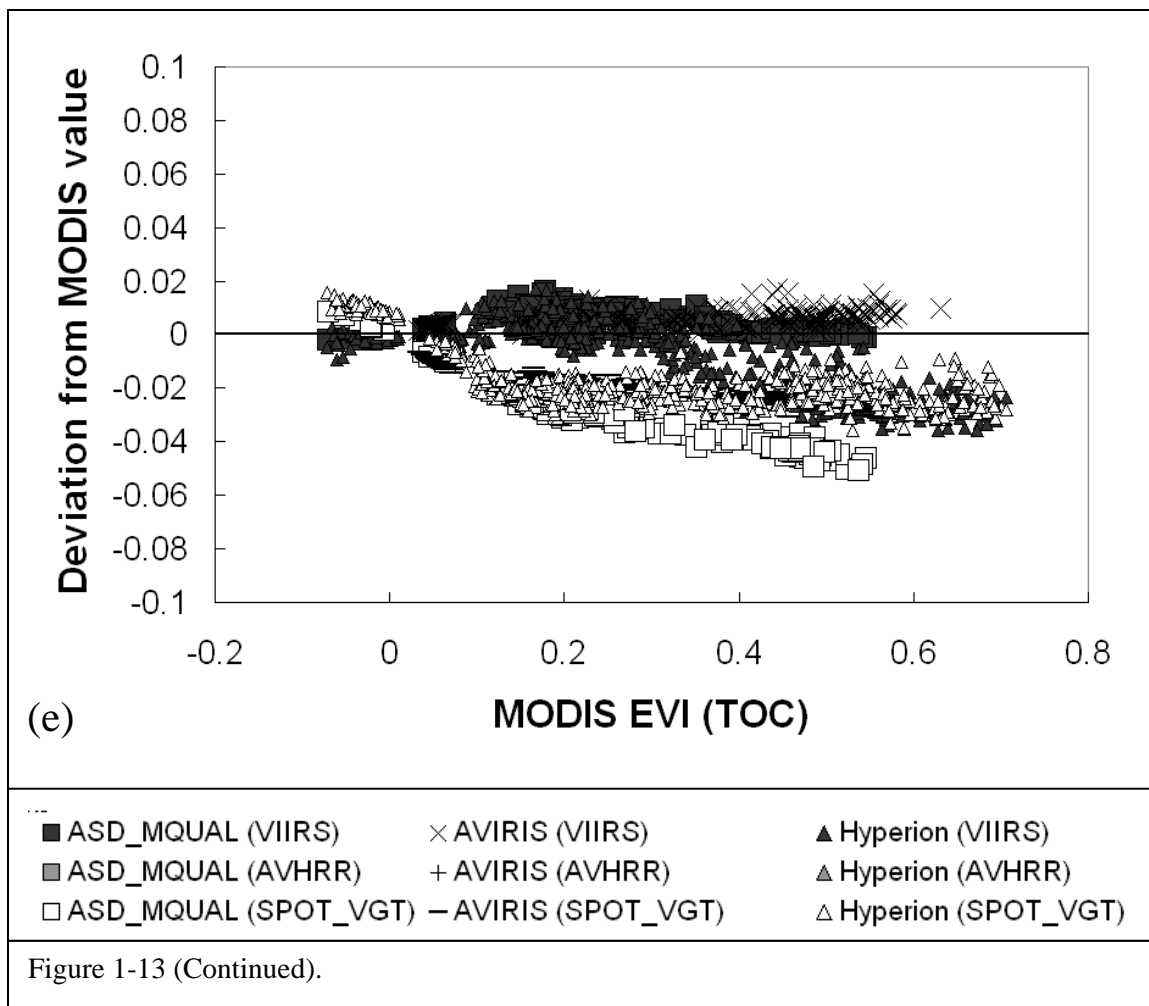
In these combined hyperspectral sensor analyses, three hyperspectral dataset (canopy-level, airborne-level, and satellite-level) were gathered in one cross plot. In Fig. 1-13, there were a couple of cross plots for the blue, red, NIR bands and vegetation indices. For the blue reflectance (Fig. 1-13a), ASD-MQUALs blue reflectance was distributed in the lower value of blue reflectance (MODIS blue reflectance of 0.010 to 0.053). AVIRIS blue reflectance ranged from 0.01 to 0.09 in the MODIS blue reflectance. Hyperion blue reflectance had the biggest range from between 0.01 and 0.15 in the MODIS blue reflectance due to darkness to bright land covers and the highest acquisition altitude. Seeing the deviation from the MODIS blue reflectance, Hyperion blue reflectance was seriously diverted from the zero value (-0.01 to 0.025). In contrast to Hyperion, ASD-MQUALs and AVIRIS blue reflectance was distributed along the zero value. Mostly, the VIIRS deviation in the blue band was positive and the SPOT-VGT blue deviation was negative within a very narrow scope of deviation values. Hyperion red reflectance had

still the widest range compared to the other two levels (ASD-MQUALs and AVIRIS levels) (Fig. 1-13b). The AVHRR red reflectance exhibited the second largest distribution from 0.02 to 0.22 in MODIS red reflectance. ASD-MQUALs red reflectance ranged from zero to 0.14 in the MODIS red reflectance. Hyperion red reflectance deviations from Hyperion MODIS red reflectance was between -0.04 and 0.012 with regard to Hyperion MODIS red reflectance of 0.012 to 0.377 . For ASD-MQUALs and AVIRIS deviations from MODIS red reflectance, the dispersion was consistently close to the zero value. In the case of the NIR reflectance (Fig. 1-13c), the range of Hyperion NIR reflectance was not significantly larger than that of the blue and red bands. Hyperion, AVIRIS, and ASD-MQUALs NIR reflectance were distributed between 0.012 and 0.48 , 0.13 and 0.42 , and 0.12 and 0.31 in the MODIS NIR reflectance, respectively. But, NIR reflectance deviations in AVIRIS and ASD-MQUALs had still a slight variation and went to the negative value with the MODIS NIR reflectance. In terms of NDVI (Fig. 1-13d), the positive NDVI values were nearly linear, which they exhibited some regression except for some of the Hyperion NDVI (~ 0.15 in MODIS NDVI). Negative NDVI values were distributed in water areas and showed extreme fluctuation from the 1:1 line. As MODIS NDVI increased, AVHRR and SPOT-VGT had two different ways from MODIS NDVI of 0.6 and they were found at diverse land covers. Concerning the EVI (Fig. 1-13e), the negative EVI value did not exist compared to the negative NDVI value. Most of the linear distribution was well established. SPOT-VGT EVI deviated from the zero level, while VIIRS EVI was constant until MODIS EVI of 0.35 . Both deviations went in two directions due to the different platforms (AVIRIS and Hyperion).

The hyperspectral simulation with various sensor bandpasses in the combined sensors provided the red and NIR bands between MODIS and VIIRS was highly correlated, those between MODIS and SPOT-VGT were well correlated, but those between MODIS and AVHRR had poor correlation. As for the blue reflectance, there were apparent discrepancies between the MODIS and VIIRS sensors, which resulted in less-compatible and biased VIIRS-EVI values. The VIIRS blue reflectance did not match the MODIS blue reflectance and was close to the green spectral region causing the higher blue reflectances and the lower EVI values compared to MODIS. In the case of SPOT-VGT, as EVI was increased, the deviation from MODIS EVI was also increased up to 0.05, which resulted from a broader NIR spectral bandpass of SPOT-VGT. The NIR bandpass also shifted to the shorter wavelength (red spectral band) relative to the MODIS NIR spectral bands. For the vegetated area, the SPOT-VGT NIR band included a small part of red-edge, which resulted in the lower NIR reflectance of SPOT-VGT.







4. Discussion and conclusions

We studied the inter-sensor translations with respect to different hyperspectral platforms (ASD-MQUALs, Hyperion, and AVIRIS). To build inter-sensor transforms, three different datasets (ASD-MQUALs, Hyperion, and AVIRIS) were utilized through spectral convolution to multispectral data (MODIS, VIIRS, AVHRR, and SPOT-VGT).

The sensor deviation values from the MODIS reflectances and vegetation indices were shown to evaluate the continuity to MODIS. The Hyperion dataset represented the largest variations due to atmospheric contamination, even with the atmospheric correction. The VIIRS reflectances and VIs values were almost identical to the MODIS values except for the blue reflectance. It also showed the effect of blue band on EVI due to the constant offsets from the MODIS EVI value.

Table 1-6 showed the summary of the slope, intercept, R^2 and RMSE of inter-sensor translation equations at the TOC levels. In ASD-MQUALs, the lowest R^2 (0.9748) occurred in the AVHRR vs. MODIS red reflectances and the largest R^2 (1) occurred in the VIIRS vs. MODIS NIR reflectances among three datasets, respectively (Table 1-4). In reference to the Hyperion dataset, the lowest R^2 (0.9904) occurred in the SPOT-VGT vs. MODIS NDVI and the largest R^2 (0.9999) occurred in the VIIRS vs. MODIS Red and NIR reflectances among three datasets, respectively. As for the AVIRIS dataset, the lowest R^2 (0.9838) occurred in the AVHRR vs. MODIS NIR reflectances and the largest R^2 (1) occurred in the VIIRS vs. MODIS NIR reflectances among three datasets, respectively. RMSE between the transformed and the convolved sensor value implied that inter-sensor translation equations derived from Hyperion datasets, in particular

SPOT-VGT and AVHRR, were mostly more different between the transformed and convolved reflectances and vegetation indices than ASD-MQUALs and AVIRIS.

To eliminate spatial and temporal differences in the transforms and convert it to universal transforms, the inter-sensor translation equations were developed from the combined sensor dataset (Table 1-7). Table 1-7 summarized the slope, intercept, R^2 and RMSE of the inter-sensor translation equations with the combined hyperspectral data. If the reflectances or vegetation indices with respect to one optional sensor were given, then the reflectances and vegetation indices can be converted to another sensor using these transforms. For the most part the three datasets through a linear coefficient of R^2 were in consistent agreement among the sensors over the various types of land covers. As expected, the relationship between the SPOT-VGT and VIIRS blue bands was the poorest ($R^2 = 0.937$) and the relationship between the MODIS and VIIRS red bands was the best ($R^2 = 0.9999$). The reflectances and vegetation indices in SPOT-VGT and VIIRS were increased to 11% of the AVHRR values and 14% of the AVHRR values, respectively. The MODIS and VIIRS sensors had similar reflectances and vegetation indices except for the blue band and EVI. The bias between MODIS and VIIRS sensor was able to be increased up to 15% (blue band). Statistical method presented the consistencies between the transforms at each datasets. They did not have many differences between the inter-sensor translations from each datasets (Table 1-4).

For deriving the vegetation indices, the vegetation indices using the inter-sensor translation equations were suggested instead of the computed vegetation indices using the transformed reflectances derived from inter-sensor translation equations.

The long-term data record could extend back to 1981 in order to utilize the AVHRR record. The inter-sensor translation equations are provided in Table 1-7. Conversely, any reprocessing of the AVHRR or MODIS records should consider steps to allow forward compatibility and continuity with newer sensors and products (VIIRS).

Atmospheric status, atmospheric correction scheme, overpass time and sun/view angle, and topographical effects still remained problematic. So it should be considered. The relationship between actual data from real satellites and these simulated data should be further studied for solutions to these problems.

III. Compatibility of enhanced vegetation index across sensors: An evaluation with convolved Hyperion data

1. Introduction

A variety of satellite sensors routinely observe the Earth's surface at daily, weekly, and monthly time periods. Monitoring the Earth's biosphere is very important for examining land cover change, agricultural production, natural resource management and climate change. The NOAA Advanced Very High Resolution Radiometer (AVHRR) has produced consistent normalized difference vegetation index (NDVI) products for over 20 years (Tucker 1979). The AVHRR NDVI enables temporal and spatial variations in vegetation photosynthetic activity and biophysical properties to be assessed, through its relationship to biomass, leaf area index, agriculture and rangeland primary productivity, absorbed photosynthetic radiation, carbon dioxide, meteorological parameters, and ecological parameters (Coops et al. 2007, Heinsch et al. 2006, Running et al. 2004, Gao et al. 2000, Schloss et al. 1999, Field et al 1995, Sellers et al. 1985, Asrar et al. 1984, and Tucker 1979).

On a standpoint of global monitoring, in addition to AVHRR, Moderate Resolution Imaging Spectroradiometer (MODIS) onboard Terra and Aqua satellite platforms are viewing the entire Earth every 1 to 2 days in 36 spectral bands with 250 m to 1 km spatial resolution for various purposes (atmosphere, land, ocean, and ice). The VEGETATION instrument of the System Pour l'Observation de la Terre (SPOT 4) program was launched on March 1998. SPOT 4 provides imagery with ~ 1 km pixel resolution in 4 bands every day. The Sea-viewing Wide Field-of-view Sensor (SeaWiFS) was launched on August

1997. The SeaWiFS has 8 bands from Visible/NIR bands with 1.1 km spatial resolution with 1 day revisit time. The Visible/Infrared Imager/Radiometer Suite (VIIRS) will collect imagery and radiometric data with 0.4 to 0.8 km spatial resolution in 22 bands with 1 day temporal resolution. VIIRS will reside on a platform of the NPOESS series of satellites.

In order to use the NDVI for quantitative assessments, it is advantageous to reduce the many sources of noise related to view angle differences, cloud shadow, atmospheric attenuation, and topographic effects, though using only red and NIR bands. The main disadvantage of the NDVI is the inherent nonlinearity of ratio-based indices and NDVI saturation problems under high biomass conditions. To overcome this weakness, the Enhanced Vegetation Index (EVI; Huete et al. 1997) was developed to optimize the vegetation signal with improved sensitivity in high biomass regions and reduce atmospheric influences and canopy background noise. As one of the 16-day MODIS vegetation index products (MOD13), EVI has been used to extract biophysical information (e.g., gross primary productivity and phenology information) (Coops et al. 2007, Huete et al. 2006a, Heinsch et al. 2006, Running et al. 2004, Schloss et al. 1999, and Field et al 1995).

There are many studies that show the compatibility of merging coarse resolution NDVI values from new and advanced sensor systems for the purpose of the extending the existing long-term NDVI time series data (Miura et al. 2006, van Leeuwen et al. 2006, Brown et al. 2006, Fensholt et al. 2006, Tucker et al. 2005, Gallo et al. 2005 and 2004, Steven et al. 2003, Bryant et al. 2003, and Gitelson et al. 1988). Many cross-sensor

translation equations were developed and compared from simulated and/or real remote sensing dataset (van Leeuwen et al. 2006, Miura et al. 2006, Steven et al. 2003, and Gitelson et al. 1998). Former translation equations above were dependent on land cover types, sensor spectral characteristics, and atmospheric condition. Sensor continuity issues were conducted from inter-comparison of various multi-sensor datasets with the relationship between NDVI and biophysical variables (Goetz 1997). Composited NDVI images were fairly robust and the NDVI anomalies exhibited similar variances between sensors on the historic AVHRR NDVI record for vegetation phenological study (Brown et al. 2006).

In contrast, the continuity and compatibility of the EVI across different sensor systems has received much less attention, compared with the NDVI, for continuity studies, despite the potential complementary benefits of the EVI to the existing NDVI time series, such as in more densely vegetated forest canopies. Fensholt et al. (2004) analyzed NDVI and EVI continuity using MODIS and AVHRR datasets and found the dynamic range of MODIS NDVI and EVI was generally much larger than for the AVHRR NDVI, and the EVI demonstrated improved sensitivity for high biomass. Xiao et al. (2005 and 2004) found MODIS and SPOT-VGT derived EVI to yield similar and consistent phenology profiles in three different forests in North and South America. One important reason for the lack of EVI continuity studies is that the EVI can only be applied to sensors with a blue band, and most studies have focused on MODIS and AVHRR translation, in which there is no AVHRR blue band available for EVI computation. In addition, the EVI may be more complex for continuity purposes due to the combined use

of three bands, compared with the two bands in the NDVI. Thus, EVI values may be more difficult to translate across sensors, since 3-band equation, such as EVI, may require strict coherencies among three bands, rather than two. Recent studies suggest the blue band in EVI may add uncertainties and complicate translation across sensors. Since the EVI is currently a standard EDR product in the future NPOESS-VIIRS sensors, it is of great interest to characterize the compatibilities of the MODIS and VIIRS EVI and their associated blue, red, and NIR bands. Jiang et al. (submitted, 2007) have shown a 2-band EVI (EVI2), without a blue band, is identical with EVI under good observation conditions, i.e., with good quality data. MODIS EVI2 equation was derived from the linear vegetation index (LVI: Jiang et al. 2007) with optimized coefficients of MODIS EVI2, minimizing the mean absolute difference (MAD) between MODIS EVI and EVI2 using a global dataset. The similarity between MODIS EVI and EVI2 was validated at local, continental, and global scales.

In this paper we investigate the potential cross-sensor compatibilities and problems of the EVI and EVI2, from MODIS, VIIRS, SPOT-VGT, SeaWiFS, and AVHRR sensors using three convolved EO-1 Hyperion images (the signal to noise: ~ 40) representing a wide range of land cover types, including grassland, savanna, wetland, riparian, and rainforest land surface cover types. We also evaluated the use and extension of the EVI2 within as well as across sensor systems. The EVI and EVI2 have the forms,

$$EVI \text{ or } 2\text{-BandEVI} = G \times \frac{\rho_{NIR} - \rho_{Red}}{L + \rho_{NIR} + C_1 \times \rho_{Red} - C_2 \times \rho_{Blue}} \quad [1]$$

Where ρ is atmospherically corrected surface reflectances, L is the canopy background adjustment and C_1 , C_2 are the coefficients of the aerosol resistance term for aerosol influences in the red and blue bands. The coefficients are, $L=1$, $C_1=6$, $C_2 = 7.5$, and G (gain factor) = 2.5 (Huete, 1997). For EVI2, its coefficients are $L=1$, $C_1=2.4$, $C_2=0$, and $G = 2.5$ (Jiang et al., 2007, submitted).

The objectives of this study were

- (1) spectral bands (blue, red, and NIR bands), EVI and EVI2 translations and coherency analyses for multiple sensors,
- (2) sensitivity analysis of EVI and EVI2 on blue, red, and NIR reflectance translation over multiple sensors,
- (3) the effect of land cover type on EVI, EVI2 translation and red-blue coherency,
- (4) evaluation of cross-sensor compatibilities of MODIS and VIIRS EVI and EVI2, as well as MODIS and AVHRR EVI2.

2. Study Site and Methodology

Three Earth Observing (EO-1) Hyperion scenes that covered a gradient in biomes, land cover types, and land conversion in Brazil were used in this study, including the Tapajos Forest evergreen broadleaf rainforest (Tp, July 30, 2001); the cerrado/ savannah biome in Brasilia National Park (BNP, July 20, 2001); and Araguaia National Park (ANP, July 18, 2001) transition biome with rainforest, wetlands, and cerrado vegetation (Table 2-1). All three sites are primary core validation sites for the Large Scale Biosphere and

Table 2-1 Description of the study areas.

Site location	Mean Annual Precip.	Mean Annual Temp.	Major Land cover type	Mean Elevation	Solar Zenith Angle
Tapajos National Forest, Brazil	2060 mm	26 °C	Primary Forest Cultivated Pasture	100 m	38.1 °
Araguaia National Park, Brazil	1670 mm	26 °C	Riparian Forest Primary Forest Savanna Woodland Savanna Grassland Cultivated Pastures Burned Cerrado	210 m	44.8 °
Brasilia National Park, Brazil	1260 mm	21 °C	Riparian Forest Cerrado Woodland Cerrado Grassland	900 m	49.2 °

Atmosphere in Amazon Experiment (LBA) equipment. The EO-1 Hyperion hyperspectral imager is a pushbroom sensor providing 220, 10 nm bands covering the spectrum from 400 to 2500 nm.

The Hyperion hyperspectral data were radiometrically calibrated to apparent spectral radiances at the top of atmosphere (TOA) using radiometric calibration coefficients (gain and offset):

$$L_{i,j,k} = DN_{i,j,k} \times [CalCoef_k]^{-1} \quad [2]$$

where $i, j, k =$ image pixel i, j in spectral band k

$L_{i,j,k} =$ in-band radiance at sensor aperture ($\mu W / cm^2 nm sr$)

$CalCoef_k =$ in-Band radiance calibration coefficient ($\mu W / cm^2 nm sr / DN$)

$DN_{i,j,k} =$ image product digital value (DN)

The top of atmosphere (TOA) and nadir-view Hyperion data was convolved spectrally into several sensor bandpasses using their spectral response functions, including MODIS, NOAA-14 AVHRR, NPOESS VIIRS, SPOT-VGT, and SeaWiFS

(Fig. 1-1). The spectral response functions were splined to Hyperion band center wavelengths for each pixel, and the convolved bandpasses were atmospherically corrected to top of canopy (TOC) spectral reflectances with 6S (Vermote et al. 1997). The 6S model corrections were constrained with site specific atmospheric parameter values retrieved from available data sources (MODIS products and GTOPO30). Total ozone thicknesses and column water vapor contents were extracted from the MODIS daily atmosphere product (MOD08) for three study sites (King et al., 2003). The Tropical atmosphere model was used for the Tapajos and Araguaia scenes and the Midlatitude Winter atmosphere model was used for the Brasilia scene. The continental aerosol model with a 100 km visibility (0.1 optical thickness) was used in all three scenes, as they were all acquired under very clear sky conditions (Miura et al. 2006). GTOPO30 (Gesch, 1994) was used for local ground elevation retrievals for three study sites.

VI agreements across sensor bandpasses and VI's were evaluated with regression analysis, and cross-sensor differences relative to MODIS were evaluated by subtraction of sensor values (reflectances and VI's) from the corresponding values from MODIS. The mean absolute difference (MAD) between variables from the two sensors was also computed as an overall quantitative measure of sensor differences;

$$MAD = \frac{\sum_{i=1}^n |X1_i - X2_i|}{n} \quad [3]$$

where X1 = reflectances and VIs of sensor X1 and X2 = MODIS reflectances and VIs.

In this analyses, differences associated with sun/view angles, atmosphere effects, pixel size and geometric location/ registration were minimal, since the convolved datasets were acquired for identical view, sun angle, and atmospheric correction conditions (view zenith angle: 0-5°) using the same pixels at different bandpasses. There may be minor atmosphere effects across the 3 scenes used, however, all 3 scenes were clear, cloudless, and with very thin atmospheres. Similarly, there were minor cross-scene differences in sun angles (solar zenith angles: 38-49°), which are equivalent to what would be acquired from polar orbiting satellite (EO-1 flies in formation with the Terra platform). Thus, in this study, we assume all data are good quality observations, with negligible noise and contamination bias. Therefore, differences in the convolved datasets would mainly arise from sensor spectral bandpass differences and their signal responses to differences in land cover type, phenology, and soil background.

3. Results

3.1 Compatibility of spectral bands across sensors

Comparisons of blue, red, and NIR bands with MODIS equivalent bands showed strong and linear cross-sensor relationships for each of the individual top-of-canopy (TOC) reflectance bands (Table 2-2). However, in many cases, there were significant differences in the slopes and intercepts of the regression relationship between two sensors. Relationships that deviate from the 1:1 line will result in significant differences in cross-sensor values, despite their strong correlation. Table 2-2 summarizes the

translation equations between sensor and MODIS, including slope, intercept, R^2 , and MAD (RMSE) across sensors.

Table 2-2 Cross sensor translation equations with MODIS using linear regression lines.

		MODIS (x)						(EVI2 vs. EVI)*
		Blue	Red	NIR	NDVI	EVI	EVI2	
VIIRS	Slope	1.1845	0.9806	0.9994	0.9786	0.9382	0.9866	0.9627
	Intercept	-0.0095	0.0013	0.0006	0.0125	0.0124	0.0044	0.0197
	R-square	0.9784	0.9997	0.9998	0.9998	0.9984	0.9998	0.9967
	MAD (RMSE)	0.0040	0.0010	0.0007	0.005	0.0120	0.0020	0.0108 (0.0178)
SPOT-VGT	Slope	1.0047	1.0104	0.9650	1.0278	0.9894	0.9730	0.9029
	Intercept	0.0039	0.0016	-0.0046	-0.0468	-0.0169	-0.0165	0.0242
	R-square	0.9937	0.9989	0.9994	0.9988	0.9991	0.9992	0.9944
	MAD (RMSE)	0.0040	0.0020	0.0130	0.030	0.0200	0.0250	0.0237 (0.0341)
SeaWiFS	Slope	1.2032	1.0399	0.9880	1.0520	0.9722	1.0200	0.9547
	Intercept	-0.0129	-0.004	0.0010	-0.0231	0.0005	-0.0045	0.0234
	R-square	0.9782	0.9956	0.9997	0.9984	0.9979	0.9994	0.9968
	MAD (RMSE)	0.0060	0.0030	0.0020	0.014	0.0010	0.0050	0.0103 (0.0168)
AVHRR (MODIS*)	Slope		0.8462	0.9024	0.9220		0.8745	0.9136
	Intercept		0.0084	-0.0017	0.0130		0.0011	0.0278
	R-square		0.9710	0.9844	0.9964		0.9969	0.9945
	MAD (RMSE)		0.0050	0.0250	0.036		0.040	0.0193 (0.0179)

The relationship is y (sensor or EVI2) = $a \cdot x$ (MODIS or EVI) + b , * EVI2 vs. EVI relationship for each sensor.

RMSE is derived from the convolved EVI2 and the converted EVI2 using translation equation between EVI and EVI2.

MODIS blue reflectances were most strongly correlated with SPOT-VGT blue reflectances ($R^2=0.994$) with a slope very close to one (1.005), as expected from their similar spectral response functions (Fig. 1-1). The VIIRS and SeaWiFS blue reflectances were least, although strong, correlated with MODIS blue reflectances ($R^2=0.978$), but with slopes that deviated the most from the 1:1 line (slopes of ~ 1.2). Overall, SeaWiFS

blue reflectances were mostly below the 1:1 line, while SPOT-VGT blue reflectances were higher, or above the 1:1 line.

Sensor bandpass relationships with MODIS in the red were more highly correlated and with slopes much closer to one and intercepts near zero (Table 2-2). Most linear coefficient of determination values exceeded $R^2 > 0.996$, with slopes between 0.98 and 1.04, with the exception of weaker AVHRR red reflectance relationships, $R^2 = 0.971$, and a slope of 0.846. The bias between the AVHRR and MODIS red reflectances became increasingly negative with increasing MODIS red reflectances. The VIIRS and SeaWiFS red reflectances showed strong agreements with MODIS red reflectances despite some differences in their spectral response curves (Fig. 1-1).

The overall NIR relationships between MODIS and the other sensors were the most variable (see next section), although sensor-specific (VIIRS, SPOT-VGT, and SeaWiFS) relationships with MODIS were very strong with R^2 values exceeding 0.999, except in the case of AVHRR where the R^2 was 0.984. The slopes of the cross-sensor NIR relationships were also lowest for the AVHRR (slope of 0.9), resulting in a 10% negative bias attributed to the very wide AVHRR NIR bandpass (Fig. 1-1). Overall, NIR reflectances from MODIS were typically larger than the corresponding NIR reflectances from all other sensors and all regression slopes were less than one, and with near zero intercepts (Table 2-2).

3.3 Cross-sensor reflectance deviations

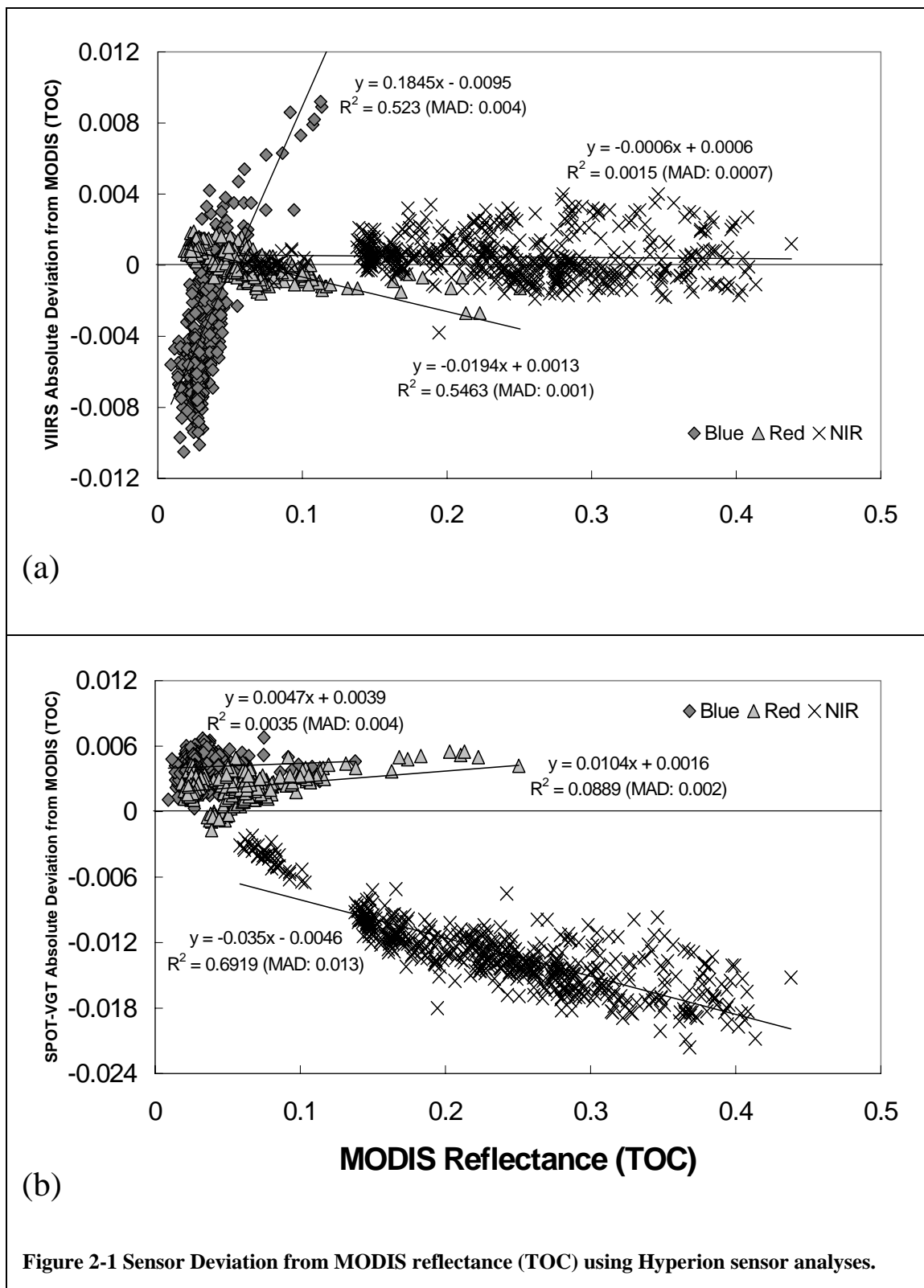
Sensor compatibilities and deviations between MODIS blue, red, and NIR reflectances with those from VIIRS, SPOT-VGT, and SeaWiFS were examined in terms of their absolute differences (Fig. 2-1). Ideally, the best compatibility is obtained when the cross-sensor differences are near zero across a large range of reflectance values, i.e., slopes close to zero and with intercepts near zero, i.e., zero bias. The absolute deviations of VIIRS and MODIS reflectances showed generally good agreements in the red and NIR bands, but strong and critical differences in the blue (Fig. 2-1a). VIIRS blue reflectance deviations were mostly negative and ranged from -0.01 to + 0.01 with a MAD of 0.004. The steep slope of the VIIRS-MODIS blue difference relationship indicated that over a very narrow range of MODIS blue reflectances (0.02-0.03), there was a large and much wider range of VIIRS blue reflectances for the same surface targets. In contrast, VIIRS red and NIR reflectance deviations from MODIS were much lower with a range of differences between -0.003 and +0.002, and MAD values near 0.001. The slopes of the cross-sensor red band differences were -0.02 for slope and +0.005 offset with NIR having a relatively constant slope (-0.0006) and an offset less than +0.004.

SPOT-VGT reflectance differences relative to MODIS were generally higher than between VIIRS and MODIS (Fig. 2-1b). SPOT-VGT blue reflectance deviations were mostly positive, in contrast to the mostly negative differences found with VIIRS, nevertheless the MAD in the blue was similar to that found with VIIRS (MAD~0.004) (Fig. 2-1b). SPOT-VGT red reflectance deviations were somewhat higher than found with VIIRS (MAD~0.002), and NIR deviations were particularly strong and increasingly

negative with higher NIR reflectances, resulting in approximately a 5% decrease relative to MODIS (Fig. 2-1b). The range of NIR differences varied from near zero to -0.02 with an overall MAD value of 0.013.

The reflectance deviations between SeaWiFS and MODIS appeared very similar to those shown between VIIRS and MODIS (Fig. 2-1c). Blue reflectance deviations were mostly negative, with a range between -0.013 to + 0.013, and had a larger MAD value (~0.006) than found with VIIRS. SeaWiFS red reflectance deviations (-0.007 – 0.005) were scattered close to the zero line, with a higher MAD value of ~0.003, while SeaWiFS NIR reflectance deviations were distributed similarly as with VIIRS, but with mostly negative bias, a slight slope, and low MAD value of 0.002 (Fig. 2-1c).

The AVHRR sensor showed the largest deviations from MODIS in both the red and NIR, with MAD values of 0.005 and 0.025, respectively. NIR differences were particularly pronounced and increasingly negatively biased with increasing NIR reflectances (Fig. 2-1d). For a given MODIS NIR reflectance of 0.30, the AVHRR equivalent NIR reflectance varied from less than 0.01 to as high as 0.05 (16% decrease). The AVHRR red reflectances were mostly biased positively, showed the highest overall red reflectance deviations from MODIS, and similarly displayed two unique, land cover relationships. The wide bandpasses can include the much interference from the neighboring wavelengths and it made larger differences from MODIS values as the reflectance was increased. The AVHRR red spectral curve included the MODIS red spectral curve and was expanded to the much shorter and longer wavelengths (toward green and NIR band).



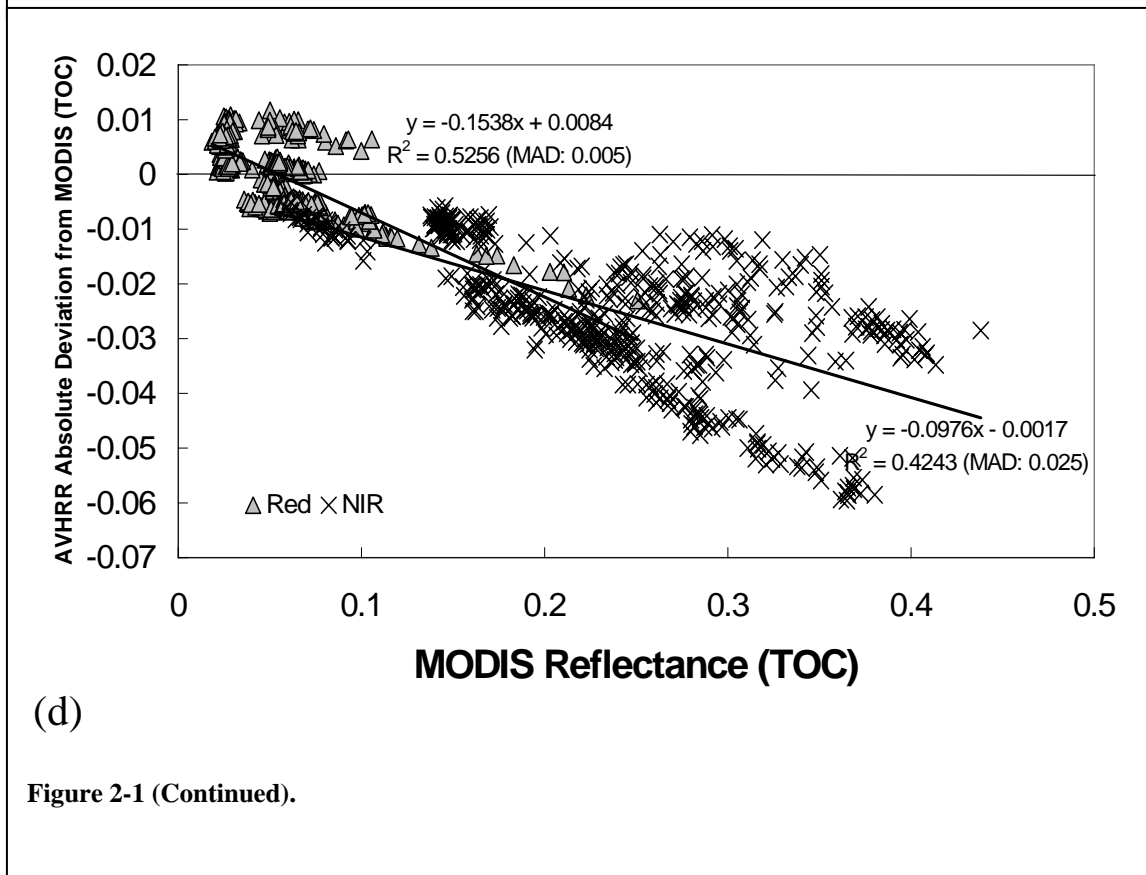
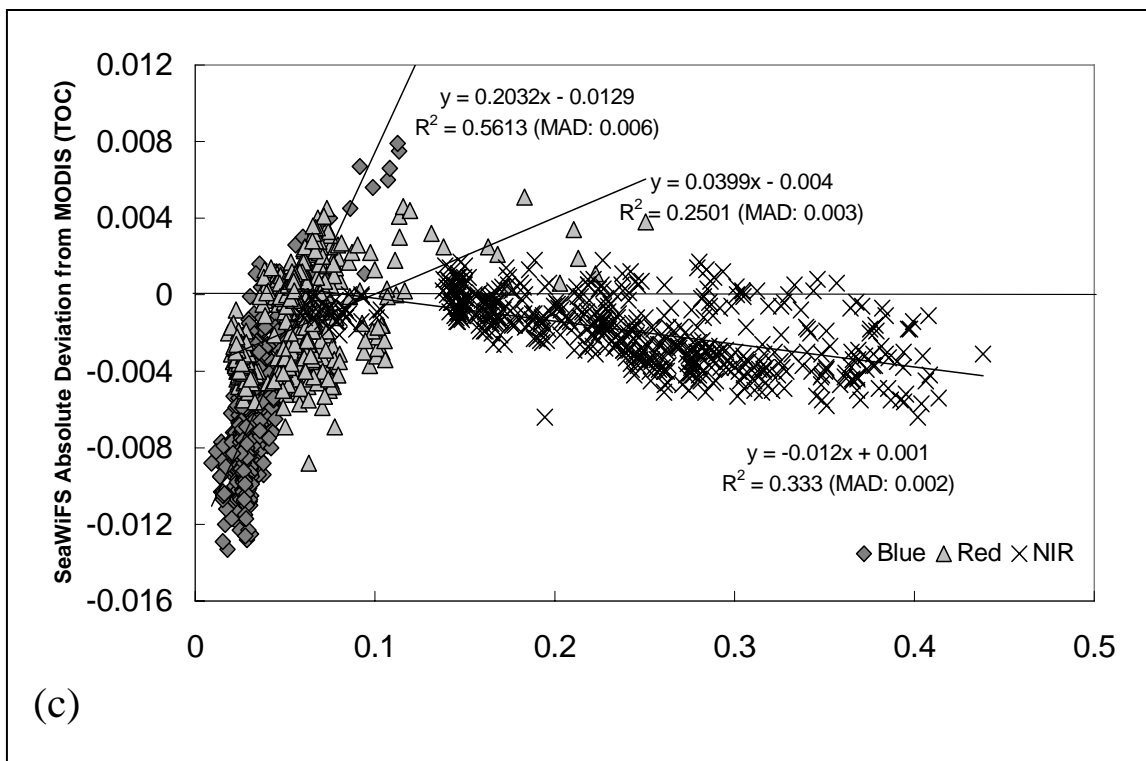


Figure 2-1 (Continued).

3.4 Cross-sensor VI analysis

Sensor differences in the EVI, EVI2, and NDVI were compared for VIIRS- MODIS, SPOT-VGT- MODIS, SeaWiFS- MODIS, and AVHRR- MODIS sensor combinations (Fig. 2-2). VI deviations between VIIRS and MODIS were mostly within -0.03 to +0.01, with EVI resulting in the greatest deviations, and EVI2 resulted in the least deviations (Fig. 2-2a). The MAD values were 0.012 (EVI), 0.002 (EVI2), and 0.005 (NDVI). There was little bias in the 2-band VI's, i.e., zero slopes, while differences between sensor EVI values increased (negative bias) with increasing EVI. Table 2-2 shows these 3 indices to be highly correlated between MODIS and VIIRS sensors, but with the EVI2 cross sensor relationship more strongly correlated than the EVI relationships. Overall EVI2 was better aligned for MODIS and VIIRS sensors than EVI, even under high biomass (Fig. 2-2a).

VI deviations between SPOT-VGT and MODIS sensors were greater and more complex with a V-shaped curvilinear relationship pattern of increasing differences followed by decreasing differences across the range of VI values, particularly evident in the NDVI (Fig. 2-2b). Overall deviations were slightly greater than between VIIRS-MODIS and ranged from -0.05 to 0, but MAD values were considerably larger and were least for EVI (0.020) and greater for the 2-band indices, 0.025 (EVI2) and 0.030 (NDVI).

VI deviations between SeaWiFS- MODIS resembled those between VIIRS- MODIS for EVI and EVI2, however, NDVI differences were much larger and biased toward higher SeaWiFS values, particularly at high NDVI values (Fig. 2-2c). EVI deviations were negatively biased, as in the VIIRS case, a result of VIIRS and SeaWiFS having

similar blue bands. The SeaWiFS NDVI was more positively biased relative to VIIRS and MODIS as a result of the lower red reflectances in SeaWiFS (Fig. 2-1c). The lower red reflectances resulted in only very slight increases in EVI and EVI2 values, as the EVI was much more sensitive to NIR than the red (Huete et al. 2002). The overall MAD values between SeaWiFS- MODIS were 0.010 (EVI), 0.005 (EVI2), and 0.014 (NDVI).

EVI2 and NDVI deviations between AVHRR and MODIS were the largest among all sensor combinations, with an overall range of differences between -0.08 and +0.02 (Fig. 2-2d). Both VI's increasingly deviated from MODIS, with negative bias, with increasing EVI2 and NDVI values. EVI2 deviations were greater than NDVI, with MAD values of 0.040 (EVI2) and 0.036 (NDVI). The lower AVHRR- VI values were a result of the same pattern of lower NIR values (Fig. 2-1d). The cross sensor differences between AVHRR and MODIS require corrections for VI continuity purposes and applications, however, the scatter in AVHRR VI values reveal at least two separate and divergent patterns, suggesting that more than empirical adjustments would be needed to ensure continuity between MODIS and AVHRR data.

Thus far, it appears that EVI2 is significantly better than EVI for cross sensor applications among MODIS, VIIRS, and SeaWiFS. Only, SPOT-VGT showed better EVI translation with a MAD of 0.020, compared with EVI2, with MAD of 0.025.

3.5 Sensitivity of cross-sensor VI differences to bandpass reflectance deviations

The sensitivities of the cross sensor differences in EVI and EVI2 to bandpass reflectance deviations in the blue, red, and NIR were analyzed to better characterize VI's.

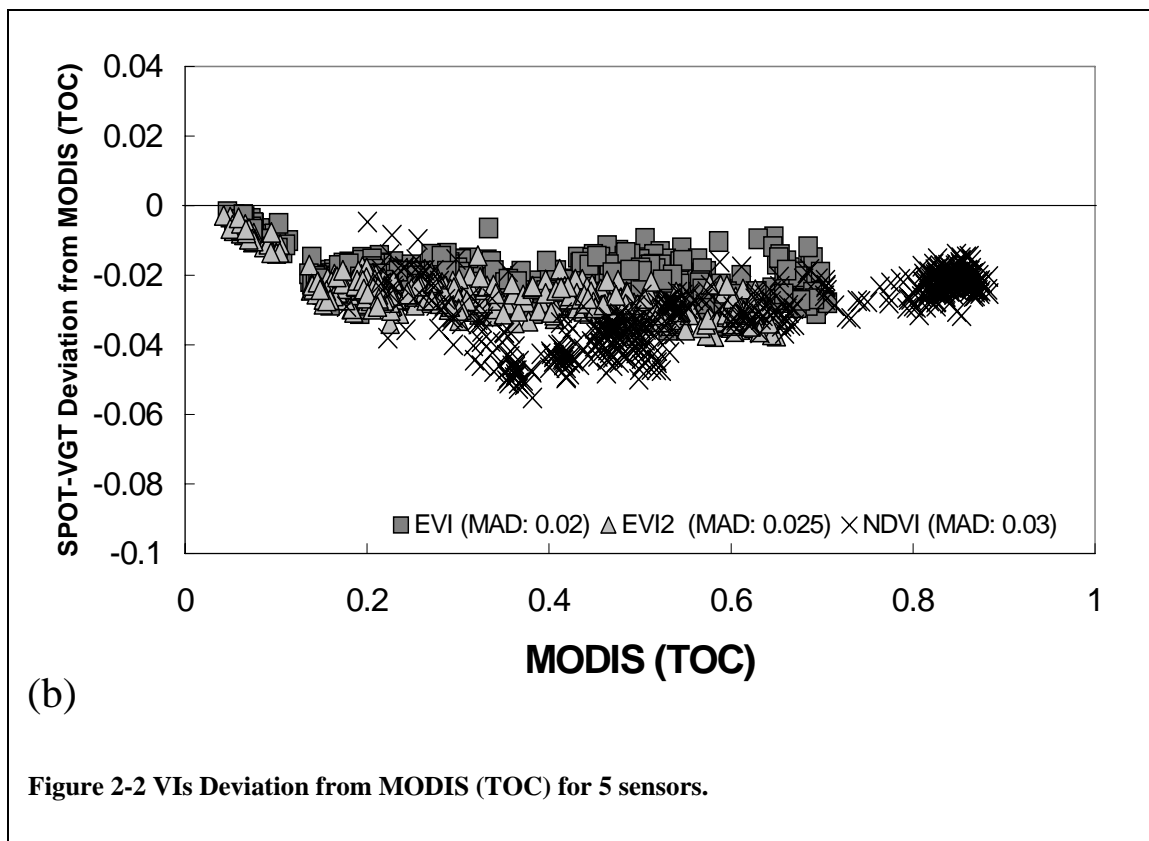
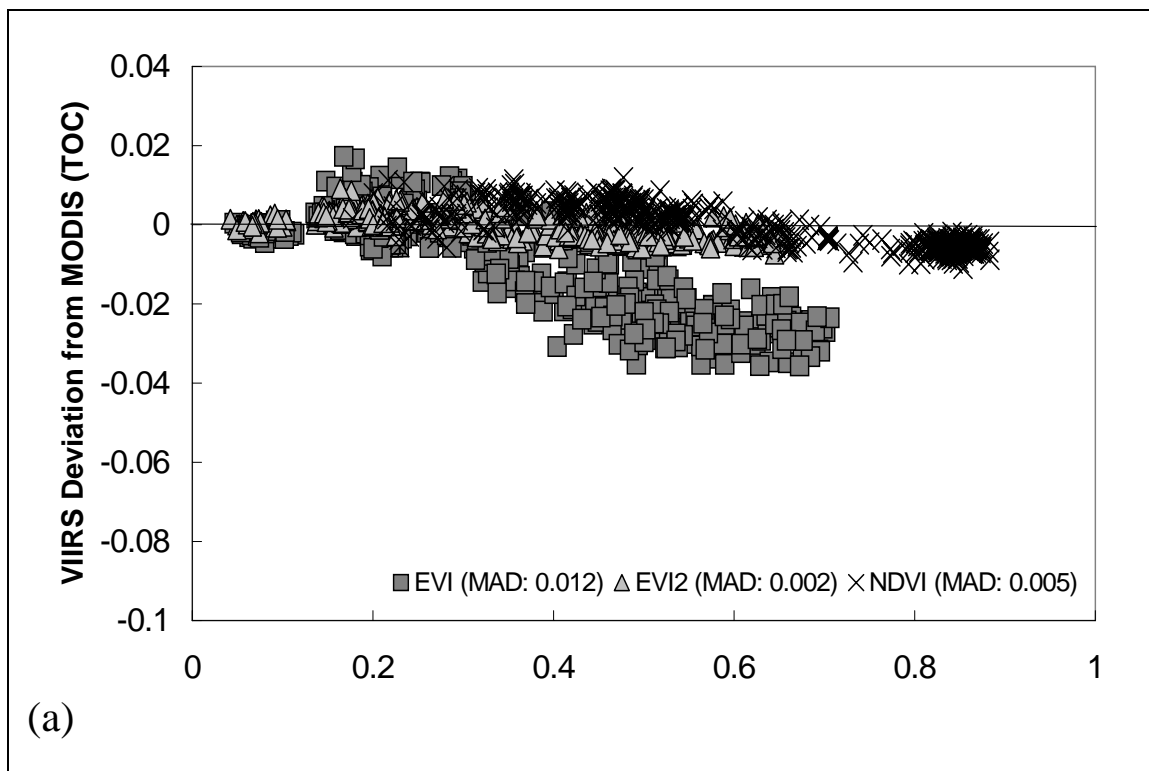


Figure 2-2 VIs Deviation from MODIS (TOC) for 5 sensors.

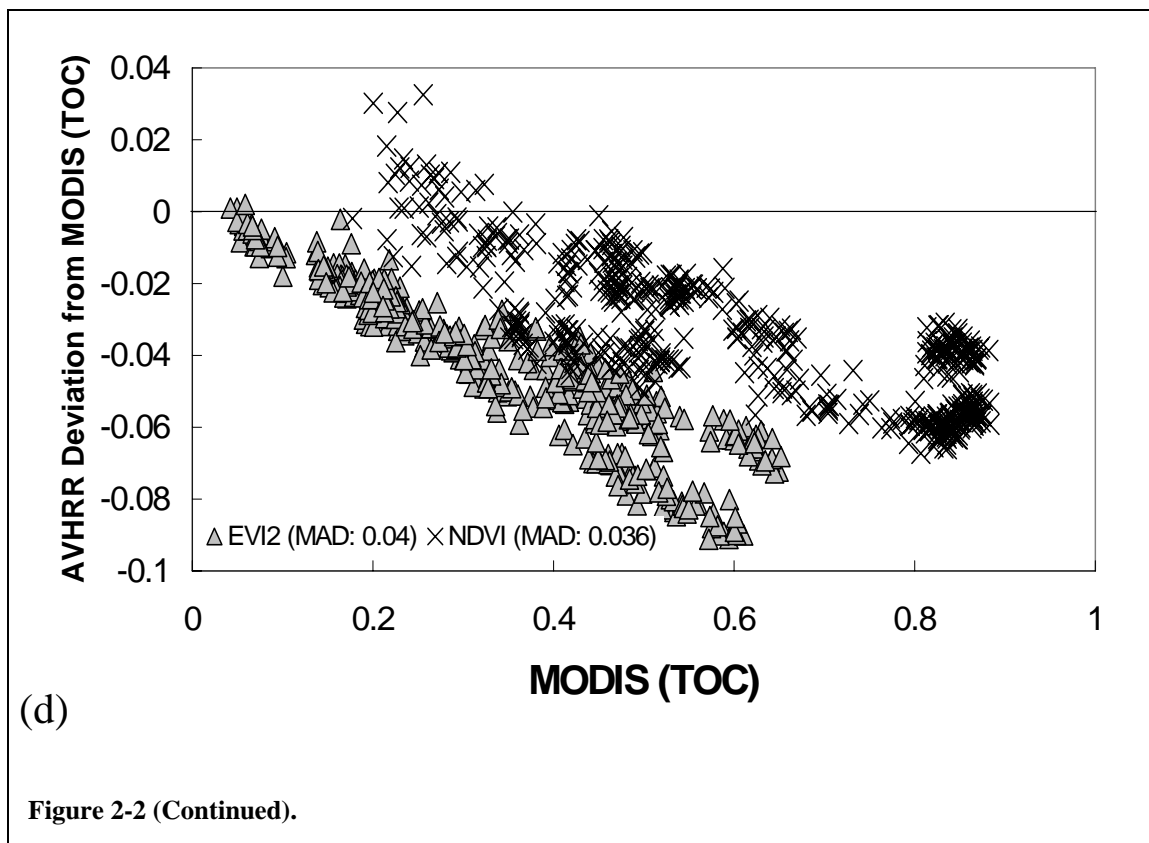
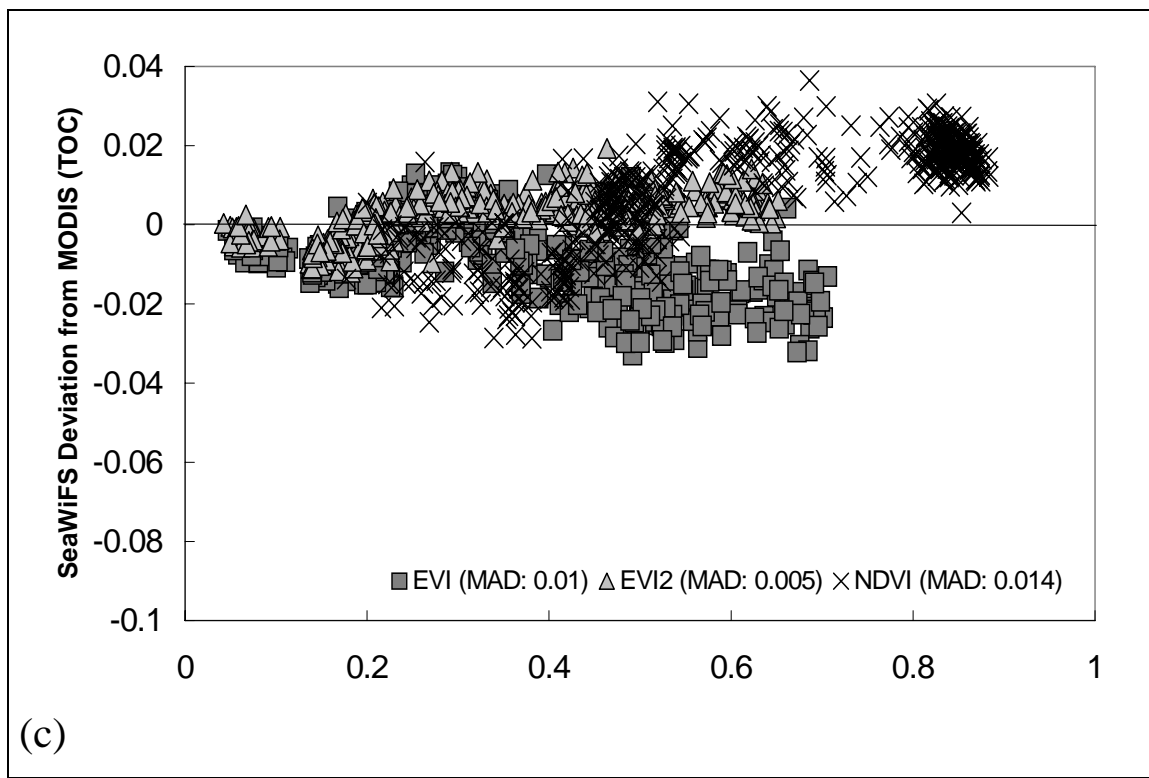


Figure 2-2 (Continued).

There were strong EVI sensitivities between VIIRS-MODIS and SeaWiFS-MODIS resulting from deviations in blue reflectances (Fig. 2-3a, c). VIIRS and SeaWiFS EVI deviations were positively related with blue reflectance deviations ($R^2=0.730$ for VIIRS and 0.477 for SeaWiFS). In contrast, SPOT-VGT and MODIS EVI differences were not correlated with changes in blue reflectance, but were moderately correlated with inter-sensor differences in the red ($R^2=0.579$) and NIR ($R^2=0.546$). The VIIRS- MODIS sensor EVI differences were strongly sensitive to blue reflectance deviations ($R^2=0.730$) and red reflectance deviations ($R^2=0.760$), but mostly insensitive to NIR reflectance deviations ($R^2=0.281$). Cross sensor deviations in EVI between SeaWiFS and MODIS were mostly due to a moderate sensitivity to blue reflectance differences, $R^2=0.477$, with no relationship to red reflectance changes, $R^2=0.001$, and smaller sensitivity to NIR differences, $R^2=0.399$.

This suggests that EVI differences between MODIS and VIIRS, and MODIS and SeaWiFS were mostly a result of blue reflectance deviations, as also seen in Fig. 2-1a, c. The SPOT-VGT EVI deviations from MODIS was mostly ascribed to red reflectance ($R^2=0.579$) and NIR reflectance ($R^2=0.546$) deviations, with no sensitivity to blue reflectance differences ($R^2=0.083$) (Fig. 2-3b). Thus, one reason the EVI2 did not improve upon cross-sensor relationships between SPOT-VGT and MODIS, was partly due to this insensitivity to blue band variations.

VIIRS- MODIS EVI2 differences were dependent on both red ($R^2=0.714$) and NIR ($R^2=0.655$) reflectance variations (Fig. 2-3d, e). This sensitivity to red and NIR band variations improved the EVI2 continuity to MODIS upon cross-sensor relationships

between VIIRS and MODIS, due to similar red and NIR spectral response function. Differences in EVI2 across SeaWiFS and MODIS sensors were predominantly related to red reflectance deviations ($R^2=0.851$), and was insensitive to variations in the NIR ($R^2=0.009$) (Fig. 2-3f). EVI2 differences between SPOT-VGT and MODIS were also dependent on differences between both red and NIR reflectances ($R^2=0.562$ and 0.919 , respectively) (Fig. 2-3e), while EVI2 differences between MODIS and AVHRR were more strongly related to NIR reflectance deviations ($R^2=0.628$), relative to red ($R^2=0.336$) (Fig. 2-3g).

3.6 Cross-sensor blue-red coherency analysis

Multi-band coherencies of blue and red reflectances for the 4 applicable sensors are shown in Fig. 2-4. Thus, despite the strong cross-sensor relationships found with each band individually, the blue-red cross-band relationships were somewhat weaker, with R^2 values ranging from 0.904, in the case of VIIRS, to $R^2=0.819$ for SPOT-VGT. However, more relevant to cross-sensor coherencies of the EVI, are the slope and intercept of the sensor-specific red-blue relationships. Whereas, SPOT-VGT had slope and intercept terms (2.08 and -0.023) which most closely approximated those from MODIS (2.09 and -0.017), VIIRS and SeaWiFS deviated the most from MODIS with red-blue slope and intercept parameters of (1.783 and -0.0002), and (1.841 and 0.001), respectively. The high correlations observed for each sensor in Fig. 2-4 demonstrated the feasibility of the only use of the red band instead of the blue band for EVI.

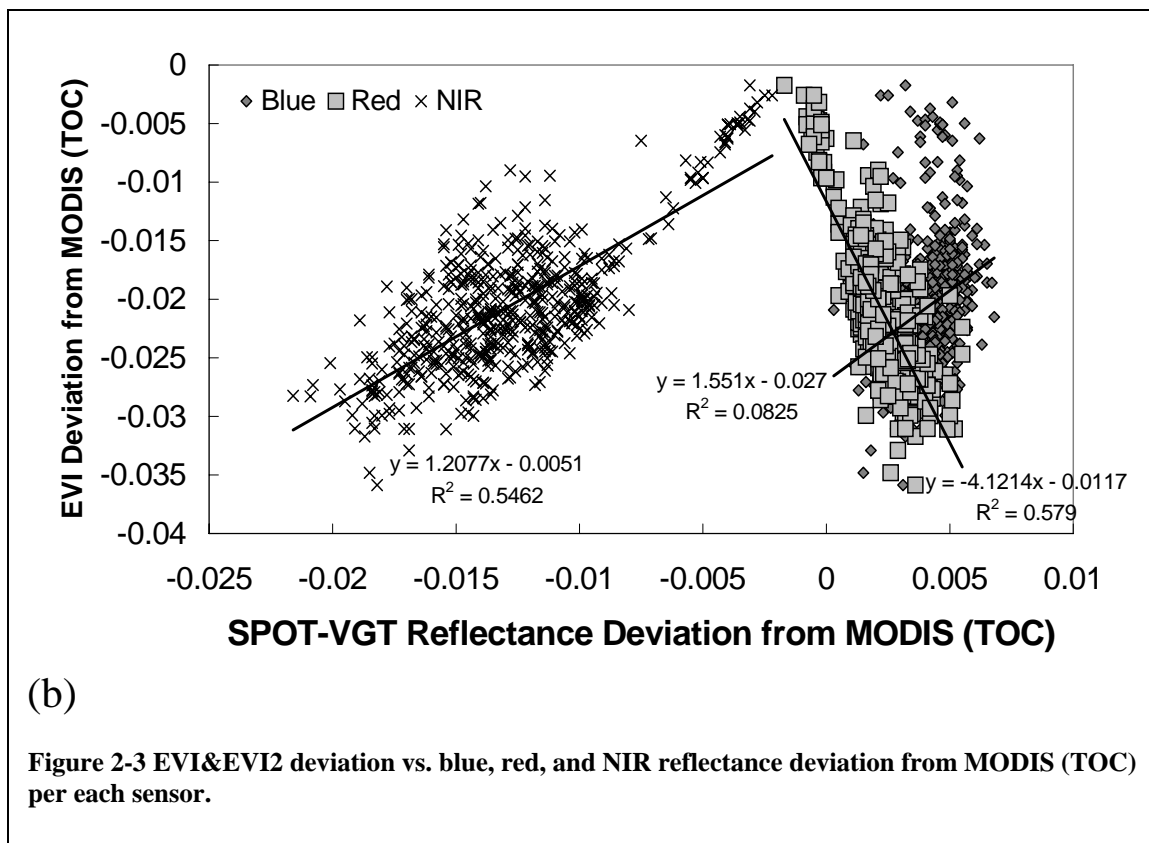
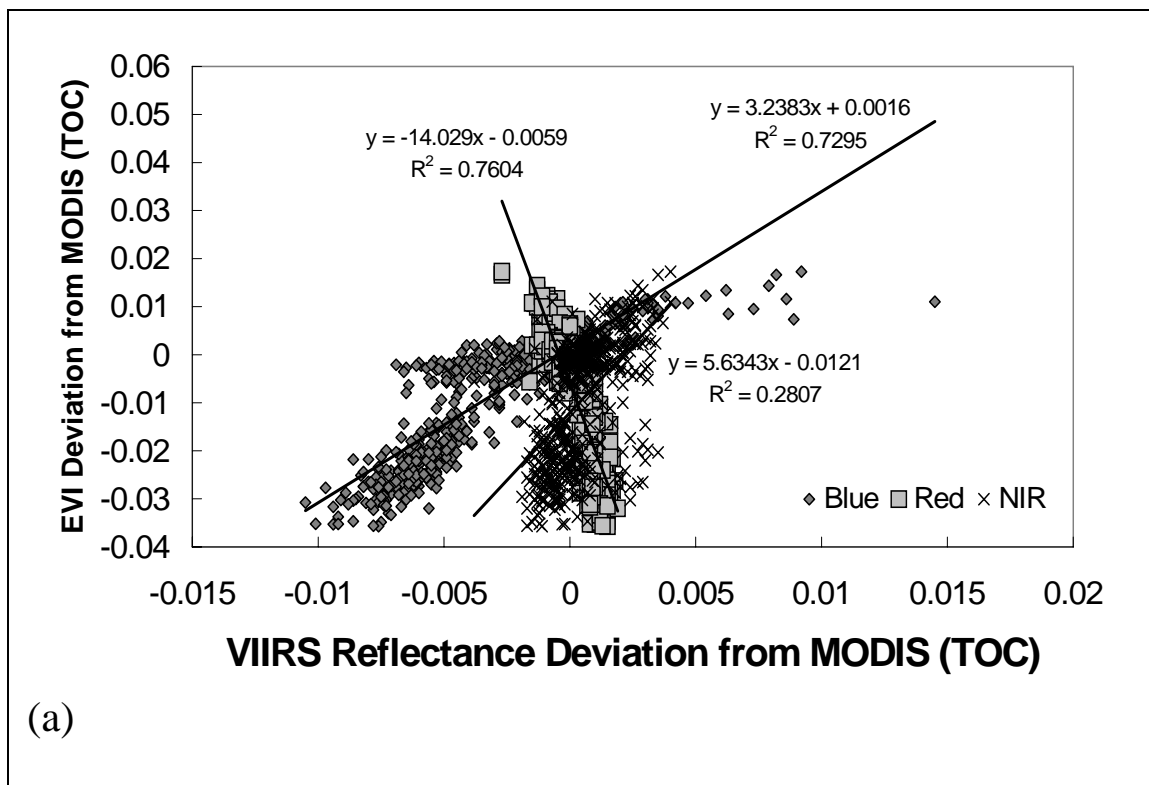


Figure 2-3 EVI&EVI2 deviation vs. blue, red, and NIR reflectance deviation from MODIS (TOC) per each sensor.

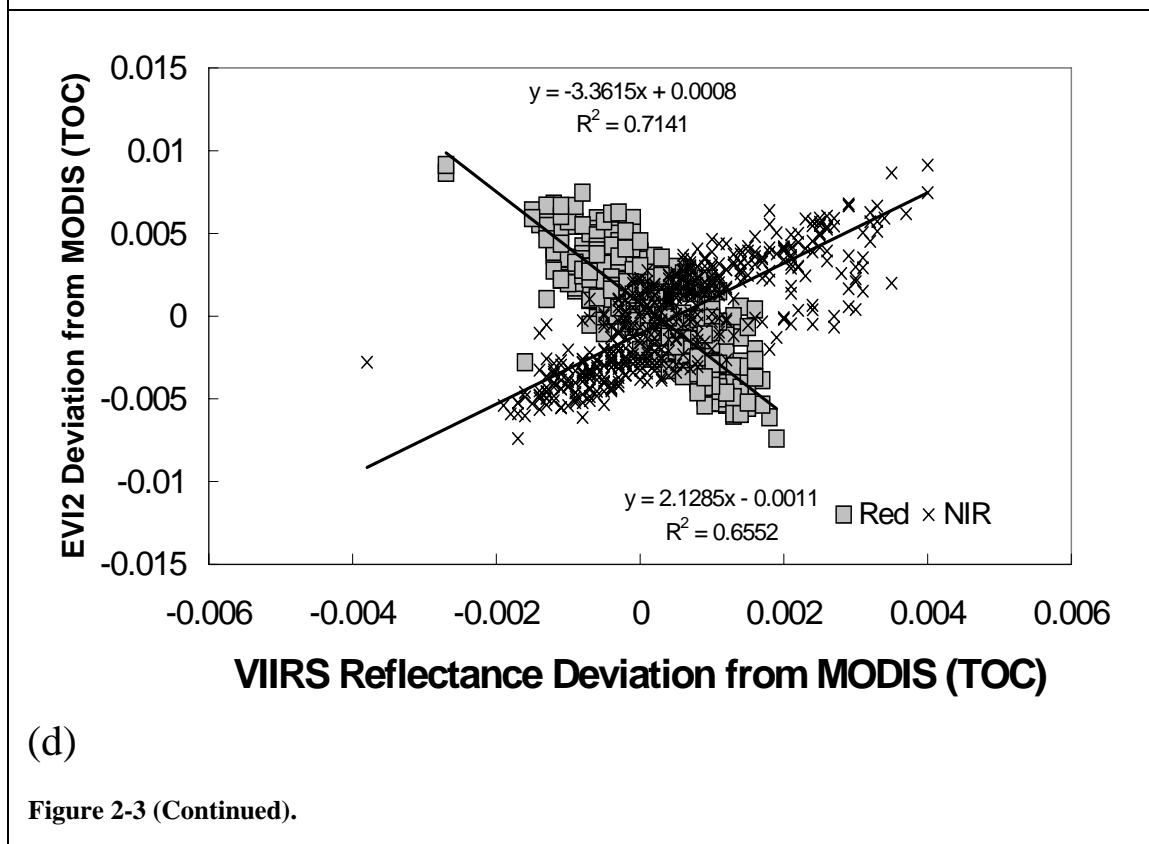
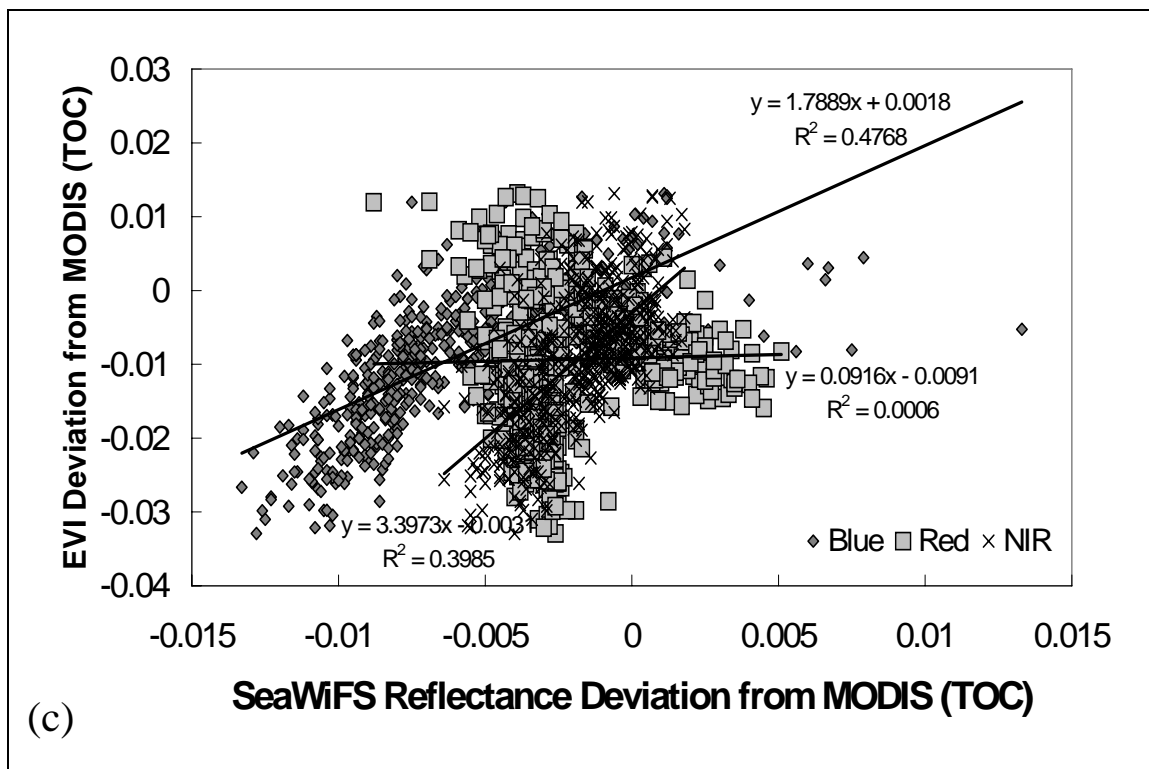


Figure 2-3 (Continued).

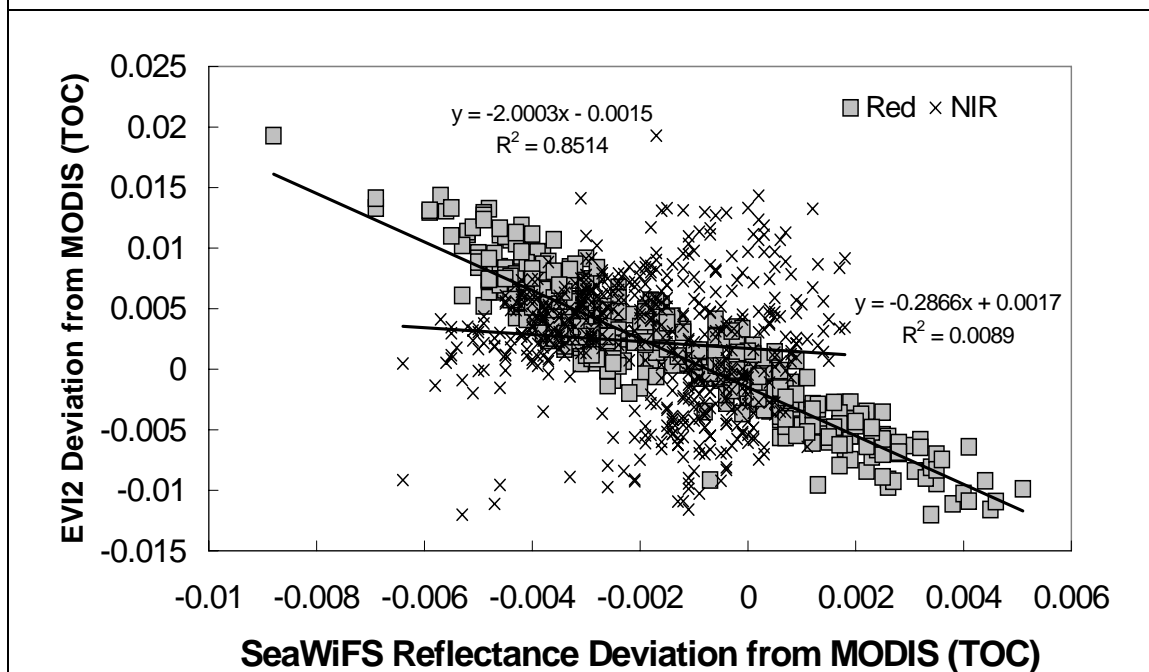
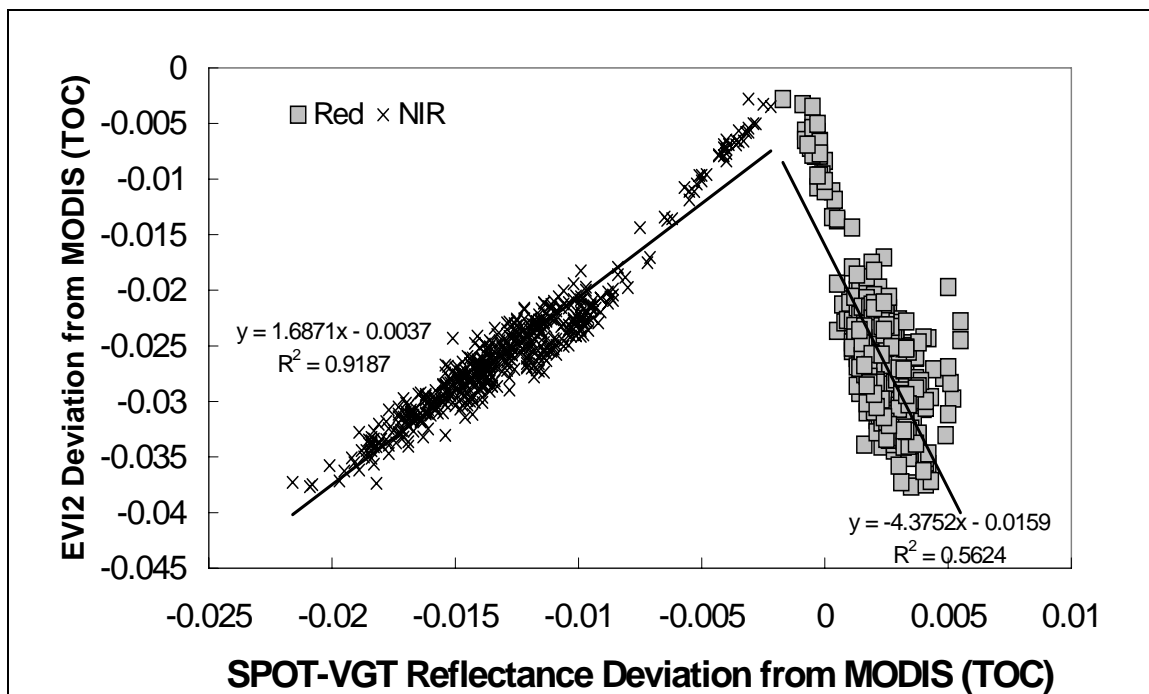
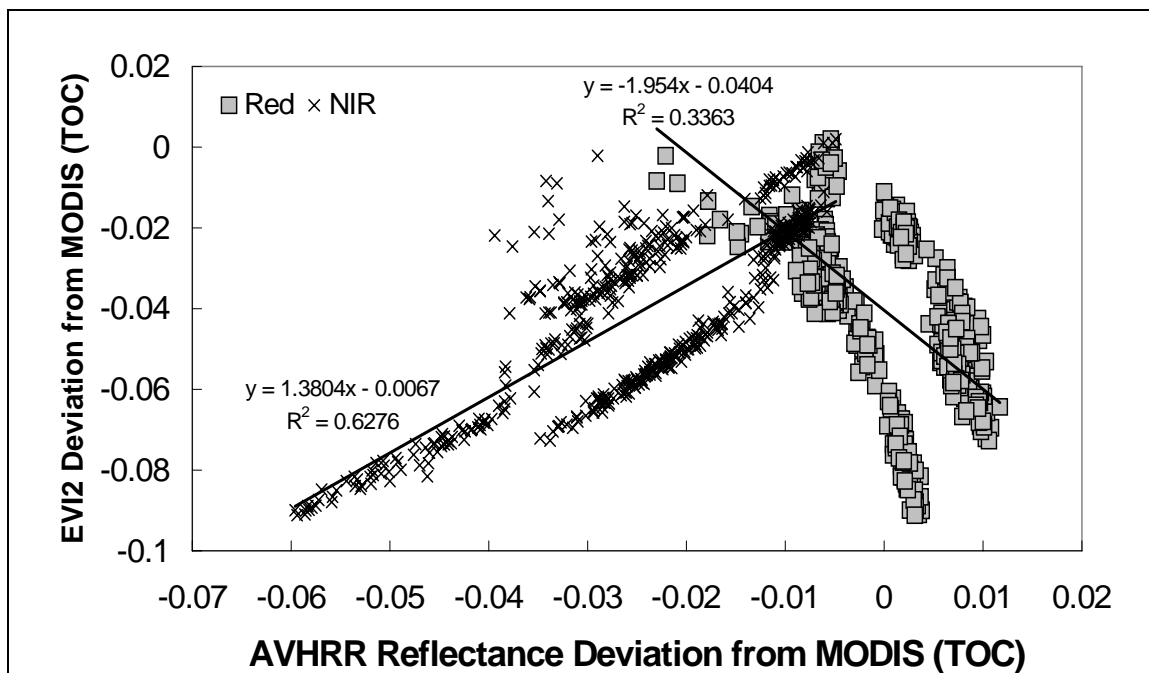


Figure 2-3 (Continued).



(g)

Figure 2-3 (Continued).

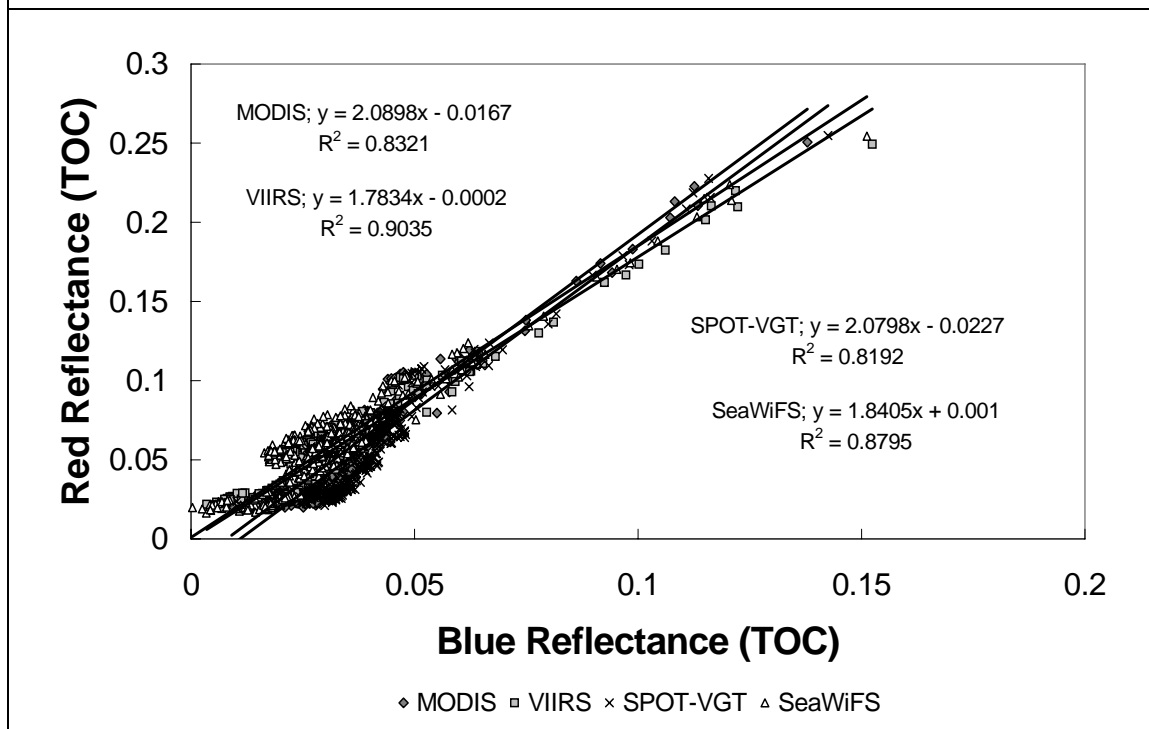
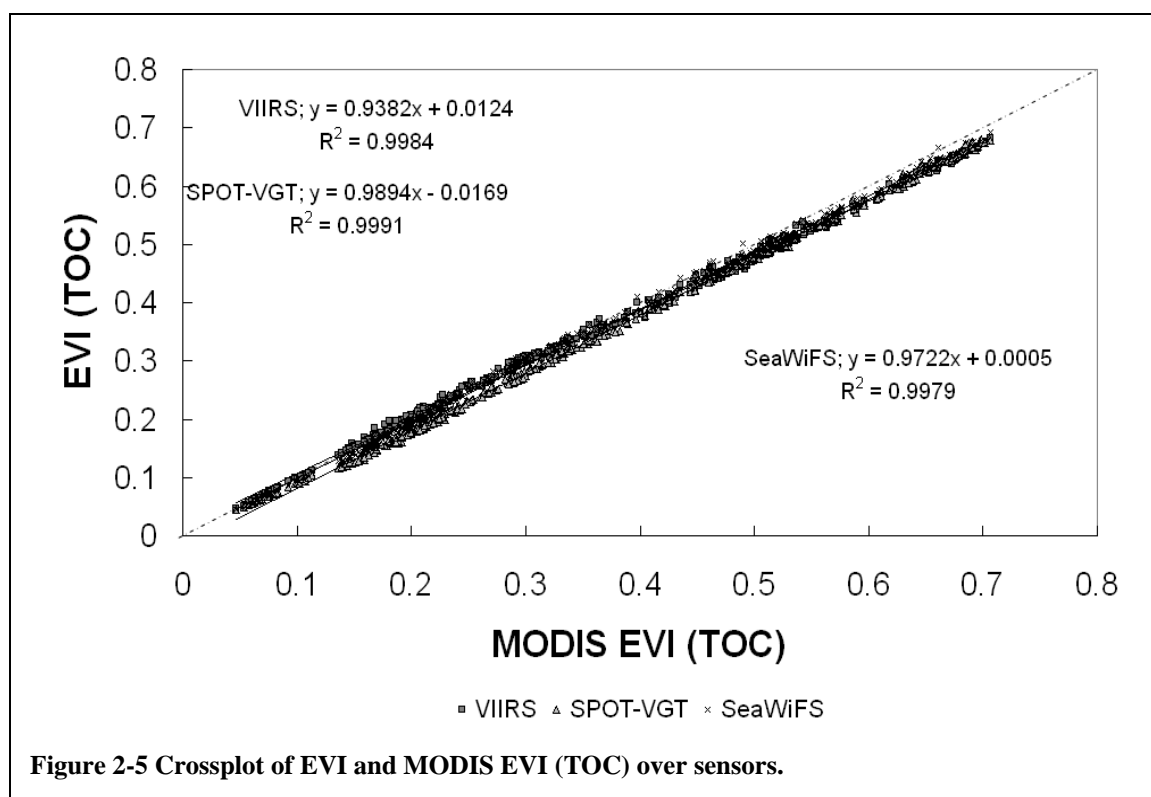


Figure 2-4 Spectral coherencies on blue and red reflectance using the hyperspectral convolution.

The following crossplots described cross-sensor EVI and EVI2 relationships. In Fig. 2-5, inter-sensor transforms for EVI between sensor and MODIS were provided. Linear relationships between sensors and MODIS were established in the crossplots. There was a bridge-like inter-sensor equation in Fig. 2-6. Sensor EVI2 relative to MODIS EVI were presented to convert future EVI2 products from current MODIS EVI products. Fig. 2-7 showed inter-sensor translations of EVI2 between sensor and MODIS. The MODIS EVI2 value was mostly larger than the EVI2 value for each sensor, excluding VIIRS and SeaWiFS. VIIRS and SeaWiFS EVI2 value is close to the diagonal, 1:1 line. Therefore, the sensor EVI2 continuity and compatibility to MODIS EVI2 was improved per each sensor pair, because R^2 between sensor and MODIS EVI2 was larger than that between sensor and MODIS EVI.



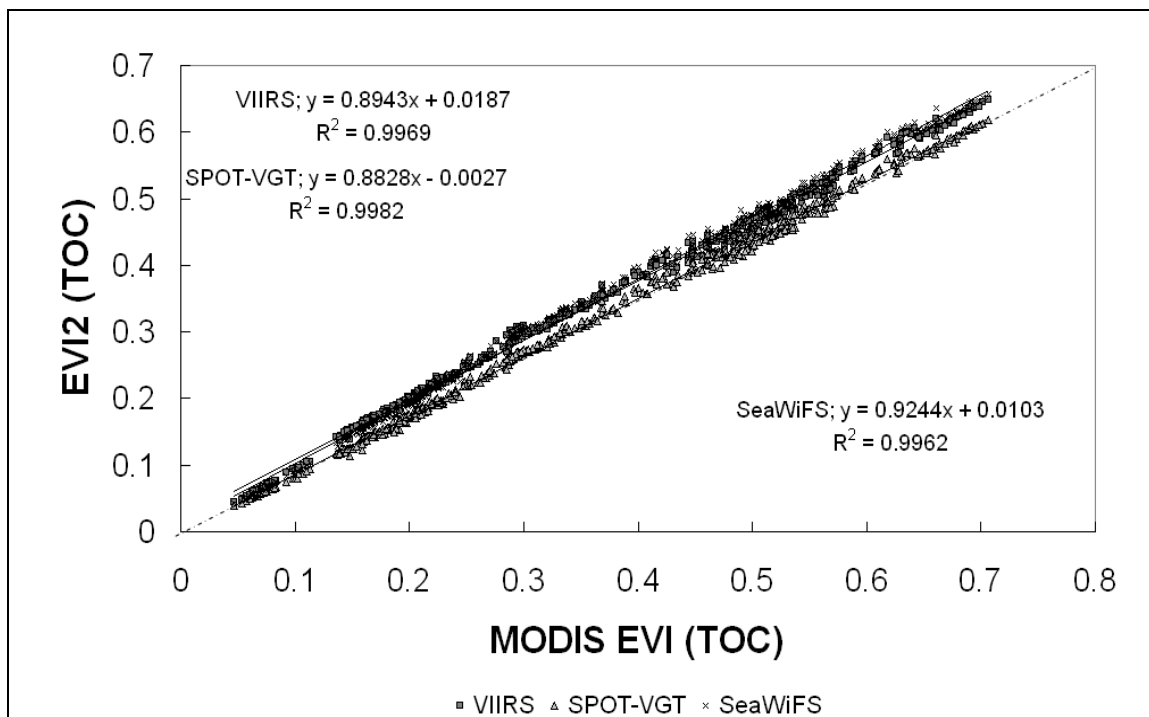


Figure 2-6 Crossplot of EVI2 and MODIS EVI (TOC) over sensors.

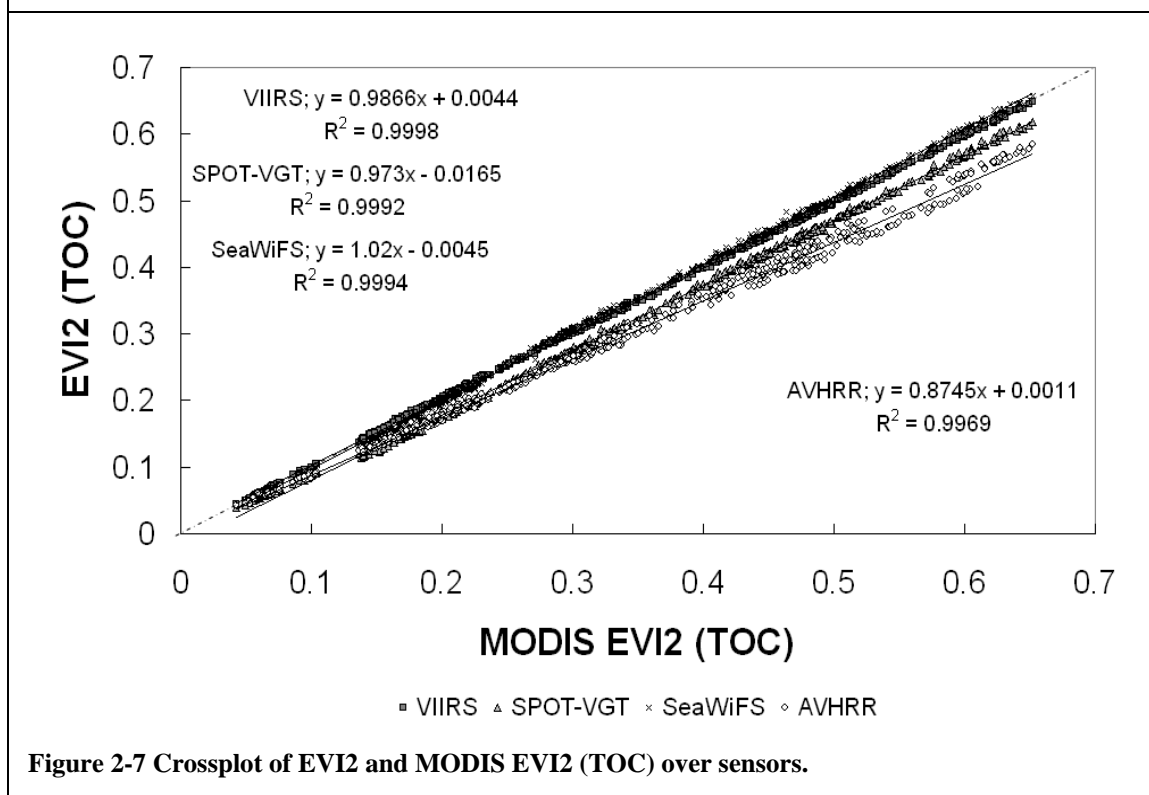


Figure 2-7 Crossplot of EVI2 and MODIS EVI2 (TOC) over sensors.

3.7 The sensitivity of red to blue ratios regarding MODIS values

To assess the ratio of red to blue reflectance per land cover type and sensor relative to MODIS, 6 land cover types were selected from three study sites by field survey with GPS measurements. The ratio of red to blue reflectance has been used to optimize the coefficient of EVI2 (Jiang et al. 2007, submitted). In many cases, the variation of the ratio from MODIS resulted in making sensor continuity hard for various land cover type regarding all sensor combinations. The variation of VIIRS and SeaWiFS ratios was similar except for cerrado (savanna) sites (Fig. 2-8b, c). In the primary forest area (Fig. 2-8a), the ratios of red to blue from VIIRS and SeaWiFS were far away from one-to-one line, while those of SPOT-VGT were mostly close to one-to-one line. In Fig. 2-8b, c (cerrado regions), VIIRS and SeaWiFS ratios were above the 1:1 line and SPOT-VGT ratios were smaller, or below the 1:1 line than MODIS ratios. SeaWiFS ratios became larger with increasing MODIS ratios, resulting from relatively more red and less blue deviations from MODIS at higher ratios. There were the least deviations from the 1:1 line across sensors in the cultivated pasture (Fig. 2-8d). The ratios patterns in Sel logged forest were quite similar to those in the dense forest area (Fig. 2-8e). In converted pasture, VIIRS and SeaWiFS ratios were above the 1:1 line and SPOT-VGT ratios were below the 1:1 line (Fig. 2-8f). But, VIIRS and SeaWiFS ratios became close to the 1:1 line as MODIS ratio was increased. The ratios of red to blue reflectance across sensors fell always along or close to the diagonal, 1:1 line in cerrado areas, cultivated pasture, and converted pasture (Fig. 2-8b, c, d, and f). The ratios of red to blue from VIIRS and SeaWiFS were different from MODIS ratio in forest sites (Fig. 2-8a, e). Mostly, the ratios

from SPOT-VGT were very close to MODIS ratios, irrespective of land cover types, while the ratio variations from VIIRS and SeaWiFS were dependent on land cover types.

3.8 Land cover influences on cross-sensor reflectances, VIs and EVI-EVI2 differences

We studied the reflectances and VIs differences based on the spectral response functions for each sensor pairs. For the purpose of the EVI2 continuity to MODIS EVI across the sensors with the different spectral response curves, especially red and NIR bands, a minimal MAD between MODIS and sensors should be considered for various land cover types. Fig. 2-9 described the land cover effects on cross-sensor reflectances, VIs and EVI-EVI2 differences for three sensors (VIIRS, SPOT-VGT, and SeaWiFS). Even if VIIRS and SeaWiFS had a similar pattern on reflectances and VIs deviations, MAD analysis (sensor values – MODIS values) provided different values per each land covers.

MAD from VIIRS red and NIR reflectances were not much varied, with an offset of $< \sim 0.002$ reflectance unit, while MAD from VIIRS blue was not uniformly distributed (0.0015 – 0.0065) (Fig. 2-9a). MAD from VIIRS NDVI and EVI2 was uniform with an offset of < 0.007 (Fig. 2-9b), while that of VIIRS EVI was varied according to land cover types, showing close relationship with blue reflectance MAD. Thus, the difference of EVI-EVI2 was followed by the variations of blue reflectance and EVI MAD. In forest area and converted pasture, MAD of VIIRS EVI became higher up to 0.025 (MAD

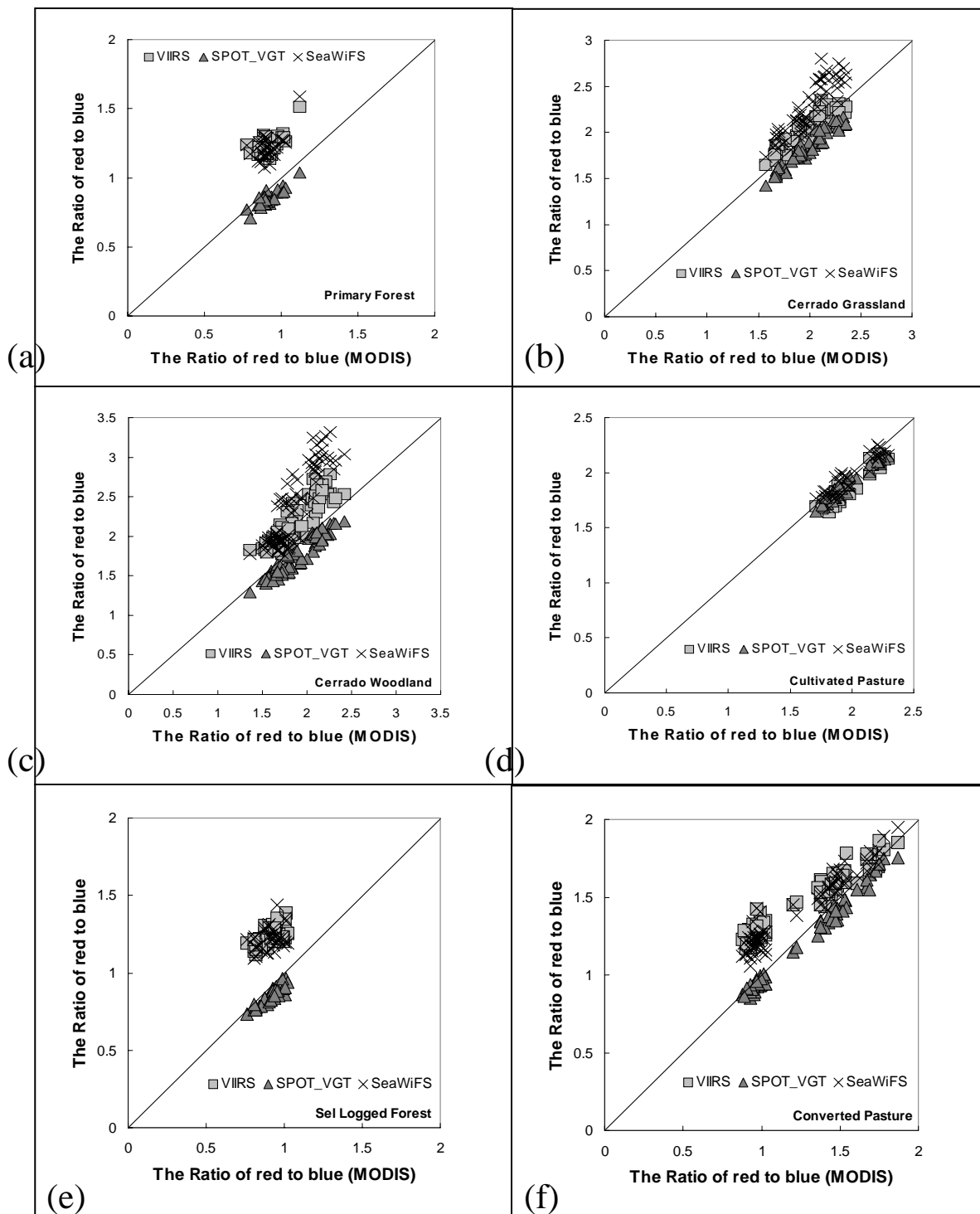


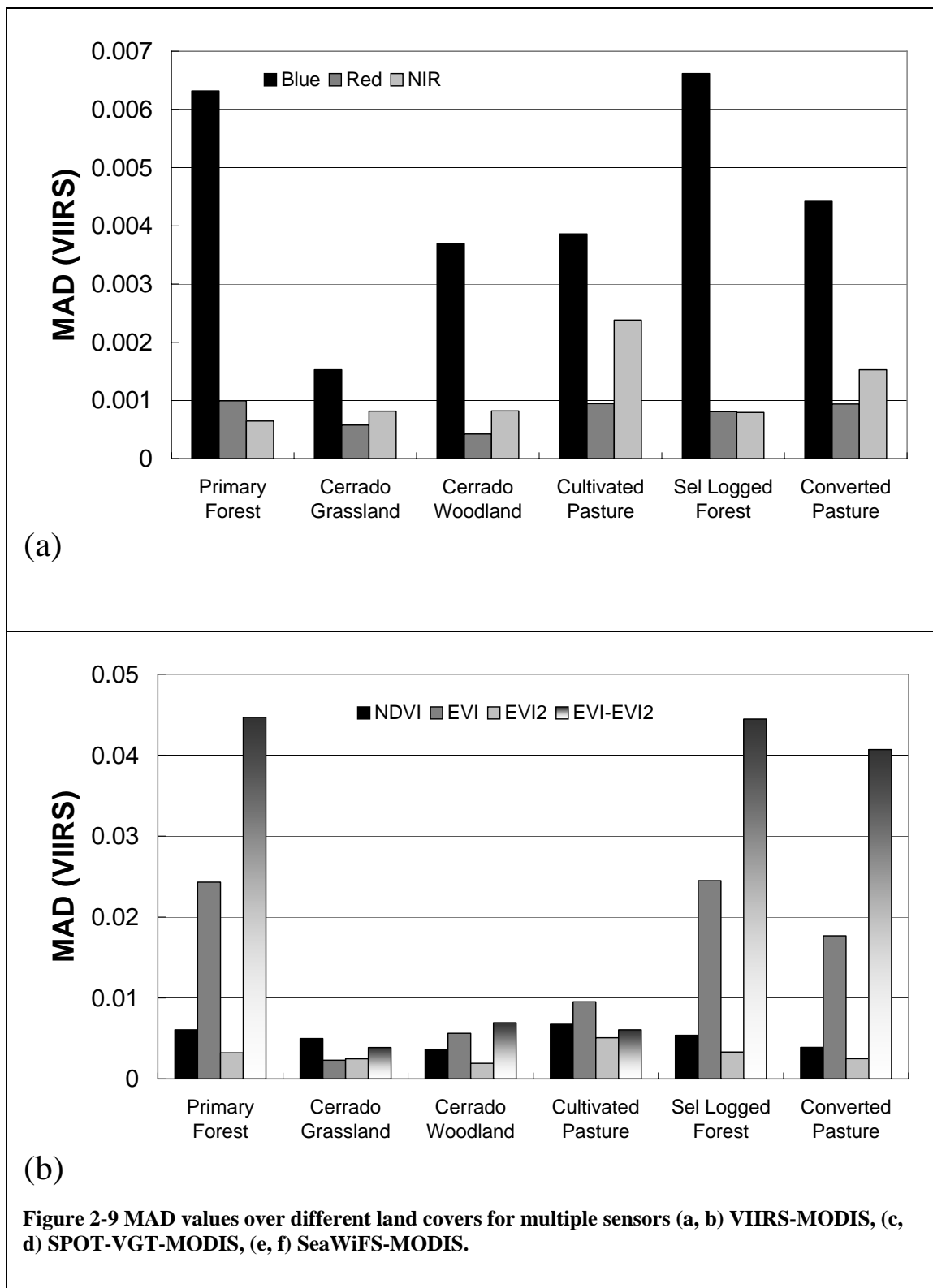
Figure 2-8 The comparison of the ratio of red to blue regarding MODIS values over different land covers for multiple sensors ((a) Primary Forest, (b) Cerrado (Savanna) Grassland, (c) Cerrado (Savanna) Woodland, (d) Cultivated Pasture, (e) Sel Logged Forest, and (f) Converted Pasture).

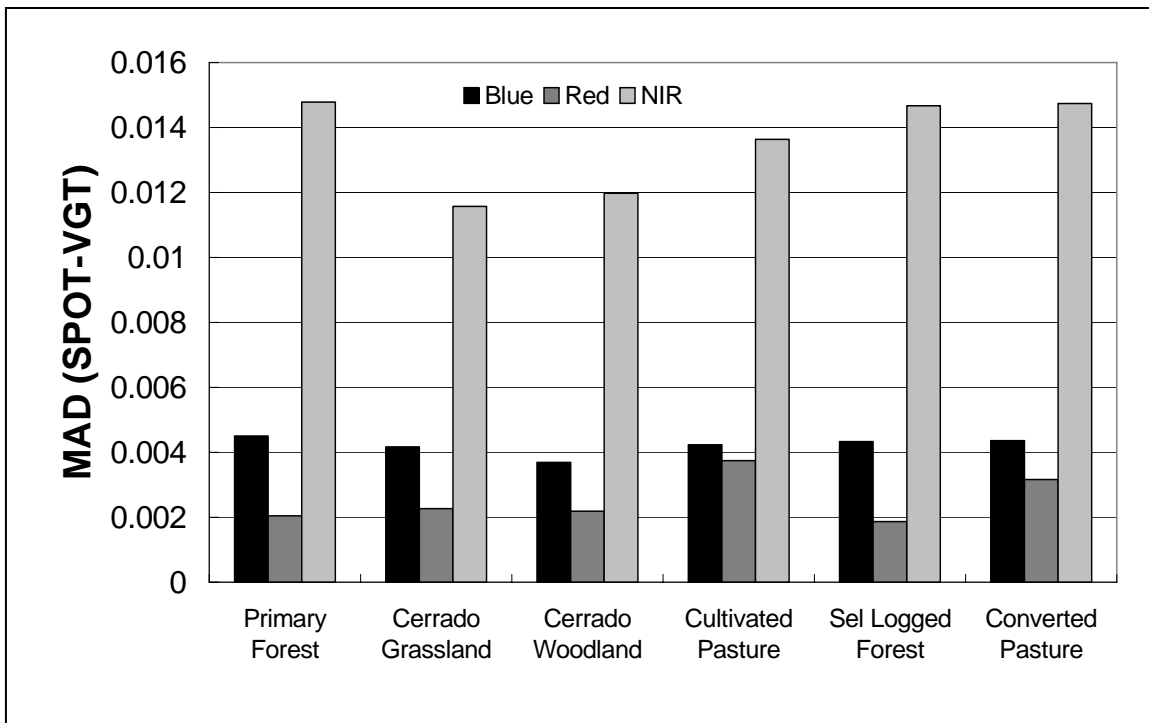
average of 0.012 in Table 2-2), resulting in larger MAD (~0.045) of EVI-EVI2 (MAD average of 0.011 in Table 2-2).

As for SPOT-VGT, MAD values from blue and red reflectances were less than 0.005 over 6 land cover types (Fig. 2-9c). MAD from SPOT-VGT NIR reflectance (~0.015) became larger than that from blue and red reflectances as shown in Fig. 2b. MAD from SPOT-VGT EVI and EVI2 was distributed uniformly, its values (0.02~0.03), however, they were larger than MAD from SPOT-VGT reflectances (Fig. 2-9d). MAD from SPOT-VGT NDVI was quite different from VIIRS NDVI MAD pattern. MAD in non-forest area (cerrado and cultivated pasture) was higher than forest area. MAD from EVI-EVI2 was similar to VIIRS value (still larger in forest area). SPOT-VGT EVI-EVI2 independency on land covers was confirmed as VIIRS EVI2.

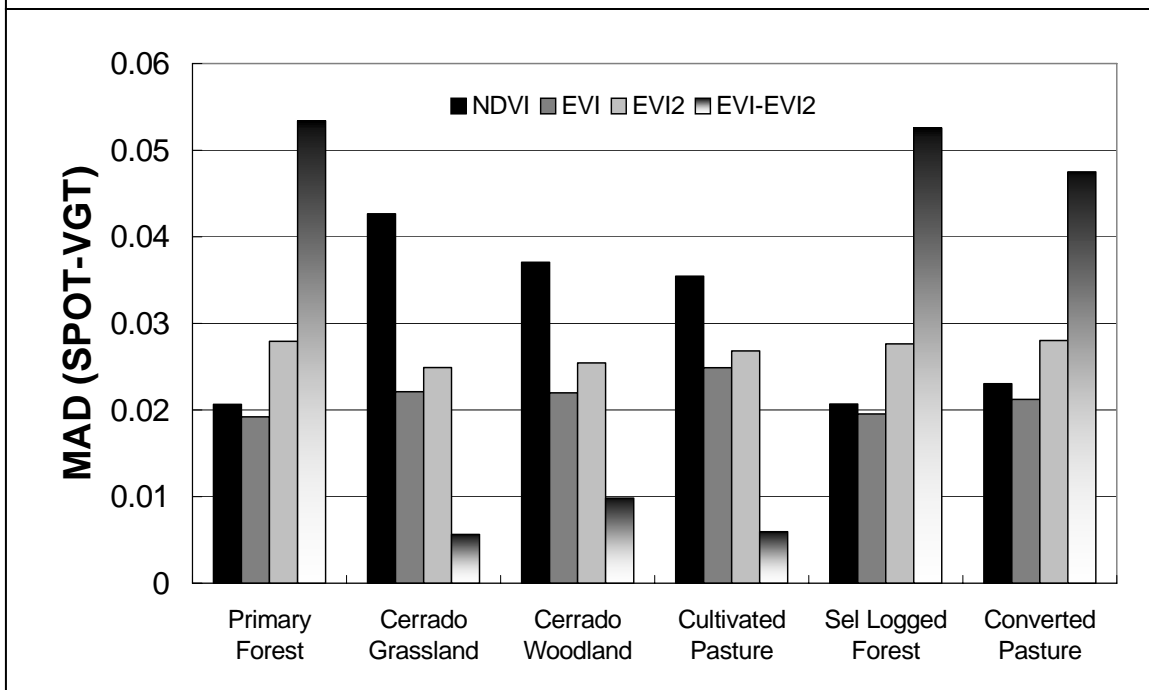
In Fig. 2-9e, the MAD from SeaWiFS blue reflectance was larger than red and NIR reflectance, particularly in forest area, it had the largest MAD values (~0.009) among sensor combinations. SeaWiFS EVI2 MAD was relatively constant distribution, while SeaWiFS NDVI and EVI were quite dependent on land cover types (Fig. 2-9f).

The VIIRS and SeaWiFS EVI2 had the minimum (and constant) MAD (<0.005) over 6 land cover types, while SPOT-VGT EVI2 (~0.028) had the maximum (but uniform) MAD across 6 land cover types. EVI2 variation from MODIS could be non- sensor- and site-specific dependent. As for EVI-EVI2, MAD in forest area had the largest values (the least values in cerrado sites). It implied forest area might affect MAD between EVI and EVI2 more, due to EVI and blue band differences.





(c)



(d)

Figure 2-9 (Continued).

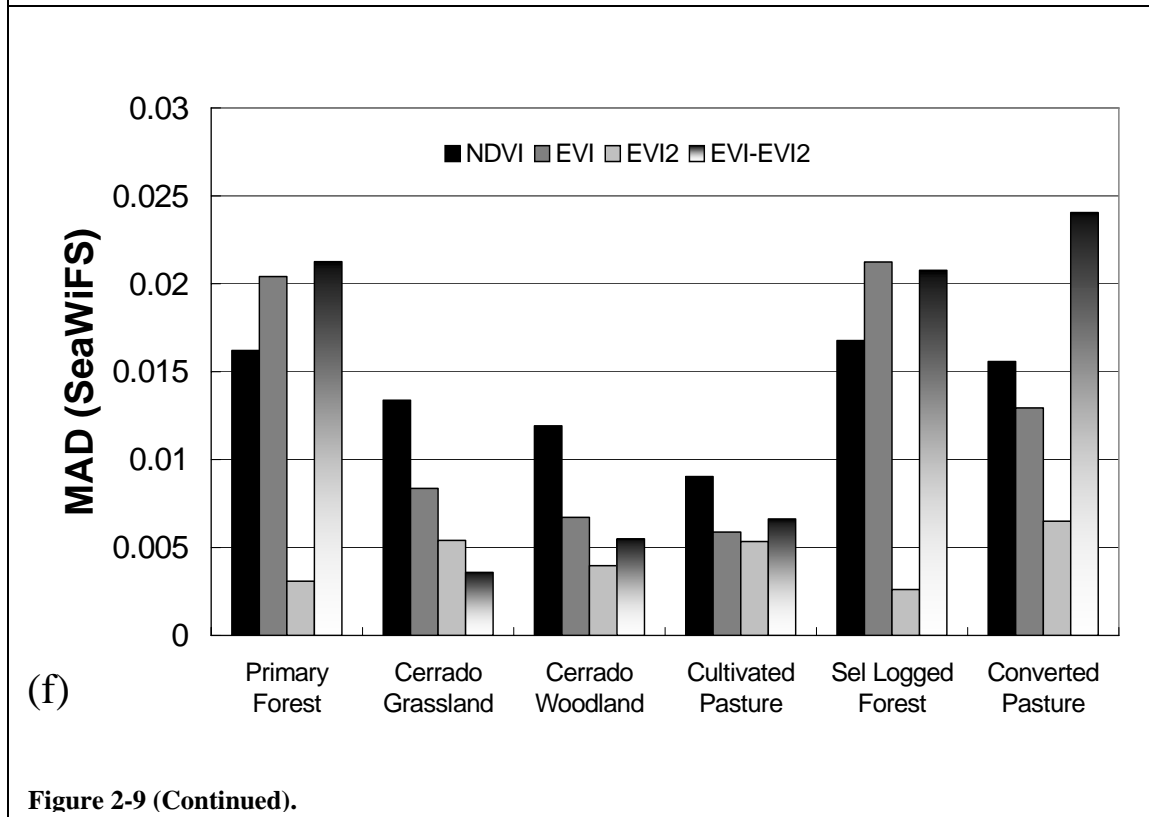
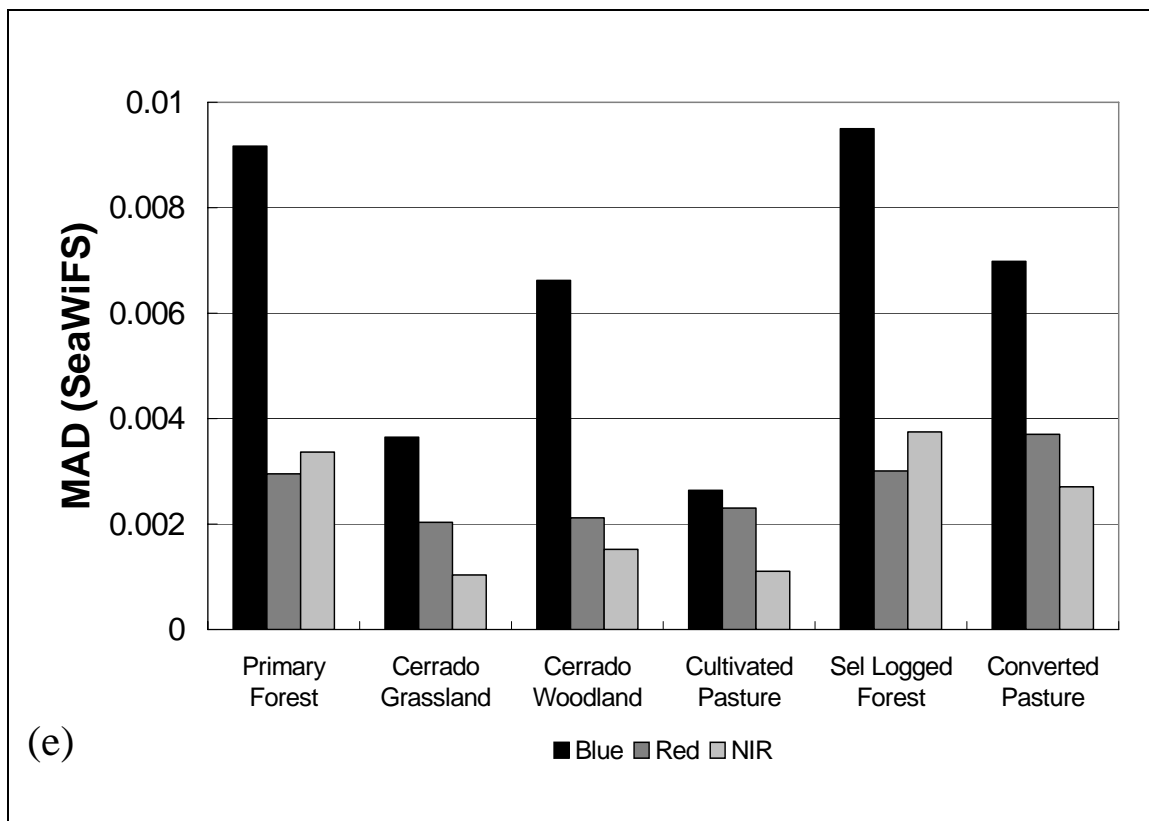


Figure 2-9 (Continued).

4. Conclusions and Discussion

We have analyzed the relationships of blue, red, and NIR reflectances, VIs deviations from MODIS values, the sensitivity of cross-sensor EVI and EVI2 differences, the blue-red spectral coherency, and land cover influences on the ratio of red to blue, reflectances, VIs, and EVI-EVI2 differences.

We found different spectral response curves resulted in reflectance and VIs deviations and strong effects on land cover types, particularly in VIIRS and SeaWiFS blue bands. VIIRS and SeaWiFS EVI2 was proposed by NDVI-like equation without the blue band which is easily affected by atmosphere, VIIRS and SeaWiFS EVI with blue band showed much complexity to inter-sensor continuity.

The VIIRS and SeaWiFS blue reflectance deviations behaved in the similar way and had large range, compared with SPOT-VGT. The SPOT-VGT red reflectance was similar with the MODIS red reflectance, while SPOT-VGT NIR reflectance was critically different from the MODIS NIR reflectance. The VIIRS and SeaWiFS red and NIR reflectance deviations from MODIS values were distributed in the similar way. The AVHRR reflectance in the red and NIR bands was quite different from MODIS, because the wide bandpass could include the much interference from the neighboring wavelengths. Through the reflectance and VIs deviation analyses, we understood that the VIIRS and SeaWiFS blue band translation as well as EVI translation from MODIS sensor were very difficult and complex, resulting in problematic EVI continuity to MODIS.

VIIRS EVI deviation from MODIS was related from blue (positively) and red (negatively) reflectance deviations from MODIS. Blue reflectance deviation resulted

from different spectral response function from MODIS was strongly affected by land cover types. VIIRS EVI2 deviation was less relative to red (negative) and NIR (positive) reflectance deviations compared with VIIRS EVI. SeaWiFS EVI deviation was moderately related to blue (positively) and NIR (positively) reflectance deviations. Blue reflectance deviation was attributed from different spectral response curve from MODIS and more deviated regarding land cover types, while NIR reflectance deviation was less dependent on land cover types. SeaWiFS EVI2 deviation was negatively relative to red reflectance deviation. Red reflectance deviation was less ascribed to different spectral response function from MODIS than the red dependency of SeaWiFS EVI. Red reflectance deviation was not strongly affected by land cover types. SPOT-VGT EVI and EVI2 were moderately related to red (negatively) and NIR (positively) reflectance deviations.

Thus far, it appeared that EVI2 was significantly better than EVI for cross sensor applications among MODIS, VIIRS, and SeaWiFS. Only, SPOT-VGT showed better EVI translation with a MAD of 0.020, compared with EVI2, with MAD of 0.025 due to dissimilarity of NIR spectral response function and its dependency on land cover types. One reason the EVI2 did not improve upon cross-sensor relationships between SPOT-VGT and MODIS, was partly due to this insensitivity to blue band variations. Another reason was that the blue-red cross-band relationships were somewhat weaker than other sensors.

The MAD between sensor and MODIS EVI2 was highest at AVHRR sensor, with least differences over VIIRS sensor (Table 2-2). In other words, VIIRS has the best

continuity to MODIS sensor and AVHRR has the worst stability through reflectance and VIs deviation analyses, and MAD analyses. To make consistency and continuity with the AVHRR VI as well as red and NIR reflectance, some sensor translation equations would be required. RMSE derived from the convolved and the converted EVI2 showed the MODIS, VIIRS and SeaWiFS had the better EVI2 translation equation than SPOT-VGT (Table 2-2).

This was a hyperspectral simulation study. If we use actual satellite datasets, the result could be different from this work. The comparison using actual satellite over various land covers should be required later.

IV. Multisensor reflectance and vegetation index comparisons of Amazon tropical forest phenology with hyperspectral Hyperion data

1. INTRODUCTION

Vegetation indices have been used in many scientific applications to derive vegetation biophysical properties, such as biomass, leaf area index (LAI), fraction of absorbed photosynthetic active radiation (fAPAR), and phenology (Running et al. 2004, Gao et al. 2000, Field et al 1995, Sellers et al. 1985, Asrar et al. 1984, and Tucker 1979), and estimate their net, or combined properties, which have been related to climate change (Coops et al. 2007, Heinsch et al. 2006, and Schloss et al. 1999). In particular, alterations in the timing and length of the growing season have been found with vegetation phenological information using the AVHRR remote sensing data (Myneni et al., 1997).

Phenology studies can contribute to investigations of climate change. Identifying temporal stages of growth are important in seasonal characterization of canopies. Changes in phenology from year to year may be indicators of climatic variations and provide signs of terrestrial carbon cycle perturbations due to global warming. Saleska et al. (2003) found phenological patterns that corresponded to the seasonal dynamics of net carbon dioxide exchange in rainforest areas. Observing seasonal cycles with field-based measurements are very difficult and limited spatially and temporally. Today globally available remote sensing data with a high repeat cycle is generally accepted as a means for evaluating phenological characteristics of vegetated areas and in assessing their variability over large areas (Xiao et al. 2006, Zhang et al. 2003, and Reed et al. 1994). Recent studies have shown close relationships between MODIS or AVHRR and the flux

tower datasets (Wilson et al. 2007, Hill et al. 2006, Wang et al. 2004, and Huemmrich et al. 1999).

In particular, remote sensing has been extensively used to monitor vegetation phenology with long-term time series data records (Xiao et al. 2006 and Sakamoto et al. 2005). Its synoptic coverage and the repeated temporal sampling from satellite observations have provided a significant potential in assessing phenological dynamics. A number of different methods have been developed to determine the timing of vegetation green-up and senescence using the time series of NDVI from the Advanced Very High Resolution Radiometer (AVHRR) and Moderate Resolution Imaging Spectroradiometer (MODIS) (Sakamoto et al. 2005, Kang et al. 2003, Zhang et al. 2003 and 2001).

Recent cross-sensor studies have shown the possibilities to translate the old sensors to new and advanced sensors, such as MODIS, SPOT-VEGETATION (VGT), and Sea-viewing Wide Field-of-view Sensor (SeaWiFS), in order to extend the existing historical NDVI data record (Tucker et al. 2005). In addition to NDVI, the Enhanced Vegetation Index (EVI) has been used to extract biophysical information (e.g. Gross Primary Production and phenology information) (Huete et al. 2006a, b). Despite the strength of the remote sensing phenology, some noise and artifacts occur in the atmosphere and in the sensor itself, such as sun/view angle geometry, the bidirectional reflectance distribution function (BRDF) of different land cover types, aerosols, and unreliable calibration among sensors, resulting in complex translations among sensors.

The seasonal variations of the AVHRR NDVI in the tropical forests of the Amazon are predominantly associated with the atmospheric CO₂ record collected by the Climate

Monitoring and Diagnostics Laboratory (CMDL), and lower troposphere temperature anomalies detected by microwave sounding unit (Braswell et al. 1997), solar radiation (Xiao et al. 2006), aerosols and clouds (Kobayashi et al. 2005). In this study, hyperspectral simulations with Hyperion data containing a near nadir view angle and the constant sun/view angle differences were studied over Amazon rainforests. The differences from the simulations among sensors were mostly attributed to their spectral response function, land cover type, phenology, and atmospheric correction schemes. An analysis of inter-sensor translation with respect to phenological stages has not yet been made. This is the focus of this chapter. The potential extension of vegetation indices derived from this study would be useful to understand tropical forest phenology, to generate consistent and objective estimates of phenology, and to evaluate phenological influences on inter-sensor transforms.

The objectives of this study were,

- (1) Investigation of the variation of inter-sensor translation equations of blue, red, NIR reflectances and VI's (NDVI, EVI, and EVI2) between MODIS and the other sensors during periods of maximum phenologic activity,
- (2) Evaluation of the interactions and influences of phenology (stage of greenness) on inter-sensor translation and continuity relationships.

2. METHODOLOGY

The 5 hyperspectral Hyperion data (Fig. 3-1) was convolved spectrally into Terra MODIS, NOAA-14 AVHRR, NPOESS VIIRS, SPOT-VGT, and SeaWiFS bandpasses at the top of atmosphere, using sensor-specific spectral response functions (Fig. 1-1). Finally, the convolved multispectral images were atmospherically corrected with '6S' to derive spectral reflectances at the top of the canopy (TOC). Aerosol and optical depth parameters were derived from the AERONET sun photometer network for visibility estimation (http://aeronet.gsfc.nasa.gov/data_frame.html) at the Belterra site (Lat. 2.647 S., Long. 54.952 W.) (Holben et al. 1998).

We examined the optical- phenology characteristics from the Tapajos National Forest, which is predicted to become drier with climate change (Cox et al. 2000), and the surrounding areas, south of Santarem in the state of Para, Brazil, with a temporal sequence of six Hyperion images acquired during the 2001 and 2002 dry seasons (July to December) periods (Fig. 3-1, left). Spatially overlapped and registered images were chosen from 5 different dates to extract the same pixels geographically (Fig. 3-1, right). A transect was made, consisting mostly of the undisturbed, dense tropical evergreen broadleaf rainforest (primary forest), and disturbed and converted forest areas (secondary forest and agricultural site) using field survey and visual estimation. The mean annual precipitation ranged from 1900 to 2300 mm during the dry season (< 100 mm; Saleska et al. 2003) period of ~5 months from early July through early December (Huete et al. 2007).

In this study, we evaluated the use and extension of the new 2-band EVI to other sensor systems. We also compared the 2-band EVI equation (without the blue band) with

the normal EVI equation (with the blue band) to assess their cross-equation compatibility. The influence and interactions of phenology on the translations among sensors were evaluated. NDVI and two EVIs take the form,

$$NDVI = \frac{\rho_{NIR} - \rho_{Red}}{\rho_{NIR} + \rho_{Red}} \quad [1]$$

$$EVI \text{ or } 2\text{-BandEVI} = G \times \frac{\rho_{NIR} - \rho_{Red}}{L + \rho_{NIR} + C_1 \times \rho_{Red} - C_2 \times \rho_{Blue}} \quad [2]$$

Where ρ is atmospherically corrected surface reflectances, L is the soil background adjustment factor and C_1 , C_2 are the coefficients of the aerosol resistance term for aerosol influences in the red and blue bands. The coefficients used are, $L=1$, $C_1=6$, $C_2 = 7.5$, and G (gain factor) = 2.5 (Huete, 1997). For 2-band EVI (hereafter EVI2), the coefficients are $L=1$, $C_1=2.4$, $C_2=0$, and $G = 2.5$ (Jiang et al., 2007, submitted).

The mean absolute difference (MAD) between variables from the two sensors was also computed as an overall quantitative measure of sensor differences,

$$MAD = \frac{\sum_{i=1}^n |X1_i - X2_i|}{n} \quad [3]$$

where $X1$ = reflectances or VIs of sensor X1, and $X2$ = MODIS reflectances or VIs.

3. RESULTS

3.1 The phenologic patterns with the convolved sensor vegetation indices

Three land cover types along transect by field survey and visual estimation (Fig. 3-1) were selected from the convolved Hyperion data, which showed discrimination among

primary forest, secondary forest (regenerating forest), and agricultural (forest conversion) areas due to finer spatial resolution. Uncontaminated and unmixed pixels with different neighboring land covers were extracted and averaged (24 pixels in agricultural site, 50 pixels in primary forest, and 139 pixels in secondary forest in the transect line) to see the phenological patterns.

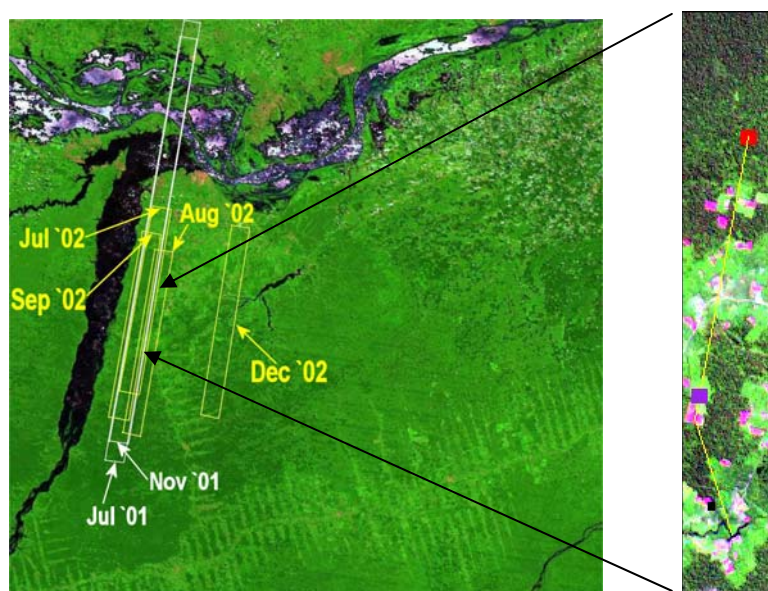


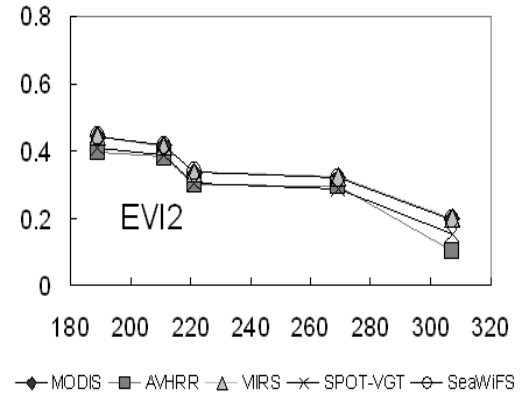
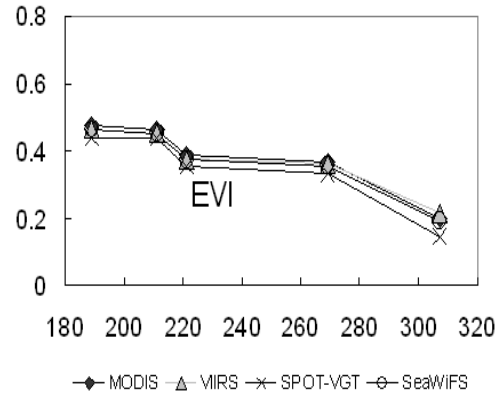
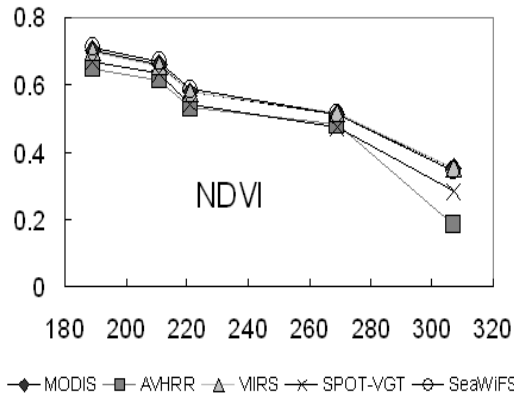
Figure 3-1. Location of 6 EO-1 Hyperion scene acquisitions within Tapajos National Forest and surrounding areas, south of Santarem, Para, Brazil; each Hyperion is 11 km wide. Right is transect (yellow line) from overlapped Hyperion image (red rectangle on top: primary forest, purple rectangle on middle: secondary forest, and black rectangle on bottom: agricultural site).

The sensor NDVI, EVI and EVI2 averages over secondary forests slightly decreased, and then increased in the 2002 season. Sensor EVI averages increased in the primary forest in the 2001 and 2002 dry seasons, while sensor NDVI decreased in the 2001 and 2002 dry seasons. Sensor EVI2 in the primary forest in 2002 decreased slightly and then

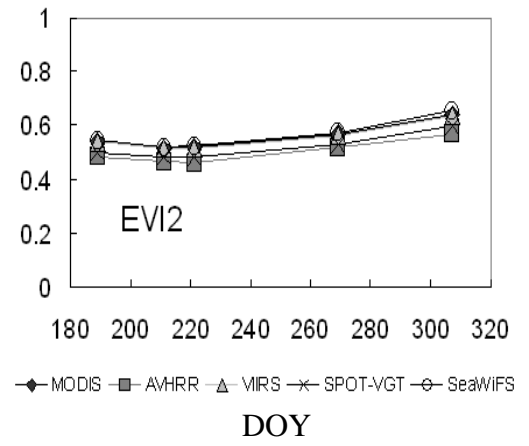
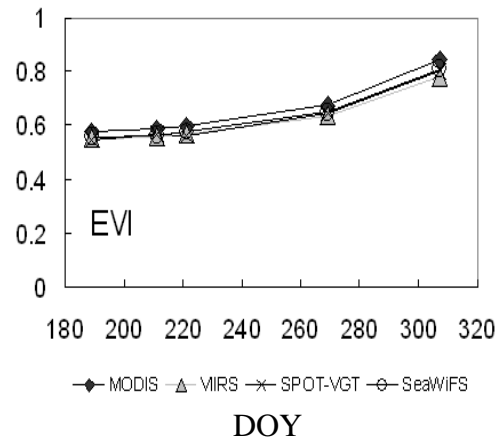
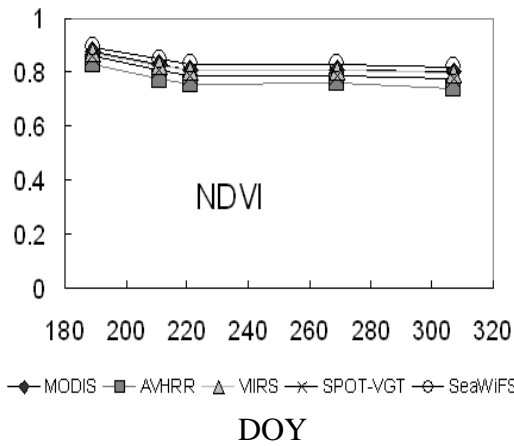
increased. Sensor NDVI, EVI, and EVI2 averages decreased in the agricultural sites during the 2001 and 2002 dry seasons (Fig. 3-2). Sensor EVI and EVI2 averages were mostly less than sensor NDVI average across all three land covers, except for sensor EVI in the primary and secondary forest sites in 2001, DOY 307. As expected, the AVHRR NDVI and EVI2 averages were less than the other sensor NDVI and EVI2 averages. The SeaWiFS NDVI average had the greatest value across all three land covers during the 2001 and 2002 dry seasons (Fig. 3-2).

Sensor NDVI averages decreased by ~10% from the beginning (July: DOY 189) to the end of the dry season (November: DOY 307) in the primary and secondary forest sites (~40% difference in agricultural site), which was opposite that sensor EVI and EVI2 averages found in the primary and secondary forest which increased by 25% and 10%, respectively. The sensor EVI and EVI2 averages in the agricultural site decreased by ~25%.

The EVI in secondary forest displayed a senescence in the first half of the dry season followed by a reversal with greening in the second half of the dry season. Previous studies with the MODIS also found EVI values to peak in the late dry season and not saturated in Amazon tropical rainforest (Huete et al. 2007 and Huete et al. 2006b).

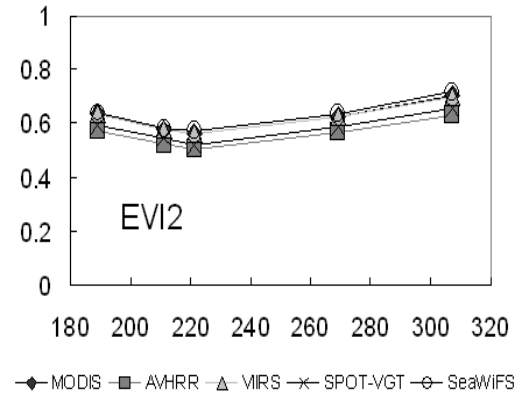
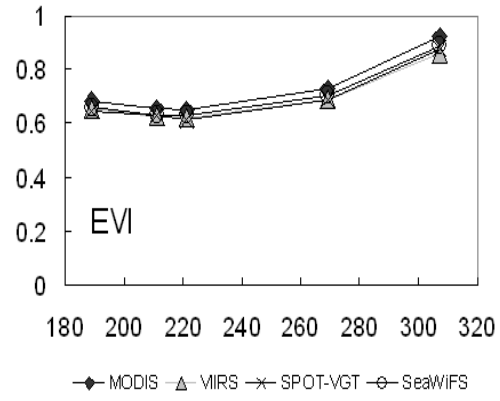
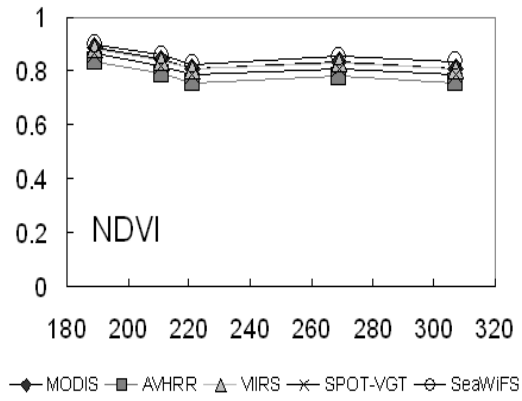


(a)



(b)

Figure 3-2 VIs variations for 5 phenology stages ((a) Agricultural site, (b) Primary Forest, and (c) Secondary Forest)



(c)

Figure 3-2 (continued).

3.2 Inter-sensor translations of sensor reflectances during dry seasons

In order to simplify the comparisons, we selected three time periods during the dry seasons: the early (wet), mid, and late- dry seasons (July, September and November) with all three land covers from 5 EO-1 Hyperion scenes (Fig. 3-1). In order to investigate the variations of the relationship between sensor and the MODIS reflectances (blue, red, and NIR reflectances) with respect to the phenology and sensor-type, the sensor versus MODIS reflectances were plotted with all three land covers and inter-sensor translation equations were also provided on the plots (Fig. 3-3, 3-4, 3-5).

The MODIS blue reflectances were linearly correlated with the sensor blue reflectances. The largest blue reflectance values were found on DOY 307 (the smallest values on DOY 189). SPOT-VGT blue reflectances were strongly correlated with the MODIS blue reflectances on DOY 221 ($R^2=0.9874$) with a slope of 0.9714 (Fig. 3-3b), as was expected from their similar spectral response functions (Fig. 1-1). The VIIRS and SeaWiFS blue reflectances were the least, although strong, correlated with MODIS blue reflectances ($R^2=0.926 - 0.929$), but with slopes that deviated the most from the 1:1 line (slopes of 1.1 - 1.2) (Fig. 3-3a, c). Overall, VIIRS and SeaWiFS blue reflectances were mostly below the 1:1 line, while SPOT-VGT blue reflectances were higher, or above the 1:1 line.

Most linear coefficient of determination values in the red band exceeded $R^2>0.991$, with slopes between 0.98 and 1.1, with the exception of the weaker AVHRR red reflectance relationships, $R^2= 0.971 - 0.990$, and a slope of 0.918 - 1.011 (Fig. 3-4). The AVHRR red reflectances were mostly larger than the MODIS red reflectances. The

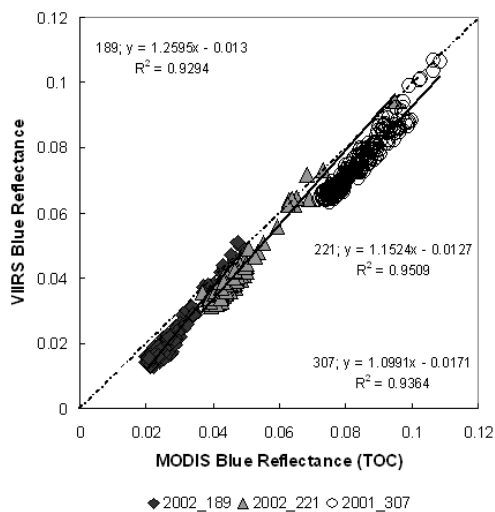
VIIRS, SPOT-VGT, and SeaWiFS red reflectances showed strong agreements with the MODIS red reflectances in all three dates, but there were some differences in SeaWiFS red reflectances on the DOY 307 (Fig. 3-4).

The VIIRS, SPOT-VGT, and SeaWiFS relationships with MODIS in the NIR reflectances were very strong with R^2 values exceeding 0.999, except in the case of AVHRR where the R^2 was between 0.992 and 0.996 (Fig. 3-5). The slopes of the cross-sensor NIR relationships were also lowest for the AVHRR (slope of 0.88 on DOY 307), resulting in a 12% negative bias attributed to the very wide AVHRR NIR bandpass (Fig. 1-1). Overall, the VIIRS and SeaWiFS NIR reflectances were mostly close to 1:1 line, while AVHRR and SPOT-VGT NIR reflectances became less with increasing MODIS NIR reflectances during the dry seasons.

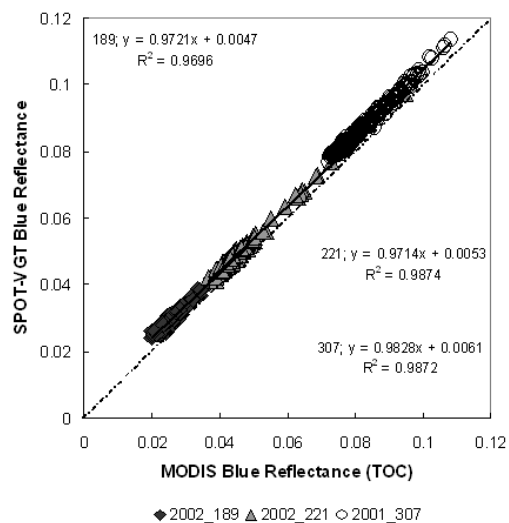
3.3 Sensor reflectance deviations per land cover during dry seasons

Sensor deviations from MODIS NDVI, EVI, and EVI2 were compared with those from VIIRS, AVHRR, SPOT-VGT, and SeaWiFS and were investigated in terms of their absolute differences with the pixels on the transect line, in order to figure out the VI continuity issue to MODIS VIs regarding phenology and land cover per each sensor (Fig. 3-6, 3-7, 3-8, and 3-9).

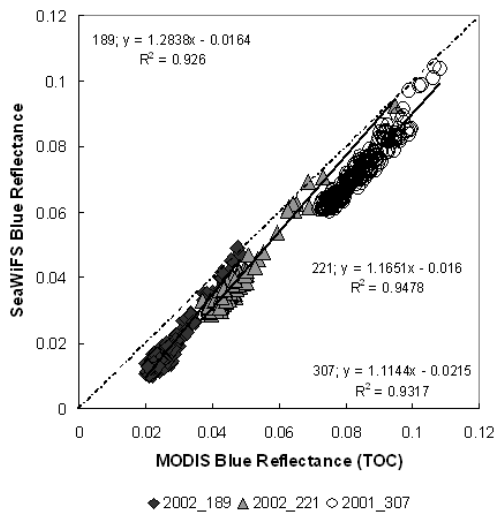
Fig. 3-6 displayed VIIRS VI deviations from MODIS values per land covers during the 3-stage dry season. The VI deviations between VIIRS and MODIS were mostly within -0.08 and 0.01, with the EVI resulting in the greatest deviations, and EVI2 resulted in the least deviations. In agricultural and pasture sites, the VIIRS vegetation indices



(a)



(b)



(c)

Figure 3-3. Crossplot of sensor and MODIS blue reflectance with all three land covers ((a) VIIRS, (b) SPOT-VGT, and (c) SeaWiFS).

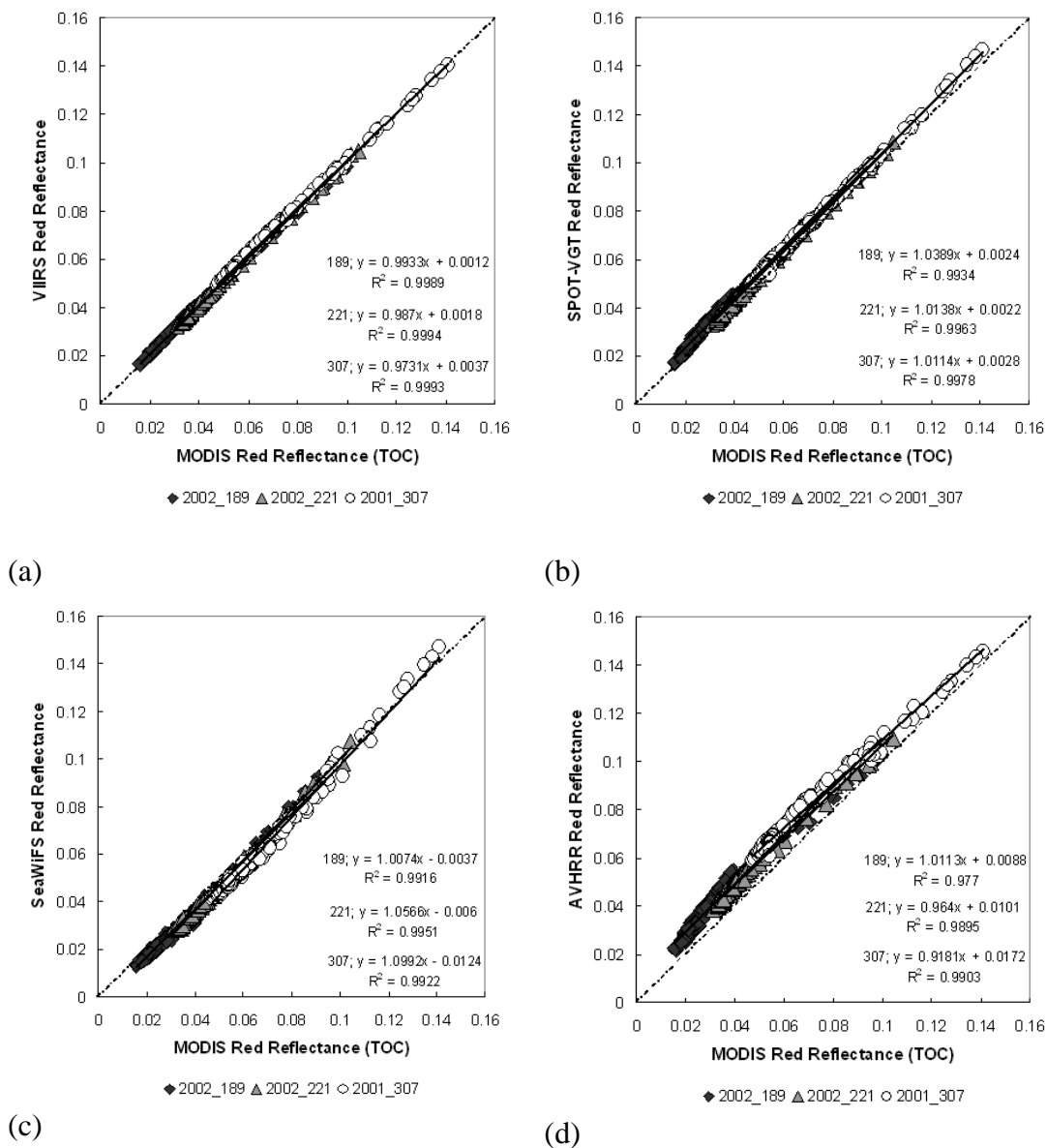


Figure 3-4. Crossplot of sensor and MODIS Red reflectance with all three land covers ((a) VIIRS, (b) SPOT-VGT, (c) SeaWiFS, and (d) AVHRR).

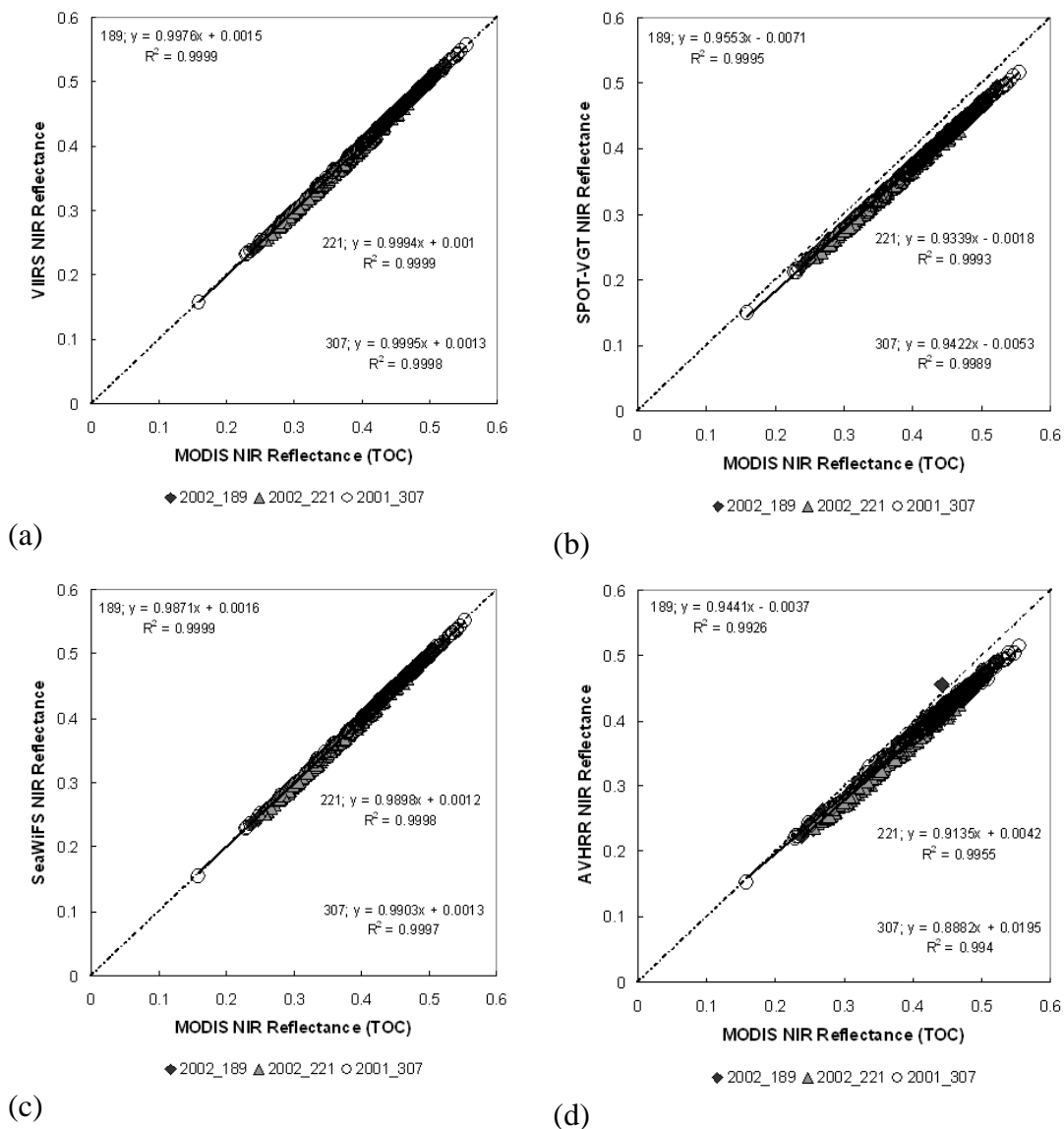


Figure 3-5. Crossplot of sensor and MODIS NIR reflectance with all three land covers ((a) VIIRS, (b) SPOT-VGT, (c) SeaWiFS, and (d) AVHRR).

deviations became negative with increasing MODIS VI values (Fig. 3-6a). The lower MODIS VI (<0.4) had partially positive VI's deviations as did the VI's deviations in the agricultural sites. It depicted that the more vegetated area resulted in negative VI deviations. VIIRS NDVI and EVI2 were uniformly deviated with negative offset (~ -0.01) in the primary forest site, while there was distinct separation in the VIIRS EVI deviation in the primary forest site (Fig. 3-6b). In the late-dry season (DOY 307), the VIIRS EVI deviations were larger than in the other two seasons (early- and mid-dry) in the primary forest site. The VIIRS EVI on DOY 307 in primary forest site ranged within -0.04 and -0.08 , while their values for VIIRS EVI on DOY 189 and 221 were zero and -0.04 in the primary forest site. Fig. 3-6c showed a wide range ($0.2 - 0.9$) of MODIS VI values in secondary forest area. In VIIRS NDVI and EVI2 the deviations became negative with increasing MODIS NDVI and EVI2 as VIIRS NDVI and EVI2 deviations in the primary forest region. There were two VIIRS EVI separations in the secondary forest in the late-dry season, similar to the deviations in the primary forest, but the VIIRS EVI deviations in the secondary forest were mostly negative and extended to zero values, in contrast to the VIIRS EVI differences in the primary forest. The VIIRS NDVI and EVI2 constantly deviated with an offset of -0.01 and $+0.01$ in all three land covers, while VIIRS EVI deviations became negative up to -0.08 in the late dry season (-0.04 in early- and mid-dry seasons) in all three land covers. The VIIRS EVI showed that the deviations mostly larger in the late dry season in all three land covers.

The AVHRR showed the largest deviations from the MODIS in both NDVI and EVI2 on different dates and land covers up to -0.08 (Fig. 3-7). AVHRR NDVI differences were

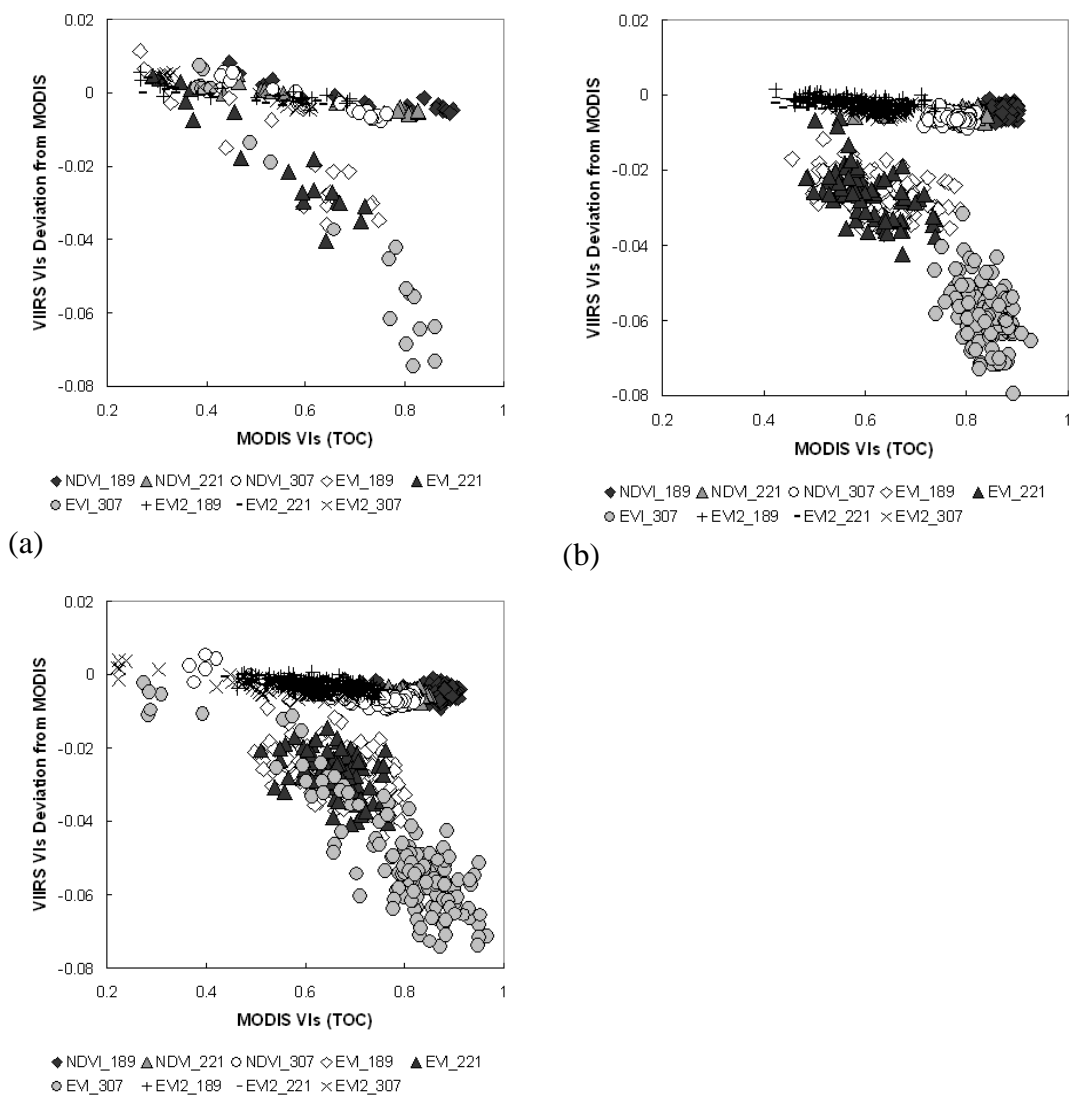
complex with a V-shaped curvilinear relationship pattern with increasing MODIS NDVI, particularly evident in all three of the land covers (Fig. 3-7), while the EVI2 deviations linearly decreased with increasing MODIS EVI2 over all three of the land covers (Fig. 3-7). The EVI2 translations between MODIS and AVHRR describes more straightforward than the NDVI transforms.

The NDVI and EVI deviations over the three land covers between the SPOT-VGT and MODIS sensors were negative and more complicated with a less V-shaped curvilinear relationship pattern with increasing MODIS values than AVHRR (Fig. 3-8). The SPOT-VGT EVI2 deviations tended to be concentrated at around SPOT-VGT deviation of -0.04 and ranged from -0.06 to -0.02 in all three cover types.

EVI deviations between the SeaWiFS and MODIS resembled those between VIIRS and MODIS EVI (Fig. 3-9), but SeaWiFS NDVI and EVI2 differences were much larger and became positive with increasing MODIS NDVI and EVI2 as a result of the lower red reflectance values in SeaWiFS (Fig. 3-4c). SeaWiFS EVI deviations were negatively biased, as in the VIIRS case, a result of the VIIRS and SeaWiFS having similar blue bands.

3.4 Variations of inter sensor translations on temporal and spatial changes

Inter-sensor translation equations with the pixels on the transect were calculated using linear regression lines with MODIS values as a reference (x-axis) for each land cover during the three dry periods, in order to investigate the influence of phenological variations on inter-sensor transforms of sensor reflectances and vegetation indices. The



(c)
Figure 3-6. VIIRS VIs deviations from MODIS value ((a) Agricultural site, (b) Primary Forest, and (c) Secondary Forest).

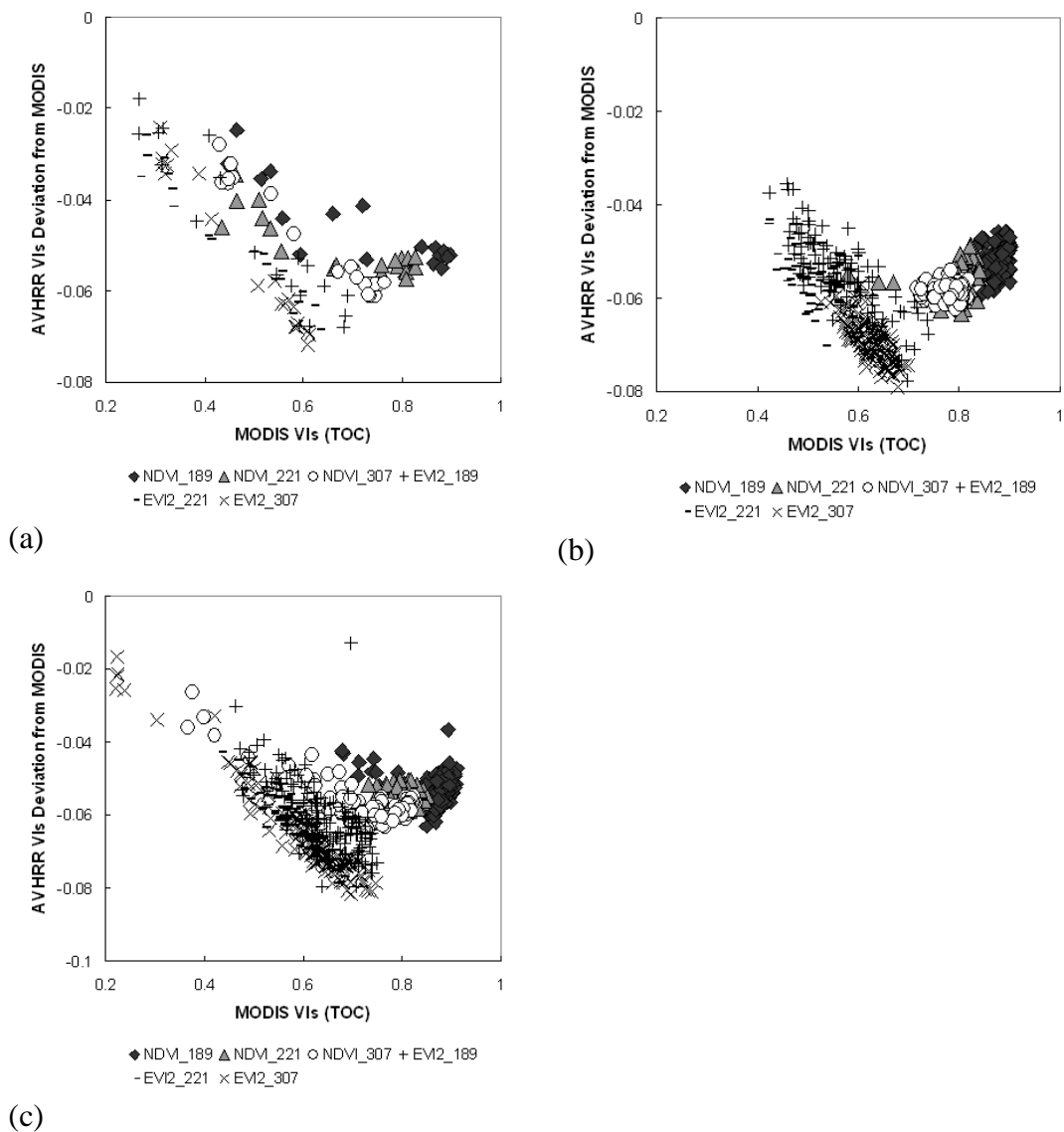
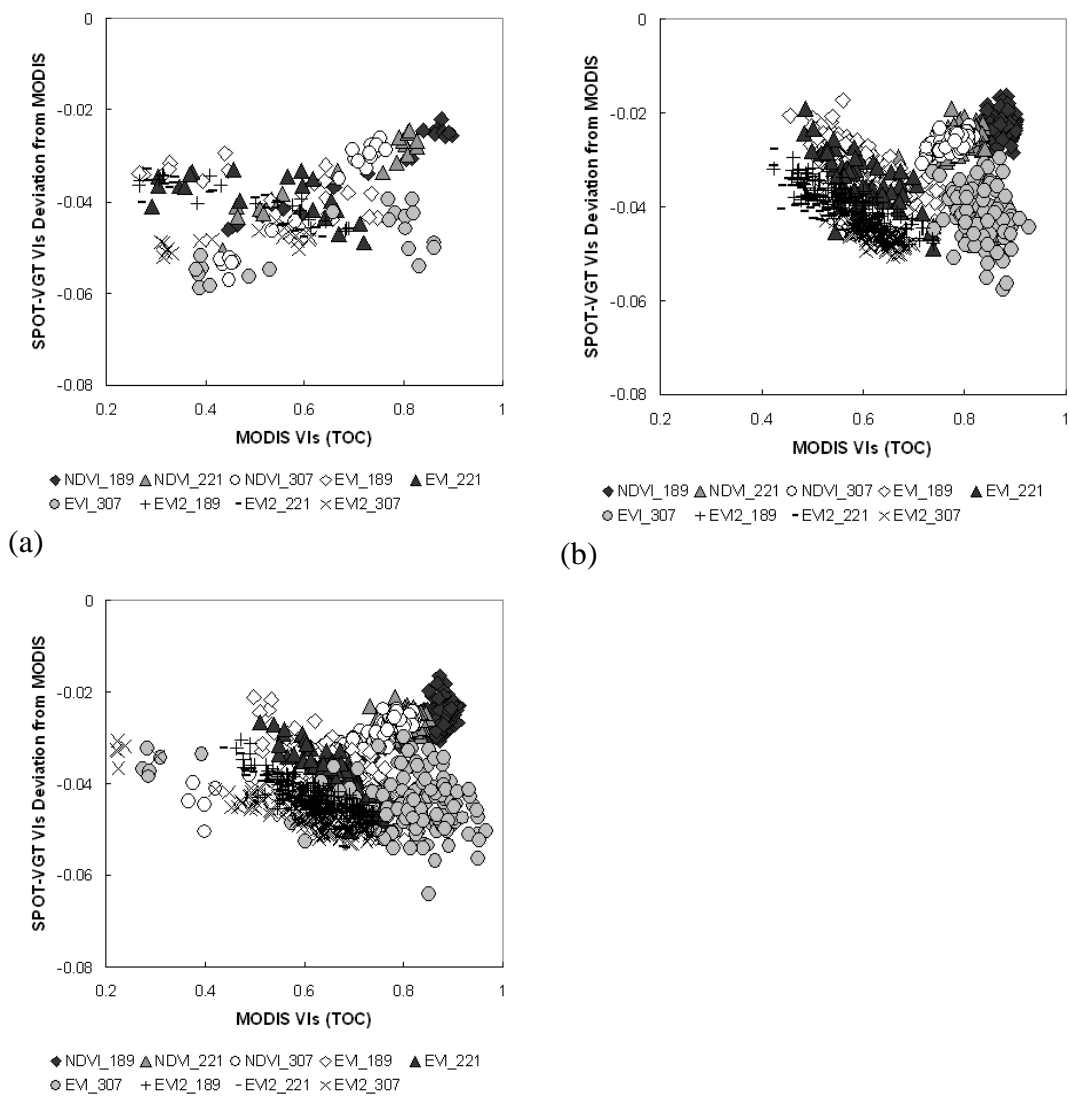
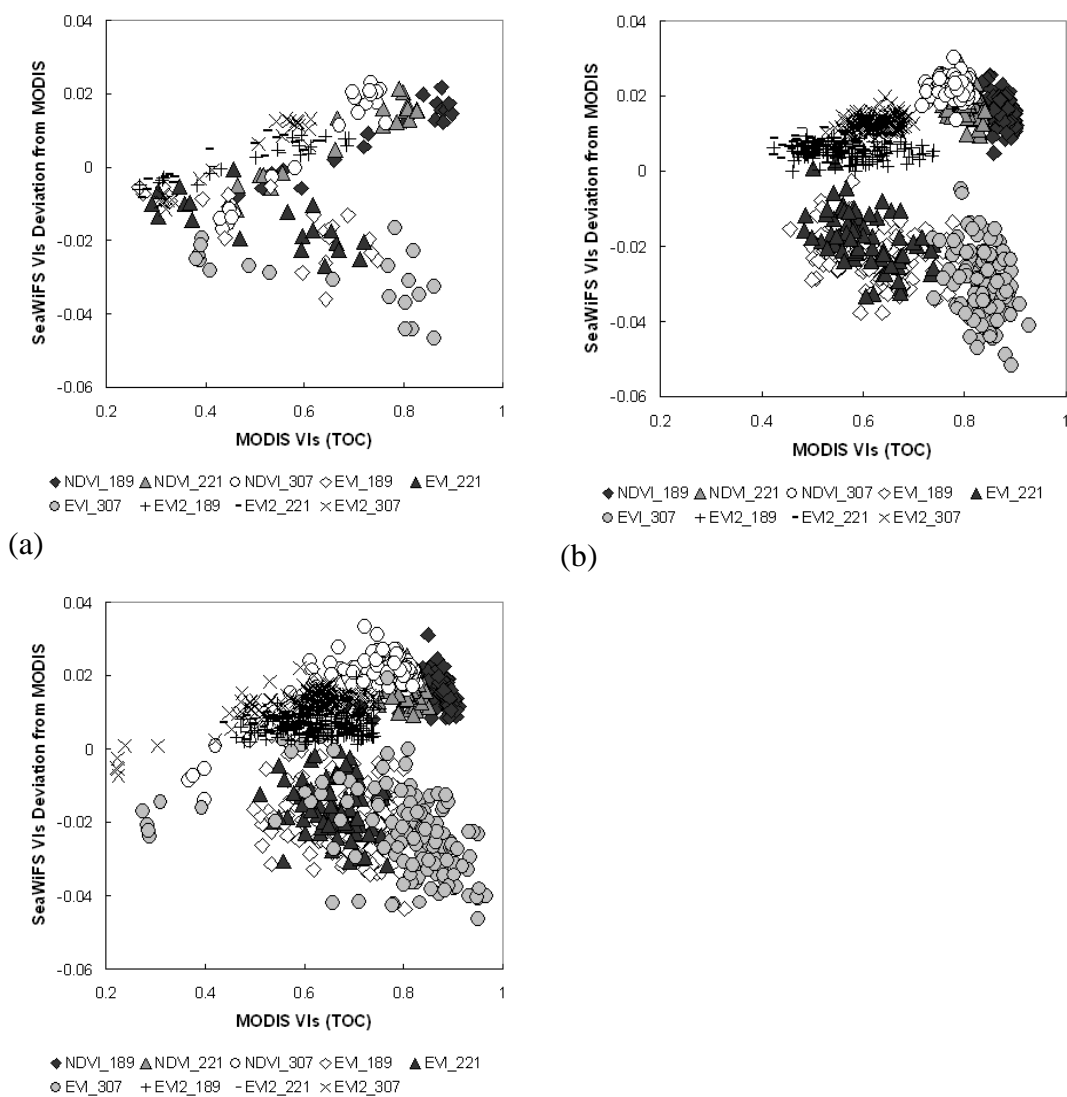


Figure 3-7. AVHRR VIs deviations from MODIS value ((a) Agricultural site, (b) Primary Forest, and (c) Secondary Forest).



(c)
 Figure 3-8. SPOT-VGT VIs deviations from MODIS values ((a) Agricultural site, (b) Primary Forest, and (c) Secondary Forest).



(c)
Figure 3-9. SeaWiFS VIs deviations from MODIS value ((a) Agricultural site, (b) Primary Forest, and (c) Secondary Forest).

slopes of cross-sensor translation equations of the blue, red, NIR bands, and the vegetation indices (NDVI, EVI, and EVI2) were compared with MODIS equivalent bands and vegetation indices. The slope variations formed strong and linear cross-sensor relationships for the blue, red, NIR bands and vegetation indices during the three seasons for each land cover type (Fig. 3-10). However, in some cases, there were differences in the slopes of the regression relationship with respect to the seasons and land cover, particularly for the blue reflectances (Table 3-1 and Fig. 3-10).

RMSE between the transformed and the convolved sensor value per each dry season is provided in Table 3-1. The inter-sensor transform between VIIRS/SPOT-VGT/SeaWiFS and MODIS has the largest RMSE for EVI in the late dry season, while inter-sensor translation equation between VIIRS/SPOT-VGT/SeaWiFS and MODIS has the highest RMSE for the NDVI in the early dry season. RMSE for the VIIRS and SPOT-VGT EVI2 in the early dry season was less than RMSE for the VIIRS and SPOT-VGT EVI2 in the late dry season, however, RMSE for the AVHRR and SeaWiFS EVI2 in the early dry season was more than RMSE for the AVHRR and SeaWiFS EVI2 in the late dry season.

There were slope variations of the translation equations of reflectances and vegetation indices between VIIRS and MODIS regarding different seasons and land covers (Fig. 3-10a). The slopes of the translation equations of the blue reflectance and EVI showed wide differences with respect to various seasons and land covers, especially in the agricultural sites. The variations in slope of the translation equations of EVI were not constant and mostly less than a slope of one (Fig. 3-10a), resulting from the large

Table 3-1. Inter sensor translation equations with MODIS using linear regression lines across early-, mid-, and late-dry season at the combined three land covers (Agricultural, Primary forest, and secondary forest)

Sensor			VIIRS			AVHRR		
			189	221	307	189	221	307
MODIS	NDVI	Slope	0.9824	0.9827	0.9757	0.9652	0.9721	0.9413
		Intercept	0.0106	0.0087	0.0121	-0.022	-0.0329	-0.0133
		R-Square	0.9995	0.9997	0.9997	0.9966	0.9977	0.9986
		RMSE**	0.0014	0.0009	0.0013	0.0037	0.0026	0.0029
	EVI	Slope	0.9467	0.9318	0.8884			
		Intercept	0.0084	0.0169	0.0367			
		R-Square	0.9953	0.9945	0.9948			
		RMSE**	0.0063	0.0049	0.0079			
	EVI2	Slope	0.9874	0.9902	0.9837	0.9077	0.9038	0.8816
		Intercept	0.0055	0.0032	0.0062	-0.0019	-0.0064	0.0053
		R-Square	0.9998	0.9998	0.9998	0.9941	0.9965	0.9983
		RMSE**	0.0012	0.0008	0.0013	0.0063	0.0033	0.0034

Sensor			SPOT-VGT			SeaWiFS		
			189	221	307	189	221	307
MODIS	NDVI	Slope	1.0529	1.0461	1.0586	1.0376	1.0571	1.0724
		Intercept	-0.0705	-0.0633	-0.0727	-0.0172	-0.0294	-0.0344
		R-Square	0.9984	0.9989	0.9993	0.9958	0.9971	0.9977
		RMSE**	0.0028	0.0020	0.0023	0.0044	0.0032	0.0043
	EVI	Slope	0.9551	0.9635	1.0007	0.9804	0.9716	0.9683
		Intercept	-0.0071	-0.0146	-0.0443	-0.0073	0.0011	-0.0007
		R-Square	0.9973	0.9969	0.9976	0.992	0.9932	0.9922
		RMSE**	0.0047	0.0037	0.0060	0.0085	0.0056	0.0393
	EVI2	Slope	0.9578	0.9533	0.9792	1.0127	1.0206	1.0405
		Intercept	-0.0158	-0.0165	-0.0339	-0.0023	-0.0047	-0.0126
		R-Square	0.9992	0.9988	0.9991	0.9991	0.9990	0.9989
		RMSE**	0.0024	0.0020	0.0027	0.0037	0.0020	0.0031

**root mean square error (RMSE) from the transformed sensor value and the convolved sensor value

discrepancies of the blue reflectances between the VIIRS and MODIS (Fig. 3-3c). The translation equations of red, NIR, NDVI, and EVI2 did not deviate much from a slope of one, with nearly constant variations during the 3-stage seasonal time sequence (Fig. 3-10a). This was a result of the similarities in the spectral response functions between the red and NIR bands of both sensors.

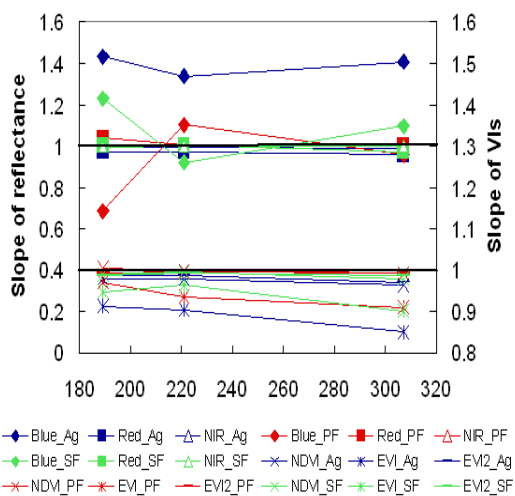
In Fig. 3-10b, the comparison of slope changes of the translation equations of the AVHRR red, NIR, NDVI, and EVI2 with MODIS are provided. The slope of the translation equations of AVHRR red reflectance varied significantly in the primary forest region, particularly on DOY 189 with a slope of 1.3. Mostly, the slope change of the translation equations of AVHRR NDVI was uniform and distributed around a slope of one, with an offset of 0.08, while that of the translation equations of AVHRR EVI2 was less than a slope of one. The slope variations of translation equations of AVHRR NDVI and EVI2 tend to follow those of the translation equations of AVHRR red and NIR reflectance, respectively.

The slope changes of the translation equations of red reflectance in SPOT-VGT were similar to that of the translation equations of red reflectance in AVHRR (Fig. 3-10c). The slope variations of translation equations of SPOT-VGT NIR reflectance were mostly less than the slope of one and uniform with an offset of around 0.05. In contrast to the VIIRS blue reflectance, the slope change of the translation equations of the SPOT-VGT blue reflectance was nearly constant due to the similarities to the MODIS blue band, except for the early-dry season (DOY 189) in the primary forest, resulting in the slope variations of translation equations of SPOT-VGT EVI also consistent with values

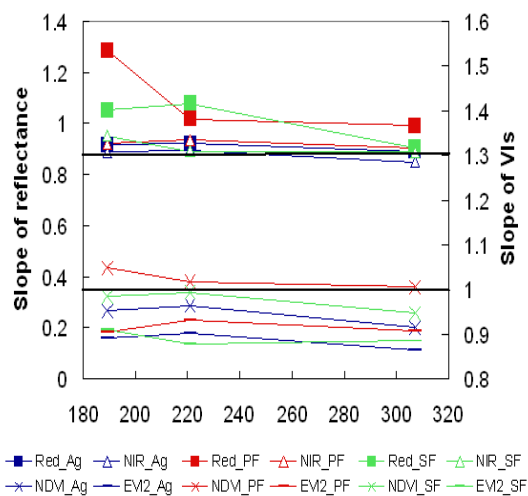
less than slope of one. The SPOT-VGT NDVI slope change was more than slope of one and its variation was mostly uniform, while SPOT-VGT EVI2 slope variations were less than slope of one and its pattern was similar to the SPOT-VGT NIR slope changes.

The slope change of translation equations of SeaWiFS blue reflectance was similar to that of translation equations of VIIRS blue reflectance, while the slope variation of translation equations of SeaWiFS red reflectance was slightly different from VIIRS red reflectance, resulting in a scattered distribution of the slope of SeaWiFS NDVI over the seasons and land covers (Fig. 3-10d). In the case of SPOT-VGT EVI2, the slope change of translation equations of SeaWiFS EVI2 tended to go behind SeaWiFS NDVI slope variations with respect to seasons and land covers, even though constant SeaWiFS NIR slope change.

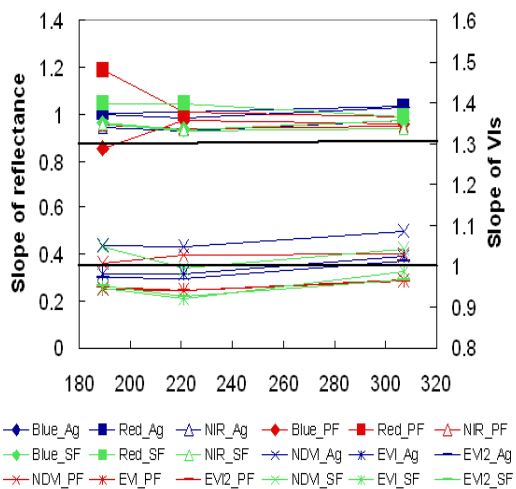
In Fig. 3-11, as an overall quantitative measure of sensor differences ([3]), MAD of vegetation indices between VIIRS and MODIS were analyzed, to examine if the phenology patterns found in the convolved Hyperion data could have an effect on cross sensor translation equations between sensor and MODIS vegetation indices. The MAD of VIIRS and MODIS vegetation indices showed good agreements in NDVI and EVI2, with large differences in EVI (0.015 to 0.06), resulting in the greatest deviations in the late-dry season (primary forest), but resulting in the least EVI2 deviations among all three land covers (Fig. 3-11a). The MAD changes in VIIRS NDVI and EVI2 were mostly negative and increased from early- to late-dry season in the primary and secondary forest, however, the MAD was nearly constant in the VIIRS NDVI and EVI2 variations at the agricultural site.



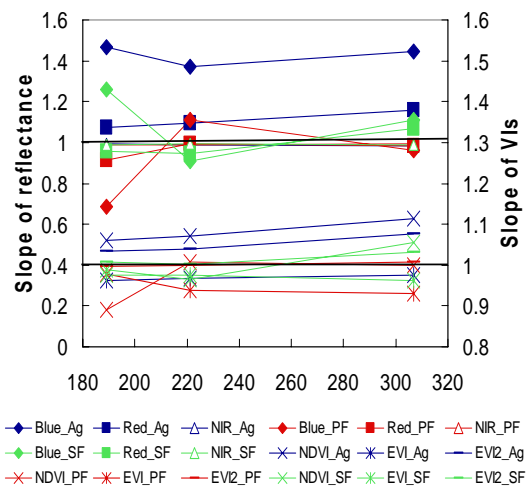
(a)



(b)



(c)



(d)

Figure 3-10. Slope variations of cross sensor translation equations of reflectance and VIs between sensor and MODIS regarding three periods (early-, mid-, and late- dry seasons) and land covers (Agricultural site, Primary forest, and secondary forest) ((a) VIIRS, (b) AVHRR, (c) SPOT-VGT, and (d) SeaWiFS).

In the AVHRR sensor data, the MAD of vegetation indices was more negative than that of the other sensors, with an overall differences in a range between 0.047 and 0.07 (Fig. 3-11b), because this was the widest bandpass in both the red and NIR bands. The MAD of AVHRR NDVI and EVI2 deviated most from the MODIS was found in the AVHRR EVI2 in the primary forest (DOY 307), while MAD of AVHRR NDVI and EVI2 were least deviated from MODIS in the agricultural site (DOY 189). There were increases of MAD of NDVI and EVI2 in AVHRR across all three of the land covers as it approached the late-dry season.

The MAD of SPOT-VGT NDVI and EVI2 relative to MODIS were generally larger than the MAD between the VIIRS and MODIS, except for EVI (Fig. 3-11c). It ranged from 0.02 to 0.05. The largest deviation was located on SPOT-VGT EVI in the agricultural site (DOY 307), but the least bias was found in the SPOT-VGT NDVI variation in the primary forest (DOY 189). The MAD variations in SPOT-VGT EVI showed similar patterns to those in SPOT-VGT EVI2 and, in late-dry season, there were sharp increases in both SPOT-VGT EVI and EVI2.

The ranges of the SeaWiFS NDVI and EVI2 MAD were from 0.002 to 0.03 (Fig. 3-11d). Similar to SPOT-VGT, the largest difference was discovered in SeaWiFS EVI in the agricultural site (DOY 307) and the least deviation was found in SeaWiFS EVI2 in the agricultural site (DOY 189). The NDVI and EVI2 MAD of SeaWiFS and MODIS were increased from early- to late-dry season in the primary and secondary forest, as same as shown by the other sensors. There was a sharp decreased in the MAD of the SeaWiFS

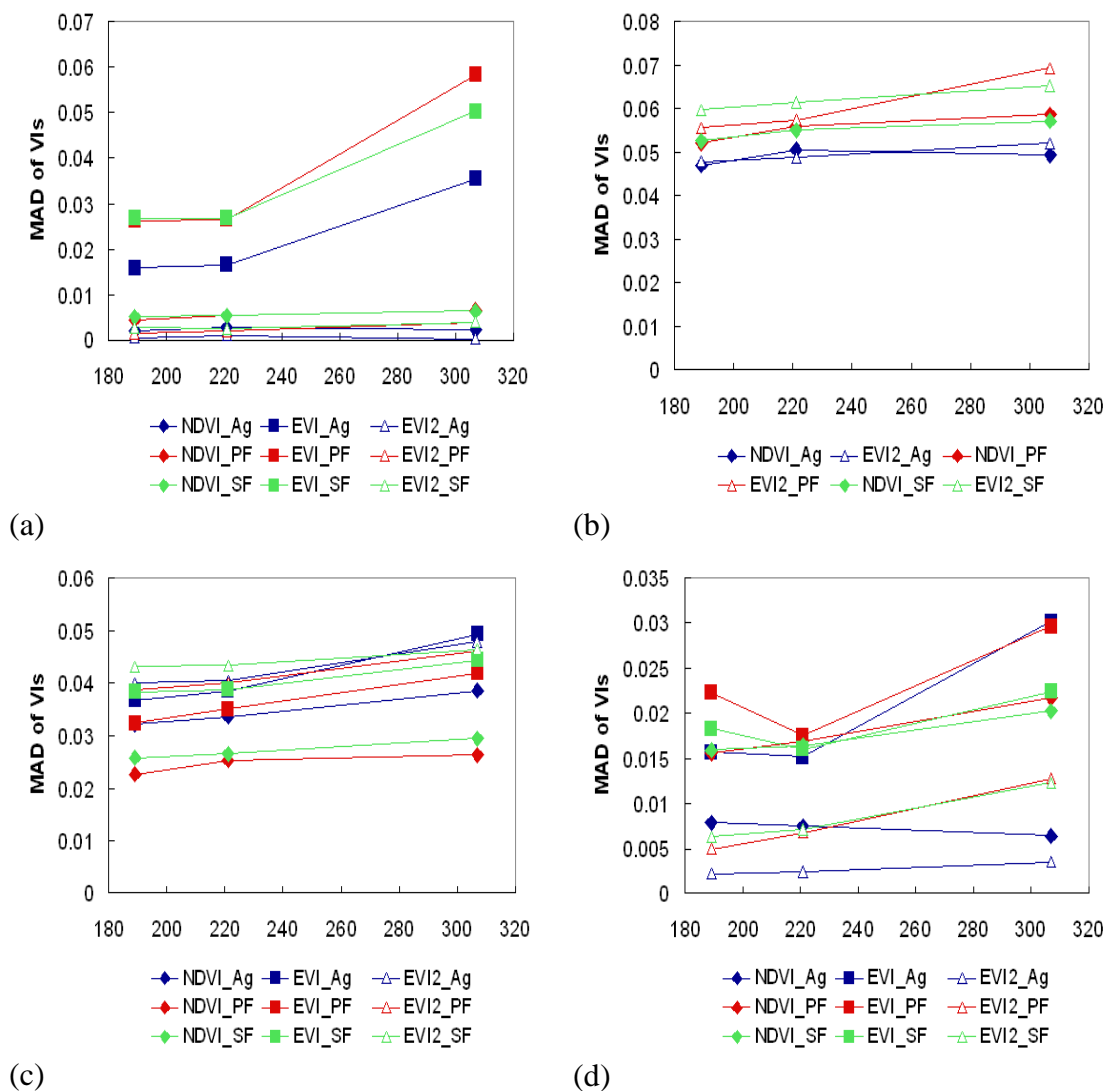


Figure 3-11. MAD variations of VIs between sensor and MODIS regarding three periods (early-, mid-, and late-dry seasons) and land covers (Agricultural site, Primary forest, and secondary forest) ((a) VIIRS, (b) AVHRR, (c) SPOT-VGT, and (d) SeaWiFS).

EVI in all three of the land covers on the late-dry season, the same as the VIIRS and SPOT-VGT.

3.5 The effects of inter sensor translation equation on the phenological stage

Table 3-1 shows the summary of slope, intercept, R^2 and RMSE of inter-sensor translation equations calculated using linear regression lines with MODIS values as a reference (x-axis). Inter-sensor translation equations show strong agreements, because their R^2 ranged from 0.9932 to 0.9998 for the NDVI, EVI, and EVI2 across the combined land covers during the 3-stage dry seasons.

The slopes of VIIRS NDVI and EVI2 were not much different for each DOY (Table 3-1), while the slopes of VIIRS EVI decreased from 0.9318 to 0.8884 (~7% difference) and the intercepts of VIIRS EVI increased with a range of 0.0084 to 0.0367 between DOY 307 and DOY 221. They were, however, not dependent on the phenological stages, because $|t|_{\text{slope}}$ and $|t|_{\text{intercept}}$ were less than 2.58 for all three seasons (Table 3-2). It implied that NDVI, EVI, and EVI2 translations between VIIRS and MODIS were not sensitive to their temporal stage.

The slope variations of AVHRR NDVI in regards to the phenological stages were between 0.941 and 0.965 (0.024) and those of AVHRR EVI2 as concerns the phenological stages were between 0.881 and 0.908 (0.027) (Table 3-1). The slopes of both vegetation indices did not differ greatly from each of the DOY. AVHRR NDVI and EVI2 were independent of the phenological patterns, since $|t|_{\text{slope}}$ and $|t|_{\text{intercept}}$ were less than 2.58 for all three seasons (Table 3-2).

The slope changes of SPOT-VGT NDVI and EVI2 were not greatly distributed for each DOY (Table 3-1), while the slopes of SPOT-VGT EVI increased from 0.956 to 1.001 (~5% difference). Even though the slope changes of SPOT-VGT EVI was relatively large, the difference was not significant due to low $|t|_{\text{slope}}$ and $|t|_{\text{intercept}}$ values for

Table 3-2. Comparison of linear regression equation regarding MODIS at three land covers (Agricultural, Primary forest, and secondary forest)

	vs. sensor	DOY_1	DOY_2	$ t _{\text{slope}}$	$ t _{\text{intercept}}$	
NDVI	VIIRS	189	221	0.004795	0.03037	ND
		189	307	0.106865	0.023925	ND
		221	307	0.101452	0.049276	ND
	SPOT-VGT	189	221	0.108893	0.115298	ND
		189	307	0.091538	0.035331	ND
		221	307	0.183786	0.138207	ND
	SeaWiFS	189	221	0.312432	0.195470	ND
		189	307	0.552617	0.273133	ND
		221	307	0.218983	0.071563	ND
	AVHRR	189	221	0.110902	0.175193	ND
		189	307	0.387533	0.141069	ND
		221	307	0.461834	0.293894	ND
EVI	VIIRS	189	221	0.193190	0.110209	ND
		189	307	0.855549	0.415301	ND
		221	307	0.592762	0.270430	ND
	SPOT-VGT	189	221	0.110408	0.098578	ND
		189	307	0.672918	0.548960	ND
		221	307	0.510744	0.407771	ND
	SeaWiFS	189	221	0.113046	0.107908	ND
		189	307	0.176237	0.096129	ND
		221	307	0.044654	0.024357	ND
EVI2	VIIRS	189	221	0.033402	0.027438	ND
		189	307	0.047153	0.008921	ND
		221	307	0.077416	0.035731	ND
	SPOT-VGT	189	221	0.057004	0.008867	ND
		189	307	0.289181	0.244526	ND
		221	307	0.328693	0.220821	ND
	SeaWiFS	189	221	0.093158	0.028301	ND
		189	307	0.348754	0.129215	ND
		221	307	0.232619	0.092346	ND
	AVHRR	189	221	0.050763	0.058572	ND
		189	307	0.362692	0.100053	ND
		221	307	0.290710	0.153212	ND

X =MODIS value and y =sensor value

$$t_{0.01(2),700} = 2.583, t_{0.01(2),800} = 2.582, t_{0.01(2),1000} = 2.581,$$

$\nu = 544$, and ND=Not significantly different

each DOY pairs (Table 3-2).

The slope of the SeaWiFS EVI decreased slightly from the early-dry (0.980) to the late-dry seasons (0.968), while the slopes of the SeaWiFS NDVI and EVI2 increased from DOY 189 to DOY 307 (Table 3-1). In addition to VIIRS, AVHRR, and SPOT-VGT, $|t|_{\text{slope}}$ and $|t|_{\text{intercept}}$ of SeaWiFS NDVI, EVI, and EVI2 was less than 2.58 and, therefore, SPOT-VGT NDVI, EVI, and EVI2 were not dependent on all three of the dry seasons.

4. CONCLUSION

We found that the convolved sensor VI's phenological patterns behaved differently with the types of land cover (between agricultural and forest sites) rather than across sensor type (spectral response functions) during the 2001 and 2002 dry season periods. In contrast to the EVI and EVI2, the convolved sensor NDVI consistently decreased, irrespective of the land covers. In terms of sensor type influences on phenological patterns, AVHRR NDVI and EVI2 showed the least values across all three of the land covers during the 2001 and 2002 dry seasons and the SeaWiFS NDVI had the largest values for all three land covers in the 2001 and 2002 dry seasons.

As far as VIs deviation analyses for the continuity to MODIS, VIIRS NDVI showed constant deviation, while the AVHRR NDVI deviation mostly decreased, and SPOT-VGT and SeaWiFS NDVI differences typically increased (and then decreased) with increasing MODIS NDVI. VIIRS, SPOT-VGT, and SeaWiFS EVI deviations generally decreased with increasing MODIS EVI, and, in particular, large EVI decreases

occurred on DOY 307 across all the sensors. Sensor EVI2 deviations were similar to sensor NDVI deviations, except for the SPOT-VGT sensor. The VIIRS EVI2 deviation was uniform, while the AVHRR and SPOT-VGT EVI2 deviations decreased and the SeaWiFS EVI2 deviation increased with increasing MODIS EVI2.

Inter-sensor translations of sensor reflectances, NDVI, EVI, and EVI2 were expressed by strong linear relationships with $R^2 > 0.98$ for all three of the dry seasons, except for VIIRS and SeaWiFS blue reflectance. NDVI, EVI, and EVI2 translations between sensors and MODIS for all three of the dry seasons were not significantly different relative to the phenological stages through the student t-Test (Table 3-2), in spite of large deviation and MAD on DOY 307 in VIIRS/SeaWiFS blue reflectances and EVI.

The slope change plots of cross sensors in reflectances and VIs showed the slopes of VIIRS EVI2 translations relative to MODIS EVI2 displayed the least variation, resulting in the least MAD of VIIRS EVI2 regarding MODIS EVI2, and the slopes of VIIRS/SeaWiFS and MODIS blue reflectances varied for each growing stages with the most MAD of EVI between VIIRS/SeaWiFS and MODIS translations. It implied the VIIRS EVI2 continuity to MODIS EVI2 was best and the VIIRS/SeaWiFS EVI continuity to MODIS EVI was worst.

Future studies will be needed to better understand the cross-sensor translations and the evaluation of land cover and/or the combined (the phenology and land covers) influences on inter-sensor translation equations.

REFERENCES

Chapter II

Brown, M. E, J. E. Pinzon, K. Didan, J. T. Morisette, and C. J. Tucker (2006). Evaluation of the consistency of long-term NDVI Time series derived from AVHRR, SPOT-Vegetation, SeaWiFS, MODIS, and Landsat ETM+ Sensors. *IEEE Transactions on geoscience and remote sensing*, vol. 44, No. 7, July: 1787-1793.

Bryant, R., M. S. Moran, S. A. McElroy, C. Holifield, K. J. Thome, T. Miura, and S. F. Biggar (2003). Data Continuity of Earth Observing 1 (EO-1) Advanced Land Imager (ALI) and Landsat TM and ETM+. *IEEE Transactions on Geoscience and Remote Sensing*, Vol. 41 (6), 1204-1214.

Cihlar, J. I., R. Latifovic, J. Chen, A. Trishchenko, Y. Du, G. Fedosejevs, and B. Guindon (2004). Systematic corrections of AVHRR image composites for temporal studies. *Remote sensing of environment*, 89: 217–233.

Didan, K. and A. R. Huete (2006). MODIS vegetation index product series collection 5 change summary. MODIS Land Quality Assessment.

Gallo, K., L. Ji, B. Reed, J. Eidenshrink, and J. Dwyer (2005). Multi-platform comparisons of MODIS and AVHRR normalized difference vegetation index data. *Remote sensing of environment*, 99:221-231

Gallo, K., L. Ji, B. Reed, J. Dwyer, and J. Eidenshrink (2004). Comparison of MODIS and AVHRR 16-day normalized difference vegetation index composite data. *Geophysical research letters*, vol. 31, L07502, doi:10.1029/2003GL019385, 2004.

Gao, X., A. R. Huete, and K. Didan (2003). Multisensor comparisons and validation of MODIS vegetation indices at the semiarid Jornada experimental range. *IEEE Transactions on geoscience and remote sensing* vol. 41, no. 10, October, pp. 2368-2381

Gesch, D. B. (1994). Topographic data requirements for EOS global change research. U.S. Geological Survey Open-File Report, 94-626.

Gitelson, A. and Y. J. Kaufman (1998). MODIS NDVI optimization to fit the AVHRR data series – spectral consideration. *Remote sensing of environment*, 66: 343–350.

Goetz, S. J. (1997) Multi-sensor analysis of NDVI, surface temperature and biophysical variables at a mixed grassland site. *International Journal of Remote Sensing*, vol. 18 (1): 71-94.

Huete, A. R., K. Didan, Y. E. Shimabukuro, P. Ratana, S. R. Saleska, L. R. Hutyrá, W. Yang, R. R. Nemani, and R. Myneni (2006). Amazon rainforests green-up with sunlight

in dry season. *Geophysical Research Letters*, vol. 33, L06420, doi:10.1029/2005GL025583, 2006.

Huete, A. R., T. Miura, Y. Kim, K. Didan, and J. Privette (2006). Assessments of multisensor vegetation index dependencies with hyperspectral and tower flux data. *Optics and Photonics 2006, An SPIE Event, San Diego, CA, 13-17 August, 2006*.

Huete, A. R., Kim, Y., Didan, K., and Miura, T. (2004). Multi- Sensor Translation, Continuity, and Scaling of Vegetation Indices Using Hyperspectral Data. 2004 AGU Fall Meeting, 13-17 December 2004 in San Francisco, California.

Huete, A. R., K. Didan, T. Miura, E. P. Rodriguez, X. Gao, and L. G. Ferreira (2002). Overview of the radiometric and biophysical performance of the MODIS vegetation indices. *Remote sensing of environment*, 83:195-213

Huete, A. R., H. Q. Liu, K. Batchily, and W. van Leeuwen (1997). A comparison of vegetation indices over a global set of TM images for EOS-MODIS. *Remote Sensing of Environment*, 59:440-451.

Kim, Y., Huete, A. R., and Miura, T. (2006). Evaluation of cross sensor vegetation index dependencies with hyperspectral data. *Global Vegetation Workshop 2006, NTSG, University of Montana, Missoula, MT. 7-10 August, 2006*.

Kim, Y. and Huete, A. R. (2005). Remotely Sensed Ecosystem Impacts of Drought at C. Hart Merriam Transect. 8th Biennial Conference of Research on the Colorado Plateau, Northern Arizona University, Flagstaff November 7 - 10, 2005.

Kim, Y., A. R. Huete, and K. Didan (2004). Monitoring Ecosystem Carbon and Water Variations during a Severe Drought in the Southwest with AVIRIS and MODIS Sensor Data, 2004 AGU Fall Meeting, 13-17 December 2004 in San Francisco, California

Miura, T., A. Huete, and H. Yoshioka (2006). An empirical investigation of cross-sensor relationships of NDVI and red/near-infrared reflectance using EO-1 Hyperion data. *Remote Sensing of Environment*, 100, 223–236.

Miura, T., A. R. Huete, and H. Yoshioka (2000). Evaluation of sensor calibration uncertainties on vegetation indices for MODIS. *IEEE Transactions on geoscience and remote sensing* vol. 38, no. 3, May, pp. 1399-1409.

Price, J. C. (1987). Calibration of satellite radiometers and the comparison of vegetation indices. *Remote Sensing of Environment*, 21, 15–27.

Steven, M.D., T. J. Malthus, F. Baret, H. Xu, and M. J. Chopping (2003). Intercalibration of vegetation indices from different sensor systems. *Remote Sensing of Environment*, 88: 412–422.

Trishchenko, A. P., J. Cihlar, and Z. Li (2002). Effects of spectral response function on surface reflectance and NDVI measured with moderate resolution satellite sensors. *Remote sensing of environment*, 81:1-18

Tucker, C. J., J. E. Pinzon, M. E. Brown, D. A. Slayback, E. W. Pak, R. Mahoney, E. F. Vermote and N. E. Saleous (2005). An extended AVHRR 8km NDVI dataset compatible with MODIS and SPOT-VGT NDVI data. *International journal of remote sensing*, Vol. 26, No. 20, 20 October 2005, 4485-4498.

Tucker, C. J. (1979). Red and Photographic Infrared Linear Combinations for Monitoring Vegetation. *Remote Sensing of Environment*, 8:127-150.

van Leeuwen, W. J. D., B. J. Orr, S. E. Marsh, and S. M. Herrman (2006). Multi-sensor NDVI data continuity: Uncertainties and implications for vegetation monitoring applications. *Remote sensing of environment*, 100: 67-81

Vane, Gregg, R. O. Green, T. G. Chrien, H. T. Enmark, E. G. Hansen, and W. M. Porter (1993). The Airborne Visible/Infrared Imaging Spectrometer (AVIRIS). *Remote sensing of environment*, 44: 127-143.

Vermote, E. F. and N. Z. Saleous (2006). Calibration of NOAA16 AVHRR over a desert site using MODIS Data. *Remote Sensing of Environment*, 105:214-220.

Vermote, E. F., D. Tanre, J. L. Deuze, M. Herman, and J. Morcrette (1997). Second simulation of the satellite signal in the solar spectrum, 6S: An overview. *IEEE TRANSACTIONS ON GEOSCIENCE AND REMOTE SENSING*, VOL. 35, NO. 3, MAY 1997: 675-686.

Zar, J. H. (1999). *Biostatistical Analysis*. Fourth Ed. pp. 362-364.

Chapter III

- Asrar, G., M. Fuchs, E. T. Kanemasu, and J. L. Hatfield. (1984). Estimating absorbed photosynthetic radiation and leaf area index from spectral reflectance in wheat. *Agronomy Journal*, 76, 300– 306.
- Brown, M. E., J. E. Pinzon, K. Didan, J. T. Morisette, and C. J. Tucker (2006). Evaluation of the consistency of long-term NDVI Time series derived from AVHRR, SPOT-Vegetation, SeaWiFS, MODIS, and Landsat ETM+ Sensors” *IEEE Transactions on geoscience and remote sensing*, vol. 44, No. 7, July: 1787-1793
- Bryant, R., M. S. Moran, S. A. McElroy, C. Holifield, K. J. Thome, T. Miura, and S. F. Biggar (2003). Data Continuity of Earth Observing 1 (EO-1) Advanced Land Imager (ALI) and Landsat TM and ETM+. *IEEE Transactions on Geoscience and Remote Sensing*, Vol. 41 (6), 1204-1214.
- Coops, N. C., T. A. Black, R. S. Jassal, J. A. Trofymow, K. Morgenstern. (2007). Comparison of MODIS, eddy covariance determined and physiologically modeled gross primary production (GPP) in a Douglas-fir forest stand. *Remote sensing of environment*, 107: 385-401
- Didan, K. and A. R. Huete (2006). MODIS vegetation index product series collection 5 change summary. MODIS Land Quality Assessment.
- Fensholt, R., I. Sandholt, and S. Stisen (2006). Evaluating MODIS, MERIS, and VEGETATION vegetation indices using in situ measurements in a Semiarid Environment. *IEEE Transactions on Geoscience and Remote Sensing*, Vol. 44 (7), 1774-1786.
- Fensholt, R. (2004). Earth observation of vegetation status in the Sahelian and Sudanian West Africa: comparison of Terra MODIS and NOAA AVHRR satellite data. *International Journal of Remote Sensing*, 25, 1641-1659.
- Field, C. B., J. T. Randerson, and C. M. Malmstrom (1995) Global Net Primary Production: Combining Ecology and Remote Sensing” *Remote sensing of environment*, 51:74-88
- Gallo, K., L. Ji, B. Reed, J. Eidenshrink, and J. Dwyer (2005). Multi-platform comparisons of MODIS and AVHRR normalized difference vegetation index data. *Remote sensing of environment*, 99:221-231
- Gallo, K., L. Ji, B. Reed, J. Dwyer , and J. Eidenshrink (2004). Comparison of MODIS and AVHRR 16-day normalized difference vegetation index composite data. *Geophysical research letters*, vol. 31, L07502, doi:10.1029/2003GL019385, 2004.

- Gao, X., A. R. Huete, W. Ni, and T. Miura (2000). Optical–biophysical relationships of vegetation spectra without background contamination. *Remote Sensing of Environment*, 74, 609– 620.
- Gesch, D. B. (1994). Topographic data requirements for EOS global change research. US Geological Survey Open-File Report, 94-626.
- Gitelson, A. and Y. J. Kaufman (1998). MODIS NDVI optimization to fit the AVHRR data series – spectral consideration. *Remote sensing of environment*, 66: 343–350.
- Goetz, S. J. (1997). Multi-sensor analysis of NDVI, surface temperature and biophysical variables at a mixed grassland site. *International Journal of Remote Sensing*, vol. 18 (1): 71-94.
- Heinsch, F. A, M. Zhao, S. W. Running, J. S. Kimball, R. R. Nemani, K. J. Davis, P. V. Bolstard, B. D. Cook, A. R. Desai, D. M. Ricciuto, B. E. Law, W. C. Oechel, H. Kwon, H. Luo, S. C. Wolfy, A. L. Dunn, J. W. Munger, D. D. Baldocchi, L. Xu, D. Y. Hollinger, A. D. Richardson, P. C. Stoy, M. B. S. Siqueira, R. K. Monson, S. P. Burns, and L. B. Flanagan (2006). Evaluation of remote sensing based terrestrial productivity from MODIS using regional tower eddy flux network observations” *IEEE transactions on geoscience and remote sensing*, vol. 44, no. 7, July, pp.1908-1925
- Holben, B. N., T. F. Eck, I. Slutsker, D. Tanre, J. P. Buis, A. Setzer, E. Vermote, J. A. Reagan, Y. J. Kaufman, and T. Nakajima (1998). AERONET-A federated instrument network and data archive for aerosol characterization, *Remote sensing of environment*, 66:1-16.
- Huete, A. R., K. Didan, Y. E. Shimabukuro, P. Ratana, S. R. Saleska, L. R. Hutyrá, W. Yang, R. R. Nemani, and R. Myneni (2006a) Amazon rainforests green-up with sunlight in dry season. *Geophysical Research Letters*, vol. 33, L06405, doi: 10.1029/2005GL025583.
- Huete, A. R., T. Miura, Y. Kim, K. Didan, and J. Privette (2006b). Assessments of multisensor vegetation index dependencies with hyperspectral and tower flux data. *Optics and Photonics 2006, An SPIE Event, San Diego, CA, 13-17 August, 2006.*
- Huete, A. R., K. Didan, T. Miura, E. P. Rodriguez, X. Gao, and L. G. Ferreira (2002). Overview of the radiometric and biophysical performance of the MODIS vegetation indices. *Remote sensing of environment*, 83:195-213
- Huete, A. R., H. Q. Liu, K. Batchily, and W. van Leeuwen (1997). A comparison of vegetation indices over a global set of TM images for EOS-MODIS. *Remote Sensing of Environment*, 59:440-451.

Jiang, Z., A. R. Huete, K. Didan, and T. Miura (2007). Development of a 2-band enhanced vegetation index without a blue band, submitted to Remote Sensing of Environment.

Kim, Y. and Huete, A. R. (2005). Remotely Sensed Ecosystem Impacts of Drought at C. Hart Merriam Transect. 8th Biennial Conference of Research on the Colorado Plateau, Northern Arizona University, Flagstaff November 7 - 10, 2005.

Kim, Y., A. R. Huete, and K. Didan (2004). Monitoring Ecosystem Carbon and Water Variations during a Severe Drought in the Southwest with AVIRIS and MODIS Sensor Data, 2004 AGU Fall Meeting, 13-17 December 2004 in San Francisco, California

King, M. D., Menzel, W. P., Kaufman, Y. J., Tanre, D., Gao, B. -C., Platnick, S., et al. (2003). Cloud and aerosol properties, precipitable water, and profiles of temperature and water vapor from MODIS. IEEE Transactions on Geoscience and Remote Sensing, 41(2), 442–458.

Miura, T., A. Huete, and H. Yoshioka (2006). An empirical investigation of cross-sensor relationships of NDVI and red/near-infrared reflectance using EO-1 Hyperion data. Remote Sensing of Environment, 100, 223–236.

Running, S. W., R. R. Nemani, F. A. Heinsch, M. Zhao, M. Reeves, and H. Hashimoto (2004). A continuous satellite-derived measure of global terrestrial primary production. BioScience, Vol. 54, No. 6, pp. 547-560. June 2004.

Schloss, A. L., D. W. Kicklighter, J. Kaduk, and U. Wittenberg (1999). Comparing global models of terrestrial net primary productivity (NPP): Comparisons of NPP to climate and the normalized difference vegetation index (NDVI) Global Change Biology, 5 (Suppl. 1), 25-34

Sellers, P. C. (1985). Canopy reflectance, photosynthesis and transpiration. International Journal of Remote Sensing, 6, 1335– 1372.

Steven, M.D., T. J. Malthus, F. Baret, H. Xu, and M. J. Chopping (2003). Intercalibration of vegetation indices from different sensor systems. Remote Sensing of Environment, 88: 412–422.

Tucker, C. J., J. E. Pinzon, M. E. Brown, D. A. Slayback, E. W. Pak, R. Mahoney, E. F. Vermonte and N. E. Saleous (2005). An extended AVHRR 8km NDVI dataset compatible with MODIS and SPOT vegetation NDVI data. International journal of remote sensing, Vol. 26, No. 20, 20 October 2005, 4485-4498.

Tucker, C. J. (1979). Red and Photographic Infrared Linear Combinations for Monitoring Vegetation. Remote Sensing of Environment, 8:127-150.

van Leeuwen, W. J. D., B. J. Orr, S. E. Marsh, and S. M. Herrman (2006). Multi-sensor NDVI data continuity: Uncertainties and implications for vegetation monitoring applications. *Remote sensing of environment*, 100: 67-81

van Leeuwen, W. J. D., A. R. Huete, and T. W. Laing (1999). MODIS Vegetation Index Compositing Approach: A prototype with AVHRR Data. *Remote sensing of environment*, 69:264-280

Vermote, E. F., D. Tanre, J. L. Deuze, M. Herman, and J. Morcrette (1997). Second simulation of the satellite signal in the solar spectrum, 6S: An overview. *IEEE TRANSACTIONS ON GEOSCIENCE AND REMOTE SENSING*, VOL. 35, NO. 3, MAY 1997: 675-685.

Xiao, X., Q. Zhang, S. Saleska, L. Hutya, P. D. Camargo, S. Wofsy, S. Frolking, S. Boles, M. Keller, and B. Moore (2005). Satellite-based modeling of gross primary production in a seasonally moist tropical evergreen forest. *Remote Sensing of Environment*, 94:105-122.

Xiao, X., Q. Zhang, B. Braswell, S. Urbanski, S. Boles, S. Wofsy, B. Moore, and D. Ojima (2004). Modeling gross primary production of temperate deciduous broadleaf forest using satellite images and climate data. *Remote Sensing of Environment*, 91:256-270.

Chapter IV

Asrar, G., M. Fuchs, E. T. Kanemasu, and J. L. Hatfield (1984). Estimating absorbed photosynthetic radiation and leaf area index from spectral reflectance in wheat. *Agronomy Journal*, 76, 300–306.

Braswell, B. H., D. S. Shimel, E. Linder, and B. Moore III (1997). The response of global terrestrial ecosystems to interannual temperature variability. *Science* v278.n5339:pp870(3).

Coops, N. C., T. A. Black, R. S. Jassal, J. A. Trofymow, K. Morgenstern (2007). Comparison of MODIS, eddy covariance determined and physiologically modeled gross primary production (GPP) in a Douglas-fir forest stand. *Remote sensing of environment*, 107: 385-401.

Cox, P. M., R. A. Betts, C. D. Jones, S. A. Spall, and I. J. Totterdell (2000). Acceleration of global warming due to carbon-cycle feedbacks in a coupled climate model. *Nature* 408, 184.

Field, C. B., J. T. Randerson, and C. M. Malmstrom (1995). Global Net Primary Production: Combining Ecology and Remote Sensing. *Remote sensing of environment*, 51:74-88.

Gao, X., A. R. Huete, W. Ni, and T. Miura (2000). Optical–biophysical relationships of vegetation spectra without background contamination. *Remote Sensing of Environment*, 74, 609–620.

Heinsch, F. A., M. Zhao, S. W. Running, J. S. Kimball, R. R. Nemani, K. J. Davis, P. V. Bolstad, B. D. Cook, A. R. Desai, D. M. Ricciuto, B. E. Law, W. C. Oechel, H. Kwon, H. Luo, S. C. Wolfy, A. L. Dunn, J. W. Munger, D. D. Baldocchi, L. Xu, D. Y. Hollinger, A. D. Richardson, P. C. Stoy, M. B. S. Siqueira, R. K. Monson, S. P. Burns, and L. B. Flanagan (2006). Evaluation of remote sensing based terrestrial productivity from MODIS using regional tower eddy flux network observations. *IEEE transactions on geoscience and remote sensing*, vol. 44, no. 7, July, pp.1908-1925.

Hill, M. J., A. A. Held, R. Leuning, N. C. Coops, D. Hughes, and H. A. Cleugh (2006). MODIS spectral signals at a flux tower site: Relationships with high-resolution data, and CO₂ flux and light use efficiency measurements. *Remote Sensing of Environment*, 103:351-368.

Holben, B.N., T.F. Eck, I. Slutsker, D. Tanre, J.P. Buis, A. Setzer, E. Vermote, J.A. Reagan, Y. J. Kaufman, and T. Nakajima, 1998, AERONET--A federated instrument

network and data archive for aerosol characterization, *Remote Sensing of Environment*, 66:1-16.

Huemrich, K. F., T. A. Black, P. G. Jarvis, J. M. McCaughey, and F. G. Hall (1999). High temporal resolution NDVI phenology from micrometeorological radiation sensors. *Journal of Geophysical Research*, Vol. 104, No. D22:27935-27944.

Huete, A. R., Y. Kim, P. Ratana, K. Didan, Y. E. Shimabukuro, and T. Miura (2007). Assessments of phenologic variability in Amazon tropical rainforests using hyperspectral Hyperion and MODIS satellite data. In: (Kalacska M., Sanchez-Azofeifa, A., eds.), *Hyperspectral Remote Sensing of Tropical and Sub-Tropical Forests*.

Huete, A. R., T. Miura, Y. Kim, K. Didan, and J. Privette (2006a). Assessments of multisensor vegetation index dependencies with hyperspectral data and tower flux data. SPIE 6298-45, *Proceedings on Remote Sensing and Modeling of Ecosystems for Sustainability III*.

Huete, A. R., K. Didan, Y. E. Shimabukuro, P. Ratana, S. C. Saleska, L. R. Hutya, W. Yang, R. R. Nemani, and R. Myneni (2006b). Amazon rainforests green-up with sunlight in dry season. *GEOPHYSICAL RESEARCH LETTERS*, VOL. 33, L06405, doi:10.1029/2005GL025583.

Huete, A. R., H. Q. Liu, K. Batchily, and W. van Leeuwen (1997). A comparison of vegetation indices over a global set of TM images for EOS-MODIS. *Remote Sensing of Environment*, 59:440-451. (1997)

Jiang, Z., A. R. Huete, K. Didan and T. Miura (2007). Development of a 2-band enhanced vegetation index without a blue band. Submitted to *Remote Sensing of Environment*.

Kang, S., S. W. Running, J. Lim, M. Zhao, C. Park, and R. Loehman (2003). A regional phenology model for detecting onset of greenness in temperate mixed forests, Korea: an application of MODIS leaf area index. *Remote Sensing of Environment*, 86, 232-242.

Kobayashi, H. and D. G. Dye (2005). Atmospheric conditions for monitoring the long-term vegetation dynamics in the Amazon using normalized difference vegetation index. *Remote Sensing of Environment*, 97, 519–525.

Myneni, R. B., C. D. Keeling, C. J. Tucker, G. Asrar, and R. R. Nemani (1997). Increased plant growth in the northern high latitudes from 1981–1991. *Nature*, **386**, 698–702.

Reed, B. C., J. F. Brown, D. VanderZee, T. R. Loveland, J. W. Merchant, and D. O. Ohlen (1984). Measuring phenological variability from satellite imagery. *Journal of Vegetation Science*, 5, 703-714.

Running, S. W., R. R. Nemani, F. A. Heinsch, M. Zhao, M. Reeves, and H. Hashimoto (2004). A continuous satellite-derived measure of global terrestrial primary production. *BioScience*, Vol. 54, No. 6, pp. 547-560. June.

Sakamoto, T., M. Yokozawa, H. Toritani, M. Shibayama, N. Ishitsuka, and H. Ohno (2005). A crop phenology detection method time-series MODIS data. *Remote Sensing of Environment*, 96, 366-374.

Saleska, S. R., S. D. Miller, D. M. Matross, M. L. Goulden, S. C. Wofsy, H. R. Rocha et al. (2003). Carbon in Amazon forests: Unexpected seasonal fluxes and disturbance-induced losses. *Science*, 302, 1554-1557.

Schloss, A. L., D. W. Kicklighter, J. Kaduk, and U. Wittenberg (1999). Comparing global models of terrestrial net primary productivity (NPP): Comparisons of NPP to climate and the normalized difference vegetation index (NDVI). *Global Change Biology*, 5 (Suppl. 1), 25-34.

Sellers, P. (1987). Canopy reflectance, photosynthesis, and transpiration, II, "The role of biophysics in the linearity of their interdependence. *Remote Sensing of Environment*, 21, 1.

Tucker, C. et al. (2005). An extended AVHRR 8-km NDVI dataset compatible with MODIS and SPOT vegetation NDVI data. *International Journal of Remote Sensing*, 26, 4485-4498.

Tucker, C. (1979). Red and photographic infrared linear combinations for monitoring vegetation. *Remote Sensing of Environment*, 8, 127-150.

Vermote, E. F., D. Tanre, J. L. Deuze, M. Herman, and J. Morcrette (1997). Second simulation of the satellite signal in the solar spectrum, 6S: An overview. *IEEE Transactions on Geoscience and Remote Sensing*, VOL. 35, NO. 3, MAY 1997: 675-686.

Wang, Q., J. Tenhunen, N. Q. Dinh, M. Reichstein, T. Vesala, and P. Keronen (2004). Similarities in ground- and satellite-based NDVI time series and their relationships to physiological activity of a Scots pine forest in Finland. *Remote Sensing of Environment*, 93:225-237.

Wilson, T. B. and T. P. Meyers (2007). Determining vegetation indices from solar and photosynthetically active radiation fluxes. *Agricultural and Forest Meteorology*, 144:160-179.

Xiao, X., S. Hagen, Q. Zhang, M. Keller, B. Moore III (2006). Detecting leaf phenology of seasonally moist tropical forests in South America with multi-temporal MODIS images. *Remote Sensing of Environment*, 103:465-473.

Zhang, X., J. C. F. Hodges, C. B. Schaaf, M. A. Friedl, A. H. Strahler, and F. Gao (2001). Global vegetation phenology from AVHRR and MODIS data. *Geoscience and Remote Sensing Symposium, 2001. IGARSS '01. IEEE 2001 International Volume 5, 9-13 July 2001* Page(s):2262 – 2264.

Zhang, X., M. A. Friedl, C. B. Schaaf , A. H. Strahler, J. C.F. Hodges, F. Gao, B. C. Reed, A. R. Huete (2003). Monitoring vegetation phenology using MODIS. *Remote Sensing of Environment*, 84:471-475.